NASA CR-15,224
Available to the Public

ESTIMATION OF TUNNEL BLOCKAGE FROM WALL PRESSURE SIGNATURES: A REVIEW AND DATA CORRELATION

By

J. E. Hackett
D. J. Wilsden
D. E. Lilley

MARCH 1979

Prepared under Contract No. NAS2-9883 by
LOCKHEED-GEORGIA COMPANY
Marietta, Georgia

For Ames Research Center
NATIONAL AERONAUTICS AND SPACE ADMINISTRATION

NASA CR-15,224
Available to the Public

ESTIMATION OF TUNNEL BLOCKAGE FROM WALL PRESSURE SIGNATURES: A REVIEW AND DATA CORRELATION

By

J. E. Hackett
D. J. Wilsden
D. E. Lilley

MARCH 1979

Prepared under Contract No. NAS2-9883 by
LOCKHEED-GEORGIA COMPANY
Marietta, Georgia

For Ames Research Center
NATIONAL AERONAUTICS AND SPACE ADMINISTRATION

CONTENTS

LIST OF FIGURES

LIST OF SYMBOLS

$A_1 \ldots A_7$	curve-fit coefficients defined via equation (4.8)
A	(Section 4) coefficient of x^2/B^2
A	(elsewhere) cross-sectional area
AR	aspect ratio
B	(Section 4) coefficient of x/B
B	(Section 7.5) cross-sectional area of separation bubble
B	(elsewhere) tunnel width
b_s, b_w	line source spans for solid and wake blockage models
C	(Section 4) constant in quadratic curve fit
C	(elsewhere) tunnel cross-sectional area
c_s	spacing between source-sink pair $\pm Q_s$
C_p	static pressure coefficient $(p - p_\infty)/\frac{1}{2}\rho U_\infty^2$
ΔC_p	C_p increment relative to empty tunnel value at same location
C_L, C_D, $C_{M_{\frac{1}{4}}}$	lift, drag and quarter-chord pitching moment coefficients based upon model reference area
C_{D_o}	lift-independent drag coefficient
ΔC_D	incremental drag coefficient due to "horizontal buoyancy"
δC_D	$d(\Delta C_D)/dx$
C_μ	knee-blowing jet momentum coefficient for KBF model
D	drag
ΔD	drag increment due to "horizontal buoyancy"
H	tunnel height
i	iteration index (Section 5)
k	Maskell's base pressure parameter (Section 7.5)
m,n	(Appendices IV and V) indices which locate a member of the source-sink image system for rectangular tunnels
M,N	(Appendices IV and V) limit values of m,n
p	local static pressure

q_θ	local surface tangential velocity
Q	line source or sink strength (volume/second)
$\pm Q_s$	strength of source/sink pair representing solid or bubble blockage component
Q_w	strength of source representing wake blockage component
R	sphere radius
R_1, r_∞	asymptotic base radius of effective body implied by source-sink model
R_2	maximum radius of effective body implied by source-sink model
R	(Appendix IV) axial velocity function in equation (A1)
r	local radius of effective, source-sink body
S	reference area for force and moment coefficients
T	(Appendix IV) tangent function in equation (A1)
U	axial velocity
Δu, Δv, Δw	induced velocities in the direction of the tunnel axis, spanwise and in the lift direction
Δu^+, Δu^-	induced velocity increments due to source or sink systems, respectively
X, Y, Z	coordinates along the tunnel axis, spanwise and in the lift direction. (Note, specialized definitions are employed within Appendix IV.)
Δx	half-width of symmetric wall velocity increment signature at half peak height
α	angle of attack
ε	(Section 7.2) half source-sink spacing
ε	(elsewhere) $\Delta u/U_\infty$
ε_M	value of $\Delta u/U_\infty$ at model location
ε_{max}	maximum value of $\Delta u/U_\infty$
η	(Section 2.3) blockage factor: replaces Maskell's ε
θ or ϕ	angular distance from front stagnation
μ	doublet strength
ρ	density

Subscripts:

b	base
c	corrected
m	model
max	maximum
p	peak
s	source/sink (refers to solid/bubble blockage model)
u	uncorrected
w	wake (refers to viscous wake blockage model)

SUMMARY

A new method is described for estimating low speed wind tunnel blockage, including model volume, bubble separation and viscous wake effects. A tunnel-centerline, source/sink distribution is derived from measured wall pressure signatures using fast algorithms to solve the inverse problem in three dimensions. Blockage may then be computed throughout the test volume.

The method is applied to the results of tests carried out on normal flat plates, on spheres, on an idealized automobile, on flat plate wings, and on a powered aircraft model. Correlations using scaled models or tests in two tunnels were made in all cases. In many cases model reference area exceeded 10% of the tunnel cross-sectional area. Good correlations were obtained regarding model surface pressures, lift drag and pitching moment.

It is shown that blockage-induced velocity variations across the test section are relatively unimportant but axial gradients should be considered when model size is determined.

Detailed descriptions are given of the computational procedures and a program listing is provided.

A copy of this document is retained in the Lockheed-Georgia Company Engineering Report Files. The identifying number is LG79ER0051.

ACKNOWLEDGEMENTS

The authors wish to offer their thanks and appreciation to the following people for their help in this program:

Vic Lyman for calculating the influence coefficients for the 40' x 80' tunnel cross section.

"Sam" Sampath for studies of sphere aerodynamics using the Douglas-Neumann program.

Sherry Bartley for help in preparing the figures.

Barbara Reagan and Elizabeth Gardner for typing the test and figure material.

1.0 INTRODUCTION

1.1 Reasons for the Present Study

During the course of routine testing in the Lockheed-Georgia Company's $16\frac{1}{4}' \times 23\frac{1}{4}'$ wind tunnel, the shortcomings of existing wind tunnel blockage correction methods became evident. The number of corrections applied roughly equalled the number of customers requesting them and when applied to the same data, a very significant spread in results was apparent. A review of the methods themselves revealed that they were often based on doubtful assumptions or required test information which was not easy to obtain. A long-term program was therefore started with the aim of overcoming these deficiencies.

A new blockage estimation method was developed in 1974-5 (ref. 1) based upon the analysis of wind tunnel wall pressure signatures. The method permits the estimation of both solid blockage (including that due to closed-separation bubbles) and wake blockage for three-dimensional models. In its early form "desk-top", chart look-up techniques were employed and a number of somewhat arbitrary assumptions were required. Nevertheless, good correlations were obtained in tests with large square flat plates mounted normally to the air-stream. Over the intervening years, the method has been refined somewhat (refs. 2 and 3) and has been computerized in an efficient form. It is now used regularly at Lockheed-Georgia both in its $16\frac{1}{4} \times 23\frac{1}{4}'$ low-speed wind tunnel and in a small, $30'' \times 43''$ research tunnel. The method is proving invaluable in full-scale car tests, in the large tunnel, and is used routinely by major car manufacturers.

Though the early normal flat plate tests underpin applications to cars quite well, a much broader correlation base is required before the method can be considered for general use. To this end, a number of basic tests were conducted in 1975-6, supported both by Lockheed and by the NASA, involving more complicated configurations. A major objective of the present study is to analyze and correlate these data and to investigate practical problems and limitations which are found. An equally important objective is to prepare a program for the NASA-Ames $40' \times 80'$ tunnel, similar to the program now in use

at Lockheed and implement it, off line, on the CDC 7600 at Ames. This program is documented herein. These objectives relate predominantly to defining the model environment, in terms of tunnel-induced velocity increments due to blockage effects. The original terms of reference also emphasized the use of small-model assumptions and effective model position. However, this has been found impractical in some cases, since large models are needed to produce tunnel effects which can be measured accurately.

1.2 Physcial Limitations for Testing

Tunnel blockage, due to the volume of a model and its wake, causes velocity changes primarily in the axial direction. These changes are relatively uniform at a given transverse plane (see Reference 3) so transverse velocities are small. However, axial gradients of axial velocity can be significant in relation to model length and can lead to increasing uncertainty in correcting data for large models. Adverse tunnel-induced pressure gradients may cause noticeable boundary layer thickening or even changes in separation point on the model. Even though the new, wall pressue signature methods for blockage estimation provide a good definition of interference velocities and even though these can be translated into "horizontal buoyancy" corrections, tunnel-induced changes in the viscous effects on the model (particularly separation) may prevent valid testing.

Another consequence of tunnel blockage stems from the pressure disturbances induced at the wall. Generally, there is a favorable pressure gradient to a point just aft of the model, followed by an adverse gradient to an asymptote determined by wake diameter. Tunnel wall boundary layers thicken in this region and the displacement effect adds to blockage. The authors are aware of no previous attempt to correct for this effect. However, the wall pressure signature method provides this correction automatically.

Though, in principle, models with very high solid/bubble blockage and low wake blockage might separate the flow on tunnel surfaces, this has not been observed in the unpowered tests described herein. Even with a 15-inch supercritical sphere in a 30-inch high tunnel (13.5% S/C), there was no sign of

tunnel floor or roof separation. It appears that lift effects, particularly with powered models, are more likely to separate tunnel surfaces than is blockage.

Model lift or any net force transverse to the flow, causes tunnel-induced changes at the model location primarily in flow angle. Though the topic is outside the scope of the present work, transverse gradients in this flow angle may provide an earlier test limit than do blockage effects. A large span wing, for example, may develop unrepresentative span loads, incorrect induced drag and even premature tip stall long before a limiting blockage condition is reached.

Whether lift or blockage is limiting, it is unlikely that hard, generally applicable test boundaries can be drawn. "Hard points" can be established for representative configurations, as herein, but in novel or marginal circumstances direct observation should always be used to determine if the tunnel is "in trouble." As the relationship between computational and experimental approaches to fluid problems become more developed, it will be possible to use the new, wall pressure signature methods with increasing effectiveness. The merger will probably start at a basic research level, in application to simpler shapes and will spread more widely as the art develops.

1.3 Layout of the Present Report

The work presented in this report concerns theory, its application to practical problems at several levels, and ensuing correlations of pressures and forces. A brief overview of the method and the tests is given in Sections 2 and 3 followed, in successive sections, by accounts of successive steps in reduction and analysis. At each stage, appropriate examples will be drawn from the body of test data. Because of the breadth and depth of the present subject matter, no attempt will be made to report the data comprehensively or to provide extensive theoretical development where these are available elsewhere.

Section 4 will be devoted to wall pressure signatures, how to measure them and how they are analyzed. Section 5, which is included mainly for physical insight, concerns the geometric shapes implied by the flow models obtained from the wall pressures. Centerline blockage velocity distributions and their application to pressure corrections and force corrections -- the "bottom line" in the present work -- are discussed respectively in Sections 6 and 8. Because of its importance and the difficulty in determining it accurately, drag is duscussed separately in Section 7. Completing the build-up towards more complex cases, Section 8 is devoted to lifting and powered models.

Possible future developments are reviewed in Section 9, leading to the conclusions which are set out in Section 10.

Program details and listings are included in Appendices I, II, and III. Operational charts for use with rectangular tunnels and the 40' x 80' tunnel are given in Appendices IV and V, respectively.

2.0 OUTLINE OF THE "WALL PRESSURE SIGNATURE" METHOD AND ITS RELATIONSHIP TO OTHER METHODS

2.1 Determination of Solid and Wake-Blockage Parameters

In a typical experiment (Figure 2.1) wall pressures are measured along the centerlines of the tunnel walls or roof. If lift is present, the mean of corresponding floor and roof pressures can be taken, or sidewall pressures may be used. These pressures are used to determine source and sink strengths, spans, and locations on the tunnel centerline (Figure 2.2) which define a body outline which is equivalent to the test model and its wake.

A typical wall supervelocity signature (Figure 2.2, lower) includes a velocity peak, just aft of the model, which reflects the presence of the expanding separation bubble which closes further downstream leaving a viscous wake. The asymptote downstream is a result of the displacement thickness of this wake.

For the purpose of analysis, the measured profile is resolved into symmetric and anti-symmetric parts, as shown in the lower part of Figure 2.2. This simplifies the task of determining the equivalent body since the symmetric part corresponds to solid/bubble blockage and the anti-symmetric part reflects wake blockage. Resolution of these components from the measured signature is achieved via an iterative process which will be described in Section 4.

The wake blockage parameters, Q_w and x_2, emerge directly from the wake signature analysis. However, to obtain the solid blockage parameters Q_s and c_s, a chart look-up technique is employed as illustrated in Figure 2.3. Preparation of these charts is discussed in Appendices IV and V. Inputs to the charts are the symmetric part peak height $(\Delta u/U)_{max}$ and half width at half peak height, $\Delta x/B$, from the resolved signature, together with source/sink span (b_s/B) which is estimated from model geometry.

In essence, the above analysis is an engineering solution of a set of equations involving five nonlinear terms (source and sink geometry) and two

linear terms (source and sink strengths). These equations are written out fully, for rectangular tunnels, in Appendix IV.

Because the problem is nonlinear, multiple solutions are possible and it is necessary to demonstrate that appropriate roots are obtained by the above procedures. Reference 3 describes a Lockheed study using a nonlinear solver algorithm which accepts sets of seven wall pressures as inputs and returns the seven aerodynamic variables as output. It was necessary to provide the program with an initial guess of the roots. By varying the guesses, it was possible to converge onto various differing roots. By these means, it was established that the source/sink strengths were "hard" variables (i.e., had nearly-unique roots) and their streamwise locations were "soft" in nature. The table at the top of Figure 2.4 shows a number of sets of roots obtained for a typical normal-plate experiment. The lower part of the figure shows the corresponding centerline distributions of interference velocity. Despite the wide variation in the aerodynamic variables shown in the table, the plot shows that this was inconsequential with regard to the interference velocity at the tunnel centerline. The engineering method produces solutions very close to those from the full nonlinear analysis.

2.2 Interference Velocities and Their Distribution in the Tunnel

Figure 2.5 shows incremental pressure coefficients, at four tunnel cross sections, induced by the image system for a large sphere at subcritical Reynolds number. The corresponding supervelocities, on the tunnel centerline, increase from 7.5% at the front of the sphere to 3.8% at its maximum diameter and continue rising to 11.3% and 11.2% at planes C and D due to the expanding separation bubble. Interference velocity decreases downstream of D as the separation bubble closes.

Although axial variation is very marked, the lower part of Figure 2.5 shows that percentage variations at any one cross section are not large — particularly within the region occupied by the model. It follows from continuity considerations that blockage-induced lateral velocities — which derive from axial velocity changes — are also small. A detailed analysis of

blockage variations on sphere pressures will be presented in Section 6 of this report.

2.3 Comparison With Other Methods

Blockage correction methods fall broadly into two classes, requiring geometric or geometric-plus-measured tunnel data, respectively. In the absence of pressure data from the tunnel, aerodynamic estimates have to be made which are often conjectural. Figure 2.6 shows a comparison between five blockage estimation methods applied to bluff models, using data taken largely from Reference 6. The methods tabulated in the figure will be reviewed only briefly here; Reference 6 describes the more subtle distinctions between them.

It is evident that the two geometric methods (References 7 and 8) give lower blockage estimates than two of the three methods employing tunnel measurements. Hensel's method, published in 1951 (Reference 9) relies upon wall pressure measurement as does the Hackett/Wilsden method. However, it has been found that use of pressures "opposite to the model location" as recommended by Hensel may be hazardous, since strong pressure gradients are usually present at this location. The method has recently been revised, for use in car testing, so as to use peak suction measurements. Another feature of the Hensel method is that it uses doublets to model the flow. This renders the method less flexible than the Hackett/Wilsden method, which permits variable source-sink spacing. This can be important for long models or models with thick wakes. Corrections via the Hensel method (Figure 2.6) are generally lower than by Hackett/Wilsden — noticeably so in the case of the sphere.

Maskell's method, which appeared in 1963 (Reference 10), determines dynamic pressure correction from an empirical relationship involving measured drag or, in a variant of the method, measured drag in combination with base pressure. Maskell shows the drag coefficient is proportional to base pressure, for square plates, and notes that non-square plates exhibit varying base pressure across their span. In the equation* $\Delta q/q = \eta C_D S/C$, η is assigned

*To avoid confusion with blockage velocity ratio, Maskell's ε has been replaced by η.

tabulated values which vary from 2.77 to 2.13 for plate aspect ratios in the range 1 to 10. Maskell's method is well founded and gives good results for normal flat plates. However, in other applications determination of base pressure for direct use in the method may be hazardous not only because of the aforementioned aspect ratio effects but also due to vortex separations which may exist to each side of the separation bubble. If the tabulated values of η are used, there may be difficulty both in separating bubble drag from other components and in estimating the aspect ratio of the separation bubble. Though Maskell asserts correctly that an η value of 2.5 ± 0.25 is reasonably accurate in situations where q-corrections are of order 10%, the spread in estimated $\Delta q/q$ becomes unacceptable for large models (see Figure 2.6, bottom line).

It has been noted already that the Hackett/Wilsden method may be regarded as an extension or generalization of the Hensel method. It may also be shown that the present method, implemented via the "ε_{max}" approach (Reference 3), exactly parallels Maskell's approach while avoiding both base pressure measurements and estimation of η. The relationship between the two methods will be examined further as part of the drag analysis in Section 7.

3.0 OUTLINE OF REFERENCED TESTS

3.1 General Comments

Figure 3.1 lists tests from which data was extracted for the present study. This list is not all-inclusive since certain of the tests listed are second attempts following earlier difficulties. For example, all data quoted herein for the 30" x 43" tunnel were taken after the stretched working section was installed: the earlier test section length was inadequate. The 1974 flat plate tests in the 16¼' x 23¼' tunnel employed an aft-sting mount (Figure 3.2), but were preceded by tests using vertical supports. Some of the latter data are quoted in Reference 1.

For the simpler models, a number of geometric copies were made and tested in the same tunnel. The smallest models were sized to give essentially free air data and the largest had an area of 10% or more of the tunnel cross section. Tunnel speeds were adjusted to yield the same Reynolds number range at each model size. Definitive data such as those quoted here have not been found in the literature for large models.

Powered models are generally too expensive for the multiple-model approach to be used. Scaling problems may also be encountered. Accordingly, large tunnel versus small tunnel comparisons were used, recognizing that differing turbulence characteristics, for example, can cause anomalies.

3.2 Tests on Unpowered Models

Normal flat plates were tested in the 16¼' x 23¼' tunnel for S/C values ranging from 2.38% to 9.53%. All had sharp edges, chamfered from the rear and were sting-mounted centrally from the rear (see Figure 3.2). The horizontal sting was mounted to the standard virtual center tunnel balance via a vertical strut which was shielded from the mainstream. Base pressures were measured both on the plate aft surface and within the bubble, using a boom (see Figure 3.2) introduced only during pressure measurements.

Other normal plate tests are included as a special case of the flat plate wing tests (Figure 3.3). These plates had a half-wing aspect ratio of 1.5 and ranged from 1.56% to 16.74%, of the 30" x 43" tunnel cross-section. An under-floor balance was again used, great care being taken in scaling the base plates and floor clearances. No attempt was made to remove the floor boundary layer and, in consequence, data for the smallest model were inferior to the remainder. Increased speeds, used to equalize Reynolds number across the model spectrum, evidently failed to thin the floor boundary layer adequately for the smallest model, W1.

For compatibility with the flat plate tests, a 50% mounting location was used and measured pitching moments were re-referenced to quarter-chord during data reduction. The lift performance of the plates, being sharp edged, was of course modest and the addition of leading edge roundings had little effect. Three spheres, of 8.5, 12.0, and 15.0-inches diameter were fabricated. Figure 3.4 shows the 15-inch sphere mounted in the 30" x 43" wind tunnel. The spheres were constructed from laminated mahogany and hollowed out for lightness and access to instrumentation. Each sphere was fitted with 14 surface pressure orifices and was mounted on a 3/4-inch diameter strain-gauge balance. The sphere was chosen as the solid object model (vis-a-vis flat plate) for continued blockage method verification tests because its free-air properties are well known and are markedly different at sub- and supercritical Reynolds numbers. Furthermore, its potential flow aerodynamics are simple analytically. The two larger spheres were tested in the Lockheed 30" x 43" tunnel under blocked conditions. All three spheres were tested at essentially free-air conditions in the Lockheed 16¼' x 23¼' tunnel. In some of the latter tests, static pressures were also measured at a location corresponding to the roof centerline in the smaller tunnel. These data were used to test pressure correction procedures (Section 6).

3.3 Tests on a Powered Model

Powered model data quoted in the present report involved a straight-winged knee-blown flap model which had a flap upper surface angle of 76 degrees. Dimensional details are given in Figure 3.5. The wing has a span of 76.2 cm

(30") with tips fitted and a tip chord of 12.78 cm (5.03"), giving a reference area of 973.8 sq. cm (1.048 sq.ft.). Tips-off reference dimensions are used throughout this report, as previously (Refs. 4 and 5). These are: span, 50.8 cm (20"); chord, 10.16 cm (4"); and area 516.1 sq. cm (0.556 sq. ft.). Full dimensional details and a detailed model description may be found in Reference 2. A general view of the model is given in Figure 3.6. The wing was mounted on a fuselage, which housed a three-component strain-gauge balance and air bridge. The sting was attached to an incidence quadrant mounted beneath the tunnel floor. Similar arrangements were used in the 7' x 10' NASA/AAMRDL tunnel. In the smaller tunnel, floor boundary layer control was available, for use at higher blowing rates, employing either a moving ground or a tangentially-blown ground. Descriptions of these devices and their application may be found in References 2 and 5. The same references give a detailed amount of calibration and test procedures used for the tests quoted herein.

4.0 MEASUREMENT AND ANALYSIS OF WALL PRESSURE SIGNATURES

4.1 Measurement of Wall Pressure Signatures

Surface pressure orifices are installed in the tunnel sidewalls, in the tunnel roof and possibly along the tunnel floor along their respective centerlines. Longitudinal spacing should be between 5% and 10% of tunnel width, with larger spacings towards the downstream end of the test section. The recommended model position, where an option exists, is about one-third of test section length from the forward end. A relatively long test section is desirable, preferably about 1.5 times tunnel width.

Well-made orifices are required, drilled in metal and free from burrs. Individual discs may be inserted in large tunnels. Continuous pressure tapped strips may be more convenient in small tunnels. An example of the latter may be seen in the tunnel roof in Figure 3.4. Discs are set into the far wall. Orifices are also drilled directly into the plexiglass windows in this tunnel.

When run time is not at a premium, a single scanivalve is usually sufficient for pressure measurements. However, in a production tunnel or where long tube runs would cause undue pressure lags, individual transducers may be used. The latter approach is used in the Lockheed $16\frac{1}{4}' \times 23\frac{1}{4}'$ tunnel.

If flow unsteadiness is present, long-time averages should be taken over a period of several fluctuation cycles. In setting up and calibrating the instrumentation it should be noted that C_p excursions may be as little as .02, for low-drag models, or as much as 1.5 for large, bluff objects (see Figure 4.1). With care and good instrumentation, adequate accuracy can be achieved without changing transducers.

A datum set of tunnel wall pressure measurements should be made with the tunnel empty, prior to model installation. Experience has shown that it is preferable to gather these data at the approximate test value of q.

Figure 4.1 illustrates a number of features characteristic of the pressure signatures for relatively simple models. The test concerned was on flat plate wing W4 (Figure 3.3) set at various angles of attack. Since this is a floor-mounted half-model, blockage information may be derived solely from tunnel roof pressures.

Over the first 15-degrees of angle of attack, prior to wing stall, wall pressure disturbances are quite small and reflect predominantly viscous blockage. As the stall develops, the wall suction peak intensifies and moves back as the separation bubble broadens and elongates. This particular model is unusually large (16.7% S/C) and the wall suction peaks at 90-degrees angle of attack are substantial. For the 80- and 90-degree cases, pressure recovery is interrupted at $x/B = 0.6$, suggesting possible wall separation. However, wool tufts showed no evidence of this.

Figure 4.2 shows the effect of lift on measured sidewall pressure signatures. The pressure coefficients are uncorrected for empty tunnel irregularities, which show most clearly in the $\alpha = 0$ signatures. As the mid-height orifices were used, pressure increments due to lift were somewhat smaller than in the lower corners of the tunnel. Nonetheless, the signatures shown could be used to estimate lift interference using methods similar to those described herein for blockage estimation.

Figure 4.3 provides a further example of the way in which a wall pressure signature can indicate flow changes around a model, this time a sphere. At subcritical Reynolds numbers there is a substantial separation bubble which is reflected in the wall signature. At supercritical Reynolds numbers, the flow attaches and a marked decrease in wall suction is evident. This signature is close to that calculated for potential flow. The automatic response of the method to such flow changes is a major virtue.

4.2 Signature Analysis

The overall procedure for determining blockage parameters is described, in broad terms, in Section 2 and is illustrated in Figure 2.3. The purpose

of this sub-section is to describe the methods used in more detail. Figures A1 and A2 give an outline of the major elements of the signature analysis program. Appendix I gives a description from a user's point of view.

Generation of Basic $\Delta u/U_\infty$ vs. x/B Signature

Pressure coefficients measured at tunnel surfaces with the tunnel empty are first subtracted from corresponding model-present values measured at approximately the same 'q'. The resulting increment, C_p, is then converted to a velocity increment using the equation:

$$\frac{\Delta u}{U} = (1 - \Delta C_p)^{\frac{1}{2}} - 1 \ . \qquad (4.1)$$

Figure 4.4(a) shows a typical measured signature at this stage.

Resolution of Signature into Symmetric and Antisymmetric Parts

Resolution into symmetric and antisymmetric parts is an iterative process which starts with a trial estimate of the antisymmetric part. This is subtracted from the symmetric part and a test is made to determine whether the inflection point of the antisymmetric component coincides with the peak of the symmetric component. If the separation is too great, the wake source is moved to the peak location and the process is repeated. Up to five iterations are permitted. The individual steps in this process are described below.

Calculation of the Antisymmetric Signature

For an ideal signature measured in a long test section, $\Delta u/U_\infty$ asymptotes to zero upstream and to a constant value, determined by wake diameter, far downstream. The downstream asymptotic value $(\Delta u/U_\infty)_{MIN}$ is noted and an estimate is made for wake source position x . The model position is used initially. These are substituted, together with the assumed wake source span, b_w/B, into the equations

$$\left(\frac{\Delta u}{U_\infty}\right)_A = A_5 \left(1 + \tanh \left(A_6 \left(\frac{x_2}{B}\right) + A_7\right)\right)$$

where

$$A_5 = 0.5 \left(\Delta u/U_\infty\right)_{MIN}$$

$$A_6 = 3.30 + 0.2474 \text{ EXP } (7.8131\ b_w/B) \qquad (4.2)$$

$$A_7 = -A_6 \left(x_2/B\right)$$

$\left(\Delta u/U_\infty\right)_{MIN}$ represents the downstream asymptote of the signature.

Equations (4.2) are a curve-fitted approximation to the true line-source equation, which is too unwieldy for convenient manipulation. The constants involved in the A_6 equation are specific to a particular tunnel shape. The values quoted above are for a rectangular tunnel of 0.699 aspect ratio.

On the majority of occasions, the test section will be too short in relation to the model and its wake for the asymptote to be well established at both ends. Designated points may therefore be selected at the upstream and downstream ends of the signature. On the first pass through equation (4.2), these are assumed to be asymptotes. "Miss-distances" are next determined, between the designated points and the fitted curve and $\left(\Delta u/U_\infty\right)_{MIN}$ is adjusted so that the fitted curve intersects the designated points. This correction is made just once and is not iterated.

A special case occurs for highly-powered models. If tunnel flow breakdown occurs, a second peak may appear at an aft location. The program detects this situation by testing the slope of the line joining the designated downstream point to the preceding point. If the slope is greater than a particular positive value, a 'walking' procedure is started with x decreasing until a near-zero slope is found. This establishes the asymptote of Equation (4.2) at an ordinate corresponding to the minimum $\Delta u/U$ value between the two peaks. Wake blockage is probably overestimated in such cases and solid blockage is underestimated.

When the above process is complete, the fitted antisymmetric signature is subtracted from the measured signature leaving a bell-shaped symmetric curve-defined by experimental points [see Figure 4.4(b)].

Analysis of the Symmetric Signature

A least-squares curve fit procedure is used to fit a parabola to the uppermost points of the symmetric signature. Various checks are employed to ensure that the points selected both represent the peak properly and extend downward sufficiently far that Δx, the peak half-width, can be estimated with confidence. Figure 4.4(b) shows a parabola fitted to the upper part of a symmetric signature.

The most significant initial result from the parabolic fit process is the peak position x_p. If this is sufficiently close to the assumed wake source location, x_2, the source and sink parameters are calculated. Otherwise, the wake source location is suitably adjusted and a further iteration is performed.

Once the iteration has converged, adjusted values of $\Delta x/B$ and $(\Delta u/U_\infty)_{max}$ are determined for use with Charts I and II. These adjustments correct empirically for the fact that the parabola is only a rough fit to the true aerodynamic source-sink function. The parabola coefficients are defined by:

$$\Delta u/U_\infty = a\,(x/B)^2 + b(x/B) + c$$

From this we obtain:

Peak Position: $$x_p/B = -\,b/2a \tag{4.3}$$

Peak Value: $$(\Delta u/U_\infty)_{max} = 1.01\,\left[C + 0.5b\,(x_p/B)\right] \tag{4.4}$$

Semi-Width: $$\Delta x/B = 1.045\,\left[-(\Delta u/U_\infty)_{max}/2a\right]^{\frac{1}{2}} \tag{4.5}$$

The factors in (4.4) and (4.5) are the empirical adjustments (see above).

Determination of Flow Model Parameters

After the signature resolution has converged $\Delta x/B$ and b_s/B are input to Charts I and II, via a double interpolation routine, to obtain c_s/B, the source-sink spacing, and $\left(\Delta u/(Q_s/B^2)\right)_{max}$ which is used to obtain source strength. Non-dimensional solid/bubble source-sink strength is then obtained from

$$\frac{Q_s}{U_\infty B^2} = \frac{(\Delta u/U_\infty)_{max}}{\left(\Delta u/(Q_s/B^2)\right)_{max}} \tag{4.6}$$

Source-sink positions are given by

$$\left.\begin{aligned} \frac{x_3}{B} &= \frac{x_p}{B} - \frac{1}{2}\frac{c_s}{B} \\ \frac{x_4}{B} &= \frac{x_p}{B} + \frac{1}{2}\frac{c_s}{B} \end{aligned}\right\} \tag{4.7}$$

b_s/B is assumed to be the same as b_w/B, which has already been estimated, so the source-sink system is now fully defined.

Non-dimensional viscous wake blockage source strength is given by

$$\frac{Q_w}{U_\infty B^2} = 2\,A_5 \cdot \frac{C}{B^2}$$

where C is tunnel area.

The wake source position, x_2/B and span b_w/B were obtained during signature analysis.

We now have three source strengths $(+Q_s/U_\infty B^2)$, $(Q_w/U_\infty B^2)$ and $(-Q_s/U_\infty B^2)$, all of span (b_s/B), situated at locations (x_3/B), (x_2/B) and (x_4/B).

Determination of Centerline Interference Signature

The total centerline signature is built up from three components, one for each source or sink, as illustrated in Figure 4.5. To determine each component at position x/B, the relative source location $(x/B - x_n/B)$ is determined and input to Chart III to give $\Delta u/(Q/B^2)$. Multiplication by the appropriate normalized source strength $(Q/U_\infty B^2)$ then yields the desired interference velocity $(\Delta u/U_\infty)$ on the tunnel centerline. The three components are added and the calculation is repeated for each specified x-station.

Check on Curve Fit to Wall Measurements

A recent addition to the program is a routine which determines the entire wall signature implied by the flow model parameters determined above. It is not essential to determine this curve, but it can be helpful if unfamiliar or unexpected results occur.

The new routine again makes use of the tanh function fit using the equation

$$\Delta u/U_\infty = A_1 \tanh\left(A_2 \frac{x}{B} + A_3\right) + A_1 \tanh\left(-A_2 \frac{x}{B} + A_4\right) + A_5\left(1 + \tanh\left(A \frac{x}{B} + A\right)\right) \qquad (4.8)$$

where

$$\left.\begin{aligned} A_1 &= 2\,(Q_s/U_\infty B^2)\,(B^2/C) \\ A_2 &= A_6 \qquad \textit{(see Equation 4.2)} \\ A_3 &= -A_2\,(x_3/B) \\ \text{and} \quad A_4 &= +A_2\,(x_4/B) \end{aligned}\right\} \qquad (4.9)$$

A_5, A_6, and A_7 are given by equation (4.2).

5.0 EFFECTIVE MODEL SHAPE

5.1 Introduction

For each set of aerodynamic parameters derived from wall pressures there is an implied body shape. It is not necessary to determine outlines of these bodies routinely, but useful insight can be gained from them in some cases. Calculated shapes can be compared with model dimensions and observed separation bubbles. In-tunnel versus free air comparisons can be used to make a rough assessment of tunnel-induced changes in separation bubble shape.

The equations for the full, two-line-source plus line sink bodies are complex and most of the present studies have been restricted to the axisymmetric shapes generated by point sources and sinks placed in a uniform mainstream.

Continuity considerations lead to the following equation for the body radius, r:

$$f(r) = \frac{1}{2} r^2 - \sum_{n=1}^{3} \frac{Q_n}{4\pi U_\infty} \left[1 + \frac{(x - x_n)}{\left((x - x_n)^2 + r^2\right)^{\frac{1}{2}}} \right] = 0 \qquad (5.1)$$

where Q_n and x_n may be interpreted in terms of $\pm Q_s$ and Q_w and their positions. Thus, Q_1 and Q_3 become $\pm Q_s$ and Q_w replaces Q_2. The x subscripts follow accordingly. Equation (5.1) was solved, for r, on an HP29C hand calculator using Newton's method in the form

$$r_{i+1} = r_i - \delta_i \left[\frac{f(r_i + \ _i)}{f(r_i)} - 1 \right]^{-1} \qquad \text{where } \delta_i = 10^{-5} r_i .$$

The downstream asymptote of the body is given by

$$r_\infty = \sqrt{\frac{Q_w}{\pi U_\infty}} . \qquad (5.2)$$

Equation (5.1) is not suitable for determining the location of the front stagnation point, x. This is given by:

$$f(x) = 1 - \sum_{n=1}^{3} \frac{Q_n}{4\pi U_\infty} \cdot \frac{(x_s - x_n)}{ABS(x_s - x_n)} \cdot \frac{1}{(x_s - x_n)^2} = 0 \ . \qquad (5.3)$$

The above equation is a sextic, having four real and two imaginary roots in most cases of interest. The lowest x root corresponds to the front stagnation point. The same solver was used as for Equation (5.1).

5.2 Calculated Body Shapes

For zero solid blockage, equations (5.1 through (5.3) yield the outline of an axisymmetric source body, strength Q_w in a mainstream U. Figure 5.1(a) shows a number of wake bodies so derived for various wake strengths. Effective bodies for purely solid blockage ($Q_w = 0$) are shown in Figure 5.1(b). These two sets of bodies represent extreme cases between which most experimental cases will be found.

Figure 5.2 shows sample cases which lie between the above extremes. Equal values of Q_w and Q_s produce shapes similar to blunt-ended rods [Figure 5.2(a)] which develop bulbous ends as relative wake strength diminishes [Figures 5.2(b) and (c)].

Each profile in Figures 5.1 and 5.2 requires numerous solutions to Equation (5.1) and this precludes quick, routine estimates. Figures 5.3 and 5.4 have therefore been prepared which give the major dimensions of the source-source-sink bodies. A reasonable approximation to the body outline may be obtained by drawing an ellipse with semi-axes R_2 and Δx and fairing it into a cylinder of radius R_1, obtained from equation (5.2).

5.3 Comparisons for Tested Models

Figure 5.5 shows effective shapes derived from wall pressure signatures for the 15-inch sphere in the 30" x 43" wind tunnel. Considering that only

three point singularities are used, the effective shapes blend with the model outline very well. The change in wake character through transition is well depicted and the thinning of the supercritical wake is very marked. It is interesting to note that the subcritical wake occupies 24.9% of the tunnel cross-section, at maximum diameter, compared with 13.7% for the model itself.

Generally similar results are obtained for a circular disc mounted normally to the flow (Figure 5.6). It is noteworthy that the calculated body diameter at the model station closely equals the disc diameter.

Figure 5.7 shows effective model shapes derived for a less symmetrical model, an idealized automobile. It is apparent that when the model is yawed, the present method responds appropriately by shortening the effective body and increasing its radius. The ratio of maximum source-sink body area to projected model frontal area is 0.738 at zero yaw and 0 737 at 30-degrees. If the wheel projections are subtracted from the zero-yaw frontal area, to give an approximate maximum cross-section, the ratio becomes 0.814. The supercritical sphere had a corresponding area ratio of 0.854.

In the subcritical sphere case [Figure 5.5(a)], the calculated wake occupies a substantial proportion of the tunnel area and it appears probable that interference will distort it. To estimate the magnitude of the change, U_∞ in Equation (5.1) was replaced by a value which included the tunnel-induced axial velocity at the x-station concerned. Figure 5.8 shows that the bubble outline is changed surprisingly little. As the model is very large in comparison with those for most routine tests, this suggests that blockage-induced distortion of separation bubbles is not likely to be a limiting factor. Effects on pressure distribution and implications regarding separation location will be discussed in Sections 6 and 7.

6.0 CORRECTIONS TO MEASURED PRESSURES

6.1 Simultaneous, Whole-Model Corrections

In the preceding sections, methods have been described for defining tunnel-induced changes in model environment in terms of changes of velocities u, v and w at points distributed over the surface of the model. As we have seen, the predominant effect of blockage is to increase u. A simple increase presents no correction problem. Pressure coefficients can be renormalized simply and a correction to Reynolds number will ensure that viscous phenomena are properly defined. However, there are usually significant changes in interference velocity along the model length. In situations involving sensitive viscous effects — incipient separation, rapidly moving separation or transition — these gradients may render the tunnel data uncorrectable. An implicit assumption, in correcting in-tunnel pressure measurements, is therefore that there are no sensitive viscous phenomena and, moreover, that tunnel gradient-induced changes in boundary layer thickness are small.

Within the above framework, there are several levels at which corrections may be made. These range from a mathematically represented model surface with full and simultaneous application of the boundary conditions to simple superposition methods. The former, whole-model corrections will be reviewed in this section. Simpler, more practical methods are discussed in Section 6.2.

To illustrate the application of blockage corrections simultaneously to a complete model, a Douglas-Neuman, source-panel model was set up of the 15-inch sphere. The total spherical surface was represented using 648 10-degree by 10-degree panels. For economy, only one quarter sphere (seen from the front) was modeled explicitly and imaging techniques were used to model the effects of the remaining panels.

The objective of the ensuing calculation was to calculate in-tunnel pressures on the sphere surface and compare them with measurement. The source and sink image system determined from an experiment at supercritical Reynolds number was used to calculate the three components of interference velocity at

each panel center. These velocities were input to the source panel program together with sphere panel geometry and mainstream velocity. Figure 6.1 shows the resulting pressures at the sphere equator together with the corresponding uncorrected measurements. The agreement over the forward part of the sphere is excellent. There are local effects evident in the experimental data further aft, but the theory reproduces the general trend well as far back as the separation point, at about 140-degrees. A similar correlation was obtained in a vertical plane, where the peak C_p's were almost the same as in Figure 6.1.

An extension of the above study could be made in which the effective viscous wake surface [Figure 5.5(b)] is paneled and blended into the sphere. Improved correlations in the 120- to 130-degree region would probably result. However, such a detailed approach is not usually justified.

The above study demonstrates that simultaneous, whole model corrections predict tunnel effects well for models with predominantly attached flow. The calculations also provide a baseline against which simpler methods can be assessed.

6.2 Approximate Method

Figure 6.2 examines the components of interference velocity and their impact upon surface pressures. For this study, a potential flow sphere was used, represented by the previous paneled sphere inside the tunnel, and a system of doublet images to represent the effects of the tunnel boundaries. It is evident that axial interference components maximize at about 5% at the sphere crest, vertical velocities are greatest — about 0.6% — at the 45-degree location. The interference velocities are not tangential to the surface, except at the crest. At the front stagnation point Δu is, of course, normal to the surface.

Figure 6.2(b) shows the corresponding surface pressure increments. Three sets of data are shown, for separate calculations involving all three increments (filled circles), transverse components only (triangles) and the axial

component, Δu only (crosses). As has already been noted, the Δu component has a dominant effect. In fact, in a corresponding plot for the equatorial position, the effect of the transverse components cannot be seen.

It is obviously very desirable to correct measured pressures on a point-by-point basis, rather than globally, as described previously. Bearing this in mind the small spread in points in Figure 6.2(b) and the very large model concerned, it is also apparent that it will generally be sufficient to concentrate on the Δu component. Further simplification is afforded if variation in Δu across the test section is assumed small (Figure 2.5). Only the centerline increments found in the standard blockage computation are then required.

The simplest point-by-point C_p correction would be to superpose the tangential component of Δu on $\sqrt{1 - C_p}$ and recalculate the pressure coefficient. This does not work because there is an implicit assumption that the mainstream flow component at the sphere surface is affected but the doublet strength is not. In the case of the potential sphere, it is clear that, if $+\Delta u$ is present at the front of the sphere the stagnation point will move back unless the sphere doublet strength increases. It is evident that sphere doublet strength must be scaled up by a factor $(U + \Delta u)/U$ to restore the stagnation point to its correct location. Since this factor is also applied to mainstream velocity, it is obviously directly applicable to measured surface velocities, at least for cases with Δu constant over the model length.

Thus, if q_θ is the local surface velocity in free air, we may write, for uniform Δu

$$C_{p_c} = 1 - \left(\frac{q_\theta}{U_\infty}\right)^2 \tag{6.1}$$

in free air and

$$C_{p_u} = 1 - \left(\frac{q_\theta}{U_\infty}\right)^2 \left(1 + \frac{\Delta u}{U_\infty}\right)^2 \tag{6.2}$$

in the tunnel. Equation (6.2) may be written as

$$\left(\frac{q_\theta}{U_\infty}\right)^2 = \frac{1 - C_{p_u}}{\left(1 + \frac{\Delta u}{U_\infty}\right)^2}$$

and on substituting into (6.1) this gives

$$C_{p_c} = \frac{C_{p_u} - 1}{\left(1 + \frac{\Delta u}{U_\infty}\right)^2} + 1 \,. \tag{6.3}$$

If Δu is not constant along the axis, we may postulate a "local mainstream" effect in which $\Delta u/U$ in (6.3) is a function of x. Thus

$$C_{p_c}(x) = \frac{C_{p_u}(x) - 1}{\left(1 + \frac{\Delta u(x)}{U_\infty}\right)^2} + 1 \tag{6.4}$$

To test the method, in-tunnel C_p's calculated with Δu, Δv and Δw present [Figure 6.2(b)] were corrected using Equation (6.4) and compared with a corresponding free-air calculation. The results are tabulated below.

θ°	5	15	25	35	45	55	65	75	85
$\Delta U/U_\infty$	.0385	.0390	.0399	.0413	.0432	.0454	.0476	.0495	.0506
C_{p_u}	.9775	.8417	.5755	.2208	-.1956	-.6212	-1.0045	-1.2955	-1.4530
C_{p_c} *	.9791	.8532	.6106	.2803	-.1005	-.4862	- .8303	-1.0877	-1.2276
$C_{p_{Free}}$	.9786	.8502	.6034	.2694	-.1133	-.4968	- .8350	-1.0859	-1.2191
ERROR	+.0005	+.0030	+.0126	+.0109	+.0128	+.0106	+.0047	+.0028	+ .0085

Using equation (6.4).

The errors in applying equation (6.4) to sphere crest pressures are .013, in C_p, at most. Around the equator, a similar calculation shows errors less than .005 at all positions.

Bearing in mind the large size of the model used for checkout, it may be concluded that equation (6.4) corrects measured pressures sufficiently accurately for most practical purposes.

6.3 Pressure Correlations on the Model Surface

Sphere Tests

Figure 6.3 shows tunnel centerline interference velocities calculated from ceiling pres ure distributions for Reynolds numbers through the critical range. At subc ' cal Reynolds numbers the tunnel centerline blockage velocity increases continuously from about 4% to more than 10% over the chord of the sphere. The blockage maximizes just aft of the sphere, at the location of the crest of the separation bubble. The strong variation of blockage makes the choice of characteristic velocity, for Reynolds number determination, conjectural. For the present work, the corrected velocity corresponding to the suction peak location has been used. A further difficulty arises because the subcritical sphere evidently has a significant favorable pressure gradient imposed upon it by blockage effects. This raises the possibility that the critical Reynolds number will change.

At supercritical Reynolds numbers blockage velocities are about half as large as in subcritical cases and vary much less over the chord of the sphere.

Figure 6.4 shows pressures measured on the surface of the 15-inch sphere in the 30" x 43" wind tunnel, designated C_{p_u} and in the 16¼' x 23¼' wind tunnel, designated C_{p_∞}. Blockage increases both the peak and the wake suctions very significantly in the small tunnel. Correction via equation (6.4) leads to good correlation except that large tunnel peak suction is slightly higher. However, this is consistent with the slightly higher Reynolds number involved.

The results of a corresponding correction at a supercritical Reynolds number is shown in Figure 6.5. In this case the Reynolds numbers were better

matched but wake suctions are again slightly higher in the smaller tunnel. There are also some detailed differences just aft of the sphere's crest.

Figures 6.6 and 6.7 show peak suction and base pressure respectively as functions of Reynolds number through the critical range. In both cases, the corrections to small-tunnel Reynolds number use velocity increments, $\Delta u/U_\infty$, calculated at the peak C_p locations, which are quite close to the sphere center in most cases. Pressure coefficients are calculated via equation (6.4) using the same value of $\Delta u/U_\infty$. Application of these corrections increases the value of Reynolds number and decreases suction coefficients (see Figure 6.6).

In both the fully subcritical and the fully supercritical Reynolds number ranges both tunnels indicate similar trends but transition to the supercritical characteristic is earlier in the large tunnel. However, examination of the base pressure characteristics, in Figure 6.7, shows no significant difference between critical Reynolds numbers in the two tunnels. With the exception of the $C_{p_{min}}$ curve for the large tunnel, Figures 6.6 and 6.7 show critical Reynolds numbers which agree both between tunnels and with accepted turbulence sphere results.

The above comparisons indicate that for a sphere occupying 13.7% of the tunnel cross-section, application of pressure corrections via equation (6.4) produces results comparable with and no less credible than results from similar tests in a large tunnel. In correcting both pressure coefficients and Reynolds number, interference velocities calculated at the peak suction location were employed. Model center values would be a reasonable approximation to this.

Test on Idealized Automobile Shape

In 1978, experiments were carried out, under joint Lockheed/Ford Motor Company auspices, on models of an idealized car. Tests were run in the Lockheed 16¼' x 23¼' tunnel on a "full size" (frontal area = 5.65% of tunnel area), on a 0.475, and on a 0.375 scale model (see Ref. 6). Figure 6.8 shows the profile in side view. The metal models were very accurately made and were

extensively pressure plotted. Design was simplified so that many surfaces were flat, being joined by simple radii or sharp edges as appropriate.

Figure 6.8 shows measured pressures at the centerplane for all three models. Floor blowing boundary layer control was used to give a uniform velocity profile near the ground and tunnel speed was adjusted to give the same Reynolds number in all three cases. Pressure signatures were measured along the tunnel ceiling and processed as described previously.

Figure 6.9 shows the previous data after correction via the present method. In this case the model blockage was small enough that a constant value of $\Delta u/U$ could be used at all locations. The peak Δu was used. Slight overcorrection is evident in some regions, but the overall correlation between models is excellent.

6.4 Pressure Correlations at Off-Body Points

In the immediate vicinity of the model it is appropriate to correct pressures in the manner just described. However, in the far field, there is another option by which off-body pressures may be deduced directly from the source-sink system derived from wall pressure signatures To demonstrate this, static pressures were measured in the large wind tunnel, in the presence of the 15-inch sphere, at locations corresponding to the small tunnel wall and ceiling orifice rows. Attempts were then made to predict the large tunnel ("free air") pressures from the small tunnel data.

To apply the direct method, source and sink strengths and locations are derived from wall pressure signatures, but no attempt is made to correct the signatures themselves. Instead, velocities induced in free air by the source-source-sink system are calculated at the desired, off-body, far field locations. These are converted to pressure coefficients and give the results indicated by crosses in Figures 6.10 and 6.11. At the wall position, correlation between large tunnel measurements (circles) and the predicted pressures is very good. Suction is underpredicted slightly at the ceiling.

An alternative method of determining free-air far field pressures is to correct in-tunnel measurements at the same locations, if these are available, using equation (6.4). For consistency with the previous calculation 'measured' C_p's at the tunnel wall and ceiling were recreated using the source-source-sink model and its tunnel image system. "Empty tunnel" $\Delta u/U$ values were computed at the orifice locations and used to correct the 'measured' C_p's via equation 6.4. The results of these calculations are given by the plus symbols in Figures 6.10 and 6.11. The suctions are systematically lower than were given by the 'direct' calculation. This difference arises because, in applying the 'direct' method, the source and sink strengths were not adjusted to an equivalent, free air value. Such an adjustment is implicit in equation (6.4).

There remains a question concerning the differences between suctions deduced from small tunnel data and those measured in the large tunnels. In the discussion on body shape, in Section 5, it was noted that the equivalent body in the small tunnel was slightly more slender than the free-air body, due to tunnel induced bubble distortion at subcritical Reynolds numbers. This may be the reason for the small tunnel/large tunnel differences observed in Figure 6.10. With the exception of one point, the supercritical data (Figure 6.11) agree quite well.

It may be concluded that pressures measured at off-body points may be corrected via equation 6.4. If measured pressures are unavailable, the 'direct' method may be used to generate new data from the source-source-sink model derived from wall pressures. The latter method is inapplicable in the near field because the source-source-sink body is too crude a representation of the actual flow.

7.0 CORRECTIONS TO DRAG

7.1 Introduction

If detailed measurements are available of pressures or of forces on components, correction on a point-by-point or individual component basis is to be preferred. Failing this, local information can be considered when estimating effective model position. However, in many cases only balance data will be available and additional reliance must be placed upon wall pressure signature information. The possibilities in this regard are extensive but have not been explored fully. However, it will be seen below that gradient effects due to wake blockage can be estimated accurately solely from wall pressure measurements.

Figure 7.1 shows the sequence in which drag corrections are made. The major corrections are for "horizontal buoyancy" effects which arise from wake blockage and to dynamic pressure for changes caused by both wake and solid blockage. In keeping with the above sequence, subsections 7.2 and 7.3 will concern horizontal buoyancy and dynamic pressure corrections respectively. Applications to flat plate and sphere data will be shown in subsection 7.4. Treatment of lifting models is deferred to Section 8.

During the present research, it was noticed that one form of the present correction method is equivalent to Maskell's wake blockage method (Reference 10). This relationship will be discussed in subsection 7.5.

7.2 "Horizontal Buoyancy" Correction

Conventional Methods

Empty tunnel or model-induced pressure gradient is frequently assumed to be constant over the model length. Buoyancy drag is then determined as the product of normalized pressure gradient and model volume. If the pressure gradient is not constant the same result may be applied to an element thickness δx and area $A(x)$. δx to give an incremental buoyancy drag

$$\delta C_D = - \frac{A(x)}{S} \frac{dC_p}{dx} dx$$

For the whole model

$$\Delta C_D = - \int_{\text{Model Length}} \frac{A(x)}{S} \frac{dC_p}{dx} dx$$

This may be written

$$\Delta C_D = - \int_0^1 \Delta C_p(x) d\left(\frac{A(x)}{S}\right) \qquad (7.1)$$

where the integral includes both forward and aft facing surfaces. $\Delta C_p(x)$, the blockage-induced pressure on the model surface, may be determined by one of the methods described in Section 6.

The "pIQ" Method

If model surface pressure measurements are unavailable or are inadequate for applying (7.1) accurately, an alternative approach may be taken. As was seen in Section 5, each source-source-sink combination determined from wall pressures may be used to generate an effective body with a defined area distribution and with defined pressures on its surface. In principle, the body shape, its pressures and its tunnel induced increments could be calculated and equation (7.1) could be applied. However the same result is obtained much more easily by considering the drag of the sources and sinks themselves. Using the notation shown in Figure 7.2, this gives

$$\Delta D_{MODEL} = \rho(-\Delta u_s^+ Q_s - \Delta u_w^+ Q_w + \Delta u_s^- Q_s) \qquad (7.2)$$

The equivalence between equation (7.2) and the integral of the outer surface pressures may be proved by constructing a control volume with an indented contour extending forward from the rear of the body and enclosing each point source with a sphere which isolates the singularity. Consideration of horizontal momentum then yields the above result.

If we consider the entire, closed body in Figure 7.2 and recognize that its (potential flow) drag is zero, we may write

$$\Delta D_{NET} = \rho(-\Delta u_s^+ Q_s - \Delta u_w^+ Q_w + \Delta u_s^- Q_s + \Delta u_w^- Q_w) = 0 \qquad (7.3)$$

Equation (7.3) may be used to simplify (7.2), giving

$$\Delta D = - \rho \Delta u_w^- Q_w$$

We also note that Δu_w^- is half the astmptotic velocity Q_w/BH, thus

$$\Delta D = - \tfrac{1}{2}\rho \frac{Q_w^2}{BH}$$

or

$$\Delta C_D = - \frac{BH}{S} \left(\frac{Q_w}{U_\infty BH} \right)^2 \qquad (7.4)$$

For non-rectangular tunnels, BH is replaced by tunnel area in the above equations.

Applications to a Sphere

In what follows, a test example is set up and is used to compare various methods for calculating horizontal buoyancy drag. The example chosen concerns a hypothetical sphere over which attached flow is enforced in the presence of an externally imposed pressure gradient. This is induced by a set of wind tunnel images chosen from a typical experiment and has the general form illustrated in Figure 7.2. Because the flow is attached, a source-panel method may be used to determine the external pressure distribution, which is then integrated to yield a baseline value of buoyancy drag. Four additional methods are evaluated against this baseline.

(i) Baseline (Panel Method)

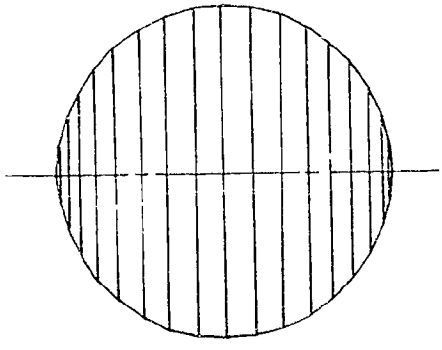

a) Panel sphere with source sheets
b) Apply tunnel-induced supervelocities
c) Enforce tangency at sphere surface
d) Determine pressures
e) Integrate drag component of external pressure

Result: $\Delta C_D = \underline{\underline{0.0216}}$

(ii) Conventional Buoyancy Calculation (Figure 7.3)

$$\Delta C_D = - \frac{\text{VOLUME}}{\text{REF. AREA}} \frac{d(\Delta C_p)}{dx}$$

where $\Delta C_p = 2\Delta u/U$

Result: $\Delta C_D = \underline{\underline{0.0140}}$

iii) Use of Model Area Distribution (Figure 7.4)

$$\Delta C_D = - \int \Delta C_p(x) \, d\left(\frac{A(x)}{S}\right)$$

where $\Delta C_p = 2\Delta u/U_\infty$

Result: $\Delta C_D = \underline{\underline{0.0136}}$ at 45° position

(iv) Model Area Distribution Plus C_p's Using Eqn. (6.4) (Figure 7.5)

$$\Delta C_D = - \int \Delta C_p(x) \, d\left(\frac{A(x)}{S}\right)$$

where, from (6.4), $\Delta C_p = C_{p_c} - C_{p_u} = (C_{p_u} - 1) \dfrac{\left[1 - \left(1 + \left(\frac{\Delta u}{U}\right)\right)^2\right]}{\left(1 + \left(\frac{\Delta u}{U}\right)\right)^2}$

Result: $\Delta C_D = \underline{\underline{0.0202}}$ at 45° position

(v) The "ρUQ" Method

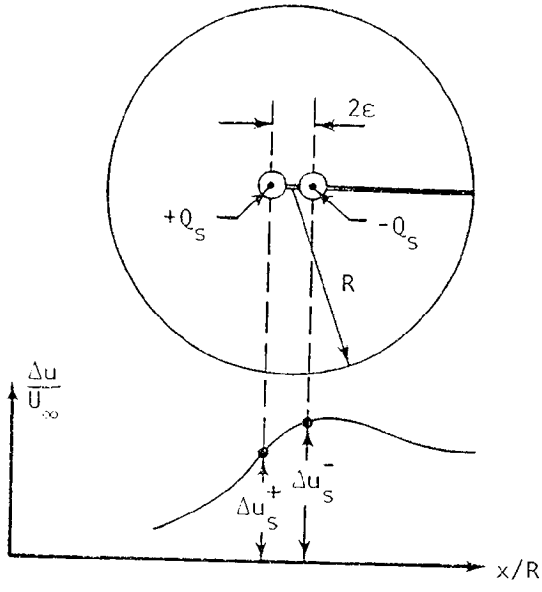

Isolate the singularities and perform drag integration over indented contour.

$$\Delta D = \lim_{\varepsilon \to 0} \left(-\Delta u_s^+ + \Delta u_s^-\right) Q_s$$

$$= \rho\mu \frac{d(\Delta u)}{dx} \text{ where } \mu = 2\varepsilon Q_s$$

$$\Delta C_D = \frac{2\mu}{\pi R^3 U_\infty} \frac{d(\Delta u/U_\infty)}{d(x/R)} \qquad (7.5)$$

Result: $\Delta C_D = \underline{0.0210}$

The above examples show that conventional blockage gradient corrections must be applied carefully, to obtain accurate results. In particular, equation (6.4) should be used to determine surface pressure increments, since linearization degrades accuracy seriously. Where model surface pressure measurements are unavailable, the above comparisons show that the application of "ρUQ"-type methods give results which agree with the exact Douglas Neumann approach. Equation (7.4) may therefore be employed with confidence for evaluating buoyancy drag.

7.3 Dynamic Pressure Correction

For non-lifting models, dynamic pressure corrections are applicable solely to viscosity-dependent drag, including base drag. Viscous forces are distributed along the model length non-uniformly and if solely balance data is available it is necessary to find an effective model location at which blockage velocity is evaluated. This may be difficult because the choice of location involves conflicting requirements.

For simple configurations it may be possible to calculate effective model position with some confidence. Thus for a streamwise flat plate with laminar flow, skin friction varies as $x^{-0.5}$ and it can be shown that the local skin friction coefficient at 25% chord equals the value for the whole plate. For a wholly turbulent plate, with $x^{-0.2}$ dependence, the corresponding location is at 32.8% chord.

It is possible, in principle at least, to extend the above approach to more complex model shapes. However, skin friction and wetted periphery estimates would be needed, as functions of x, and such an approach would be impractical in most test situations. In many cases a specific model location is defined by lift center, and this usually will be of overriding importance. Thus, the quarter chord is the obvious effective location for an unstalled simple wing. As stall occurs, it would be logical to move the effective location rearward in consonance with the lift. A constant, nominal model position has been retained in the cases treated so far.

The following equation is recommended for correcting drag coefficient. It includes both buoyancy and dynamic pressure terms

$$C_{D_c} = \frac{C_{D_u} - \Delta C_D}{(1 + \varepsilon_M)^2} \tag{7.6}$$

where ΔC_D the buoyancy increment is given by (7.4) and ε_M is the value of $\Delta u/U_\infty$ at the model position.

7.4 Correlations for Flat Plates and Spheres

Normal Flat Plates

Figure 7.6 shows measured and corrected drag coefficients for 3-, 4-, 5- and 6-foot square plates tested in the 16½' x 23½' wind tunnel. These experimental results were previously reported in Reference 1. An early correction procedure, known as the "ε_{max} method" was reported in this reference. This is

based upon maximum observed interference velocities. Additional corrected results using the "ρUQ" method [Equation (7.4)] are included in Figure 7.6. It is evident that the newer method yields corrections which are slightly smaller than before. Nonetheless the corrected drag coefficients agree quite well with accepted flat plate drag values, though they are about .03 higher than the value quoted by Hoerner.

Figure 7.7 presents new results for floor-mounted rectangular plates. Up to 0.1 S/C, the general trends are similar to before. Drag coefficients are again slightly higher than the Hoerner value. For W4, the largest plate, the uncorrected drag coefficient is almost double the corrected value and the fact that the variation with S/C is no longer linear is probably significant. The results show that the 'ρUQ' method can be applied successfully to models with cross sections of at least 10% of tunnel area and which have highly separated flow.

Spheres

Maxworthy (Reference 1) reviews sphere tests by a number of workers and shows wide variations in the drag versus Reynolds number characteristics. In certain cases, it is claimed that tunnel constraint is the cause. The present large tunnel tests, for which blockage effects were negligible, indicate that the observed variations arise from bistable flow characteristics which are inherent to sphere aerodynamics. Blockage-corrected small tunnel tests confirmed this.

In the present tests the spheres were smooth and no attempt was made to trip the boundary layer. The turbulence level in both the small (30" x 43") and the large (16½' x 23½') tunnels was in the 0.3 to 0.5% range, increasing with Reynolds number. The turbulence scale was smaller in the smaller tunnel. At the time of testing, the spheres were considered "difficult" models because repeatability was difficult to achieve. Subsequent detailed analysis showed bistable flow conditions over most of the test range of Reynolds numbers. In the small tunnel this caused speed control problems which made it very difficult to define transition for the large sphere. Further surge problems were noted with supercritical flow fully established.

Figures 7.8 and 7.9 show drag variation with Reynolds number for the 12- and 15-inch spheres. With the exception of the broken line in Figure 7.8, which shows the uncorrected characteristic, all small tunnel data have been corrected using equation (7.6). In early analyses data appeared unrepeatable, unreliable and generally confusing. Only after correcting the small tunnel data properly, only after considering both tunnels and both spheres simultaneously and only after considering point sequence as well as position did a clear picture emerge. The major problem in data analysis was that hysteresis appeared over the entire test range of Reynolds numbers. In certain instances — notably the 12-inch sphere in the large tunnel — it did not appear because it evidently was not provoked. In the small tunnel, transitional hysteresis could not be detected because of speed control problems. The table below summarizes the hysteresis observations:

TUNNEL	SPHERE	SUBCRIT. R_e	TRANSITION	SUPERCRIT. R_e
30" x 43"	12"	H?	SPEED CONTROL PROBLEMS	H
	15"	H		SPARSE DATA
16½' x 23½'	12"	HYSTERESIS NOT INDICATED	H	HYSTERESIS NOT INDICATED
	15"	H	H	H

H: HYSTERESIS PRESENT

Against the above background, the differences between tunnels due to constraint, due to tunnel-induced changes in the viscous flow or due to turbulence scale, are minor. The 12-inch sphere data show a somewhat differing characteristic in the two tunnels, subcritically (Figure 7.8) but the differences are within a credible hysteresis band (Figure 7.9). Transition in the small tunnel came halfway across the hysteresis loop observed in the large tunnel Drag coefficient at the lower bound of the supercritical bistable region in the small tunnel was slightly above the observations made in the large tunnel.

The 15-inch sphere had a slightly more 'peaky' subcritical drag characteristic than did the 12-inch sphere but large tunnel and corrected small tunnel data defined the same hysteresis boundaries in this region. Transitional and supercritical data were sparse in the small tunnel. There was reasonable agreement regarding transition Reynolds number but large tunnel supercritical drag levels appear high. The small tunnel supercritical 15" sphere drag level, after correction, agrees with the large tunnel 12" sphere data.

Because of the difficulties just described, it is tempting to suggest, in retrospect, that the sphere was not a good candidate for checking the blockage correction procedure. However this is not so, because the difficulties encountered here would also be found in many wing-stall situations, for example. The preceding analysis shows that the new correction method worked well and was, in fact, the least of the problems encountered. Corrected data from even the large, 15-inch sphere in the 30" x 43" tunnel is considered at least as reliable as the large tunnel data at subcritical, transitional and at supercritical Reynolds numbers.

7.5 The "ε_{max}" and Maskell Methods

Reference 3 describes two early methods of implementing equation 7.6 which have now been superseded. One of these, the "ε_{max}" method, gives very similar results to the present, recommended method but is less soundly based. Using the "ε_{max}" procedure, the peak interference ε_{max} replaces ε_M. The buoyancy term is determined from model volume and pressure gradient, rather than via the "ρUQ" method.

A velocity vector $v_o(x)$ is accurately measured in the wind tunnel and an uncorrected pressure coefficient C_{p_u}, is determined via

$$C_{p_u} = 1 - \left(\frac{v_o(x)}{U_{\infty_u}}\right)^2 \qquad (7.7)$$

where U_{∞_u} is the nominal mainstream velocity determined from the contraction pressure drop and the empty tunnel calibration. Because of blockage $v_o(x)$ relates to an effective mainstream speed $U_e(x)$, higher than the nominal value and given by

$$U_e(x) = U_{\infty_u} \left(1 + \varepsilon(x)\right) \tag{7.8}$$

Equation (7.8) represents the procedure for pressure correction given by Equation (6.4). The "ε_{max}" procedure is not x-dependent and (7.8) reduces to

$$U_e(x) = U_{\infty_u} \left(1 + \varepsilon_{max}\right) \tag{7.9}$$

The corrected pressure coefficient, C_{p_c}, which associates $v_o(x)$ with the effective mainstream speed, is given by

$$C_{p_c} = 1 - \left(\frac{v_o(x)}{U_e(x)}\right)^2 \tag{7.10}$$

Eliminating $v_o(x)$ between (7.7) and (7.10) gives

$$\left(\frac{U_e(x)}{U_{\infty_u}}\right) = \frac{q_c}{q} = \frac{1 - C_{p_u}}{1 - C_{p_c}} = \frac{k^2}{k_c^2} \tag{7.11}$$

in Maskell's notation.

This equation, which derives from the "ε_{max}" method, is identical to Maskell's equation (17). The "ε_{max}" method therefore exactly parallels Maskell's method but replaces bubble pressure measurements, or alternative assumptions, by results derived from equivalent wall pressure signature measurements.

Wall signatures reflect not only tunnel-induced q-increases but also any change in bubble shape (which we have seen to be small). For cases in which base pressure is not measured, Maskell assumes in effect that the bubble area change is (B/C) times that for a fully yielding wake, where B is

bubble cross sectional area and C is tunnel area. This changes the relationship for determining Maskell's k values but is automatically accommodated by the wall signature procedure. The present method implicitly includes bubble distortion effects while avoiding Maskell's possibly contentious assumptions in this regard.

8.0 CORRECTIONS FOR LIFTING AND POWERED MODELS

8.1 Flat Plates at Angle of Attack

Linear C_L - α Range

Figure 8.1 shows corrected lift curves for four flat plate wings tested to just beyond stall. The semi-span models were mounted from the tunnel floor and the whole-wing aspect ratio was 3. Plate area ranged from 1.6% to 16.7% of test section area and the "ε_{max}" method was used to correct 'q'. Standard text book methods were used for angle of attack corrections. These were generally less than one degree.

Despite the very large model size for wing W4 (circles) and despite the presence of an uncontrolled boundary layer on the tunnel floor, the lift correlation between the four models is excellent over the linear C_L - α range. There was some tendency for smaller models to stall earlier, which was probably due to the relatively greater adverse influence of the floor boundary layer. The lift curve slope is about 10% greater than that given by simple wing theory; this is most likely a manifestation of lift from edge vortices at the wing tip.

Figure 8.2 shows corresponding drag data. In this case the effect of the floor boundary layer was more serious. The percentage effect is smallest for the large wing, W4 and C_{D_i}/C_L^2 for this wing agrees well with the free air value quoted by Hoerner (broken line). The $1/2\pi$ term in Hoerner's equation represents the loss of leading edge thrust for the thin flat plate. The smaller wings exhibit a "cut out" effect in the root region due to the tunnel floor boundary layer. Hoerner states that, with 10% of span removed centrally, the effective aspect ratio is halved (see chained line, Figure 8.2). Even for the smallest wing tested (5.5" semi-span), the effect is significantly less than this.

The above results show that the combined blockage and conventional angle of attack corrections produce good results for large wings, including

one for which C_L S/C was 0.134. In the presence of a floor boundary layer, the largest semi-span model gave the best results.

Post-Stall Range

Figures 8.3 and 8.4 extend the previous lift and drag data all the way to 90-degrees angle of attack, i.e. the normal flat plate case. Uncorrected data are also shown. Drag corrections are particularly large at the higher angles of attack. The correlations between models remain good except in the immediate post-stall region. Here, it appears that the floor boundary layer again had an adverse effect on the smaller models, this time in delaying the approach to the second lift peak.

Figure 8.5 shows the above data in polar form at a larger scale. This reemphasizes the large magnitude of the blockage corrections at high angles of attack. It is also apparent that the "ε_{max}" method overcorrects slightly in this region for the largest wing. On reverting to the "ρUQ" method (tagged circles), improved correlation is obtained up to about 60-degrees angle of attack but thereafter results from the "ρUQ" and "ε_{max}" methods converge. Examination of derived blockage parameters reveals that model-ε, ε_{max} and wake source strength all increase smoothly with angle of attack in this range. However, the peak blockage position moves back up to 60-degrees angle of attack and then stays constant. This evidently is what causes corrections derived by the "ρUQ" and "ε_{max}" methods to converge.

The above comparison between the two correction methods raises an important distinction related to lift. The ε_{max} method, by implication, includes a horizontal buoyancy term in application to drag which appears as the difference between ε_{max} and model ε. This same difference is also applied to lift. This is incorrect because horizontal buoyancy cannot induce lift. This is a further reason for favoring the "ρUQ" method over the "ε_{max}" method.

Figure 8.6 shows pitching moment data over a 0 to 90° angle of attack range. The correlation between the four wings is similar to that for lift and drag. At 90-degrees the quarter chord pitching moment equals 0.25 times the

drag coefficient. Observed differences here reflect both drag coefficient variations, between models, and possible small set-up errors for the smaller models.

8.2 Correlations for the Knee-Blown Flap (KBF) Model

In its basic form, with slats added but no tips, the reference area for the KBF model is 6.2% of the 30" x 43" tunnel cross section, or 37% of the largest flat plate wing. However, the C_L-range is an order of magnitude greater, so $C_L \cdot S/C$ and hence angle of attack corrections are about three times greater than for the flat plate wing. Figure 4.7 of Reference 2 shows that angle of attack and blockage corrections are of comparable magnitude for the KBF model in the 30" x 43" tunnel. The angle of attack corrections used are those of Williams and Butler (Ref. 12) which are applied as described in Reference 2.

Baseline data were obtained in the NASA/AAMRDL wind tunnel (see Reference 2). Since angle of attack corrections are significant, comparisons between corrected small tunnel and large tunnel data are as much a test of the angle of attack corrections as they are of the blockage method. There is a need to carry out both corrections on a consistent, unified basis. This is discussed further in Section 9.

Wall pressure signatures reflect not only model flow conditions but also the effects of changes in tunnel conditions, particularly flow breakdown. This is reviewed in some detail in Section 6 of Reference 2 which discusses signatures for moving ground, blown BLC ground and very high C_μ cases.

Figure 8.7 shows the boundary for jet impingement on the tunnel floor as a function of C_μ and α. A firm correlation has been established between the occurrence of impingement and the subsequent development of a second peak in the wall pressure signature. The broken line in Figure 8.7 is the boundary beyond which the second peak dominates the pressure signature. Once this has happened, the correction process is seriously compromised and model flow conditions are probably unrepresentative of free flight. Figure 8.8 shows the lift characteristics of the KBF model across the entire test range, to C_μ's

of 10 and α's of 30. Individual points are not shown because the curves are the product of cross plots needed to obtain constant C_μ values from corrected data. Up to C_μ = 1, there is generally good agreement between the two tunnels except that unpowered lift is slightly higher in the small tunnel. Corrections are very small in this case.

The C_μ = 2 curve is interesting because it intersects both the impingement and the strong second peak loci in Figure 8.7. The large tunnel and the corrected small tunnel results start to diverge half way between the two conditions. At C_μ's of 4.0 and greater, differences between the small and large tunnel data increase as impingement intensifies.

Figures 8.9 and 8.10 show drag and pitching moment correlations corresponding to a C_L range up to 10. Drag correlations are quite successful, including the unpowered case, but overcorrection again occurs at C_μ = 4, the impingement case. The trends in the pitching moment correlations (Figure 8.10) are generally similar to those for lift.

Reference 2 includes correlations similar to those described here but using what is, in effect, an early version of the present correction method. A "true q" system was employed which relied upon a single pressure measured part way down the test section. Examination of wall pressures measured subsequently has shown that the orifice used in the "true q" system lies between the first and second peaks of this signature under most circumstances, which was a fortunate choice. In effect, the previous system isolated the wake blockage from the total signature and ignored the solid blockage. For this reason the new procedure gives better results up to and including C_μ = 2. Beyond this, the undercorrection tendency of the old, "true q", procedure lead to somewhat better correlations.

Some limited studies have been made of blockage interference associated with the second peak in impingement cases. This peak may be interpreted as due to a second effective body situated at floor level. Because of it's aft location, this body retards the flow in the region of the model. A residual signature was calculated for a C_μ = 8 data set by subtracting the fitted,

single peak signature from the measured one. A rough analysis of this residue gave blockage increments which improved the lift correlation. No corresponding angle of attack correction was attempted. Though such a second-stage analysis provides a likely explanation for small tunnel effects and might be regarded as a basis for further correction, any results obtained might be speculative, at best, because of impingement-induced flow distortion.

9.0 DISCUSSION

With methods for determining axial velocity increments due to blockage now well established, emphasis shifts to determining their effects on a self-consistent basis. A need has also been noted for tunnel surface pressure signature analysis method which determines corrections to angle of attack. To achieve this, a simple horseshoe vortex model might be used, which complements the line source-sink model employed for blockage estimation. The method could be implemented via look-up charts with inputs from tunnel ceiling and floor pressure signatures. Such a procedure would define the angle of attack environment of the model, including variations in at least the axial direction. The problem of determining the effects of the distributed angle of attack increments parallels that concerning distributed blockage velocity increments.

Significant advantages accrue when blockage and angle of attack constraint corrections are determined on the above unified basis. For example, blockage increments found via the present method could be applied to the horseshoe vortex model determined during the angle of attack analysis. This would permit lift and possibly pitching moment increments to be determined using information derived solely from tunnel surface pressures. The present need to estimate a proper effective model position would thereby be avoided.

It is implied in the above discussion that the vortex lifting model would comprise one or maybe two horseshoe systems of unknown strength situated at unknown positions, i.e. a system having non-linear geometric unknowns and linear strength variables as for the present blockage analysis. This approach would probably work well for small models or straight wings but for more complex configurations more elements may be needed to attain the necessary resolution when calculating induced effects. A preferable approach might employ two linear systems, one each for the source and vortex flow models, each of which has multiple elements at known positions but of unknown strength. "One shot" analyses would then be possible using predetermined influence matrices and iterative techniques would be avoided.

The above discussion is of course, quite speculative and any attempt to implement the suggested scheme should probably be made on a careful, stage-by-stage basis. However, much of the data described in the present report could be used for checkout purposes.

10.0 CONCLUDING REMARKS

The present report concerns a wind tunnel blockage correction method, first described in Reference 1, which relies upon wall pressure measurements. This ensures that changes in blockage, due to stall or power effects for example, are sensed immediately and are incorporated automatically into the correction process. Correlations from tests on various models are given in this report including normal flat plates, spheres, an idealized automobile, flat plate wings and a blown-flap model. Tests upon scaled models in a single tunnel or upon one model in small and large tunnels are included in all cases.

The terms of reference for the above studies relate predominantly to the prediction of blockage-induced velocities within the test section volume. Secondary objectives concern the conversion of such velocity increments to model surface pressure or force corrections.

Determination of Interference Velocities (Section 4)

The development of wall pressure analysis techniques and blockage velocity prediction methods is complete. Velocity increments due to combined wake and solid blockage have been computed throughout the test section volume, and it has been found that knowledge of the centerline axial velocity increment is sufficient for most purposes. Certain "problem" signatures — notably those with double peaks due to tunnel flow breakdown — are accepted and analyzed by the current program. However the validity of the test itself should be questioned when such signatures occur.

Corrections to Measured Pressures (Section 6)

A correction technique has been devised for model surface pressures which relies upon a "local mainstream" concept (see equation 6.4). The method has been checked out successfully against definitive theoretical predictions, in tunnel-versus-free-air sphere surface pressure comparisons, and in automobile tests. It is suggested that a similar concept may also apply to skin friction.

Corrections to Drag (Section 7)

Drag correction techniques have been reviewed in some detail. An early technique, designated in Reference 1 as the "ε_{max}" method, is closely related to Maskell's blockage correction method for bluff bodies and stalled wings. More recently, the "ρUQ" method has been developed which involves separate buoyancy and dynamic pressure corrections (see equation 7.6). Buoyancy corrections are derived from the drag of the wake sink found during signature analysis — hence the name "ρUQ method". The dynamic pressure correction is determined at the model center. The two methods produce comparable results and work well for non-lifting models. However, it is shown that the ρUQ method is better founded and therefore should be more readily applicable to complete, lifting models.

Corrections for Lifting Models (Section 3.1)

The above methods extend to lifting cases quite readily provided that lift is concentrated around a single x-location. The power of the "ρUQ" method becomes evident in this application since dynamic pressure corrections may be determined at a wing quarter chord, for example, or possibly at the half-chord under stalled conditions. Tests on a family of AR 3 flat plate wings up to and including 90-degrees angle of attack showed excellent correlations for wing:tunnel area ratios of up to 10%. There were up to 5% drag discrepancies above 60-degrees for a wing with S/C of .167 but the corrections were extremely large — the uncorrected drag coefficient being twice the corrected value with the wing normal to the flow. An effective model location at 50% chord was assumed throughout these studies and conventional angle of attack corrections were employed.

Corrections for Powered Models (Section 3.2)

Powered tests were corrected successfully by the present method up to approximately $C_L = 10$, $C_\mu = 4$, despite the fact that mild tunnel flow breakdown was present for all $C_\mu = 4$ data. The occurrence of flow breakdown was readily detected from the wall pressure signatures which developed a second

peak under these conditions. This caused increasing overcorrection, by the present method, as C_μ increased beyond 4.

Model Size Considerations

In the past, model size in relation to the tunnel cross section has sometimes been limited by our ability to perform blockage corrections with confidence. Development of the wall signature method has removed much of this difficulty and much larger models may be considered. An extreme example is described in Section 7 concerning a 15-inch diameter sphere in a 30" x 43" test section. Both surface pressures and drag values were corrected successfully.

Axial gradient of blockage velocity may be a limiting factor for more complex models, particularly if lift is present. If lift is not concentrated around a single x-location — as on a large-chord wing, a highly swept wing or a whole aircraft model with a tail — accurate moment corrections may not be possible unless pressure distributions or component forces are available. Thus blockage gradient, rather than blockage magnitude, may limit model size in certain cases. Because of properties inherent to the present method, gradient presents less difficulty regarding axial force corrections than for transverse forces or moments. A unified correction method is proposed, in Section 9, which extends the present wall pressure signature analysis method by adding vortex elements to the source-sink theoretical model, thereby placing angle of attack corrections on a similar footing to the present blockage correction.

11.0 REFERENCES

1. Hackett, J. E.; and Wilsden, D. J.: Determination of Low Speed Wake-Blockage Corrections via Tunnel-Wall Static Pressure Measurments. Presented at AGARD Wind Tunnel Design and Testing Techniques Conference, October 1975 in London, England. AGARD CP 174, Paper 23, October 1975.

2. Hackett, J. E.; and Boles, R. A.: Ground Simulation and Tunnel Blockage for a Swept, Jet-Flapped Wing Tested to Very High Lift Coefficients. NASA CR-152032, June 1977.

3. Hackett, J. E.; and Wilsden, D. J.: Estimation of Tunnel Blockage from Wall Pressure Signatures: A Review of Recent Work at Lockheed-Georgia. AIAA Paper No. 78-828 given at the AIAA 10th Aerodynamic Testing Conference, San Diego, California, April 1978.

4. Hackett, J. E.; Boles, R. A.; and Praytor, E. B.: Ground Effect for V/STOL Aircraft Configurations and Its Simulation in the Wind Tunnel, Part II - Experimental Studies. NASA CR 114,496, November 1972.

5. Hackett, J. E.; Boles, R. A.; and Lilley, D. E.: Ground Simulation and Tunnel Blockage for a Jet-Flapped, Basic STOL Model Tested to Very High Lift Coefficients. NASA CR 137,857, March 1976.

6. Wilsden, D. J.: A Review of Blockage Correction Methods for Automobile Testing in Wind Tunnels. Lockheed-Georgia Engineering Report No. LG79ER0050, March 1979.

7. Pope A.; and Harper, J. J.: *Low Speed Wind Tunnel Testing*. Published by John Wiley and Sons, 1966.

8. Thom, A.: Blockage Corrections in Closed High Speed Tunnels. ARC R&M 2033, November 1943.

9. Hensel, R. W.: Rectangular wind Tunnel Blocking Corrections Using the Velocity Ratio Method. NACA TN 2372, June 1951.

10. Maskell, E. C.: A Theory of the Blockage Effects on Bluff Bodies and Stalled Wings in a Closed Wind Tunnel. ARC R&M No. 3400, November 1963.

11. Maxworthy, T.: Experiments on the Flow Around a Sphere at High Reynolds Numbers. Transactions of ASME, Paper No. 69-APMW-26.

12. Williams, J.; and Butler, S. F.: Experimental Methods for Testing High Lift BLC and Circulation Control Models. In *Boundary Layer and Flow Control* by Lackman (ed), Vol. I, Pergamon Press, 1961, p. 395.

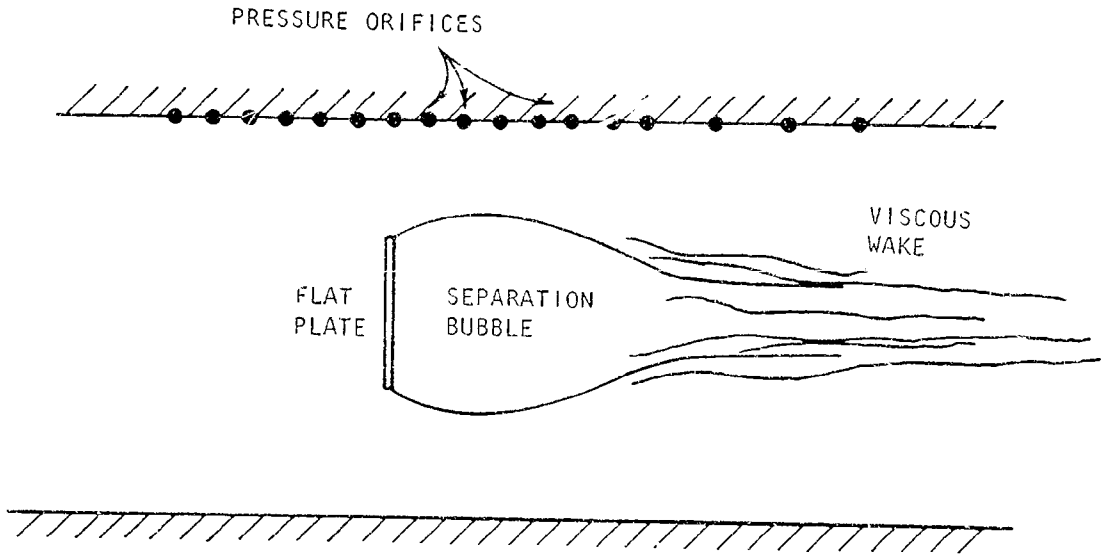

Figure 2.1 Determination of wall pressure signature in a typical case.

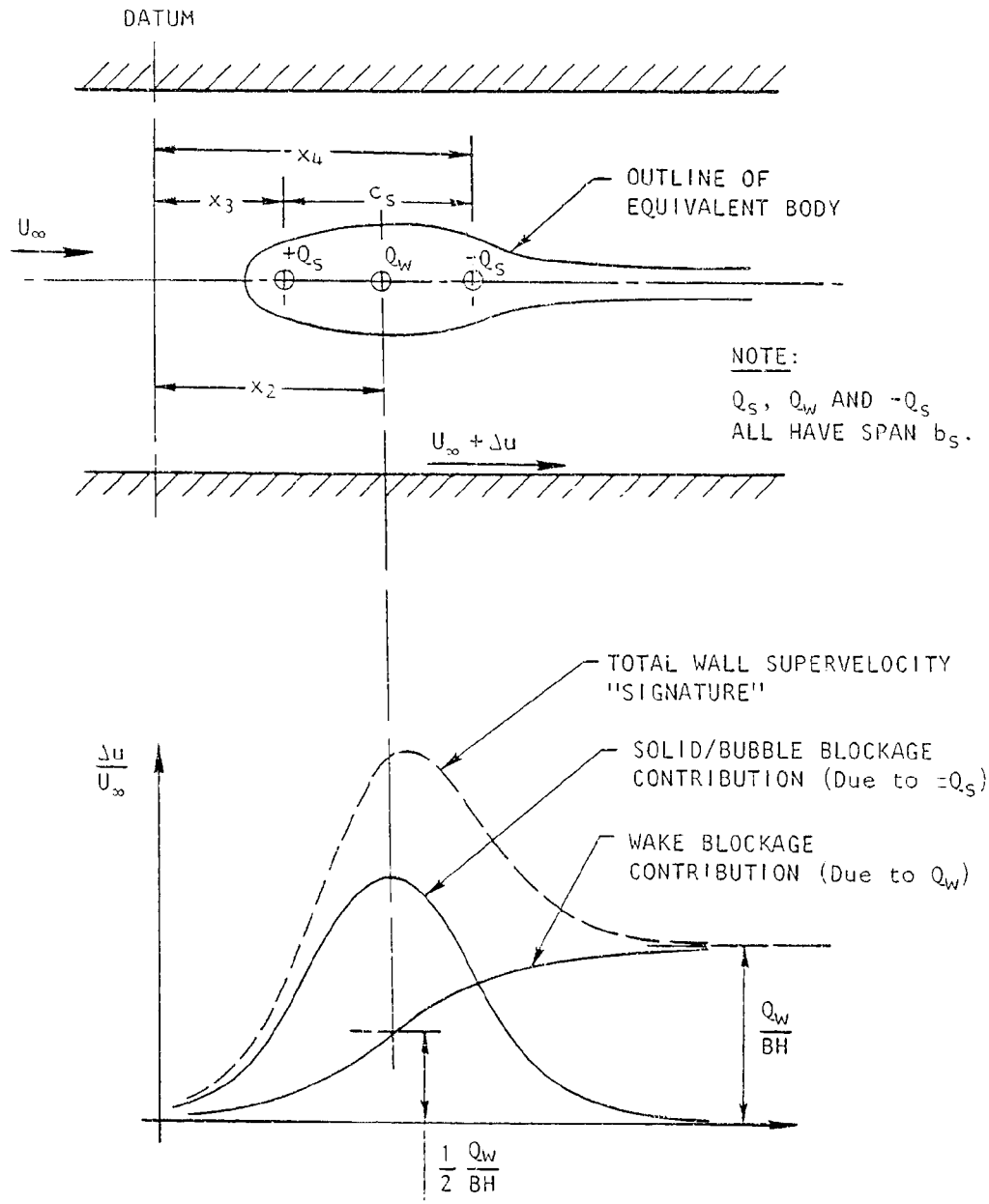

Figure 2.2 Effects, at a wind tunnel wall, of solid/bubble and of viscous wake blockage.

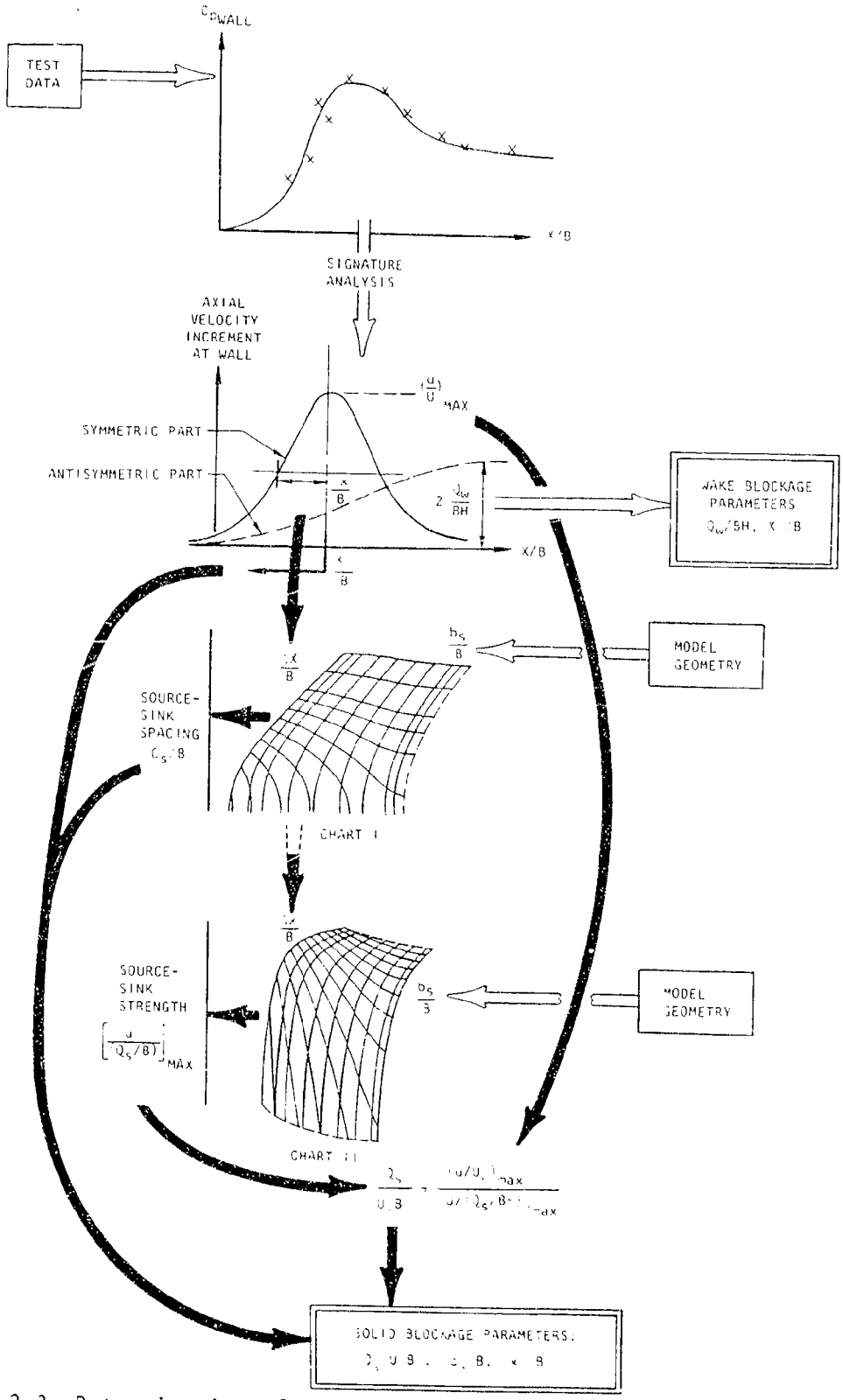

Figure 2.3 Determination of solid/bubble and wake-biockage parameters from a wall pressure signature.

ALTERNATIVE SETS OF ROOTS:

SET #	$\frac{Q_s}{U_\infty}$	$\frac{Q_w}{U_\infty}$	$\frac{x_2}{B}$	$\frac{x_3}{B}$	$\frac{x_4}{B}$	$\frac{b_s}{B}$	$\frac{b_{3,4}}{B}$	COMMENTS
1	96	42	.11	-.21	.44	.05	.05	Chart Method, $b_s = .05B$
2	93	42	.11	-.25	.46	.30	.30	Chart Method, $b_s = .30B$
3	113	42	.03	-.12	.38	.30	.35	Nonlinear Solver. Problem reduced to one of 6 variables by fixing b_s.
4	121	42	.29	-.18	.43	.30	.45	
5	121	44	.59	-.18	.51	.30	.45	

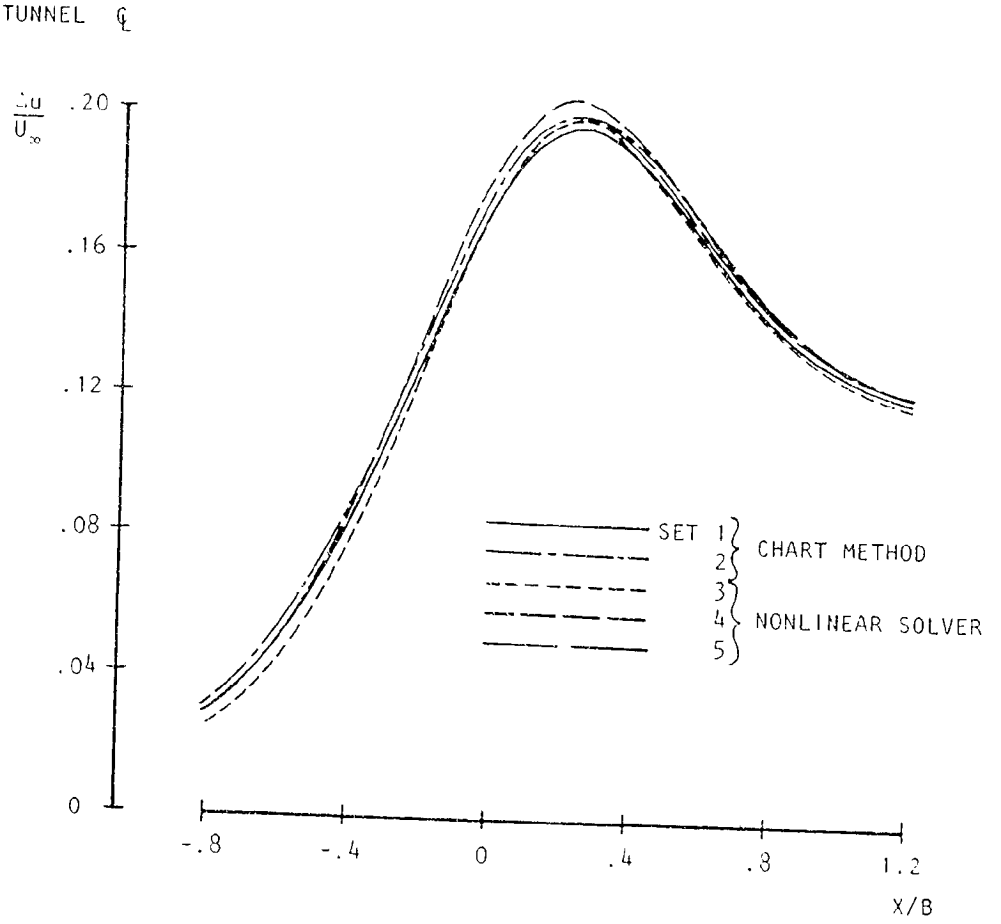

Figure 2.4 The nature and consequences of multiple solutions to the wall pressure inverse problem (normal plate S/C = 9.5%)

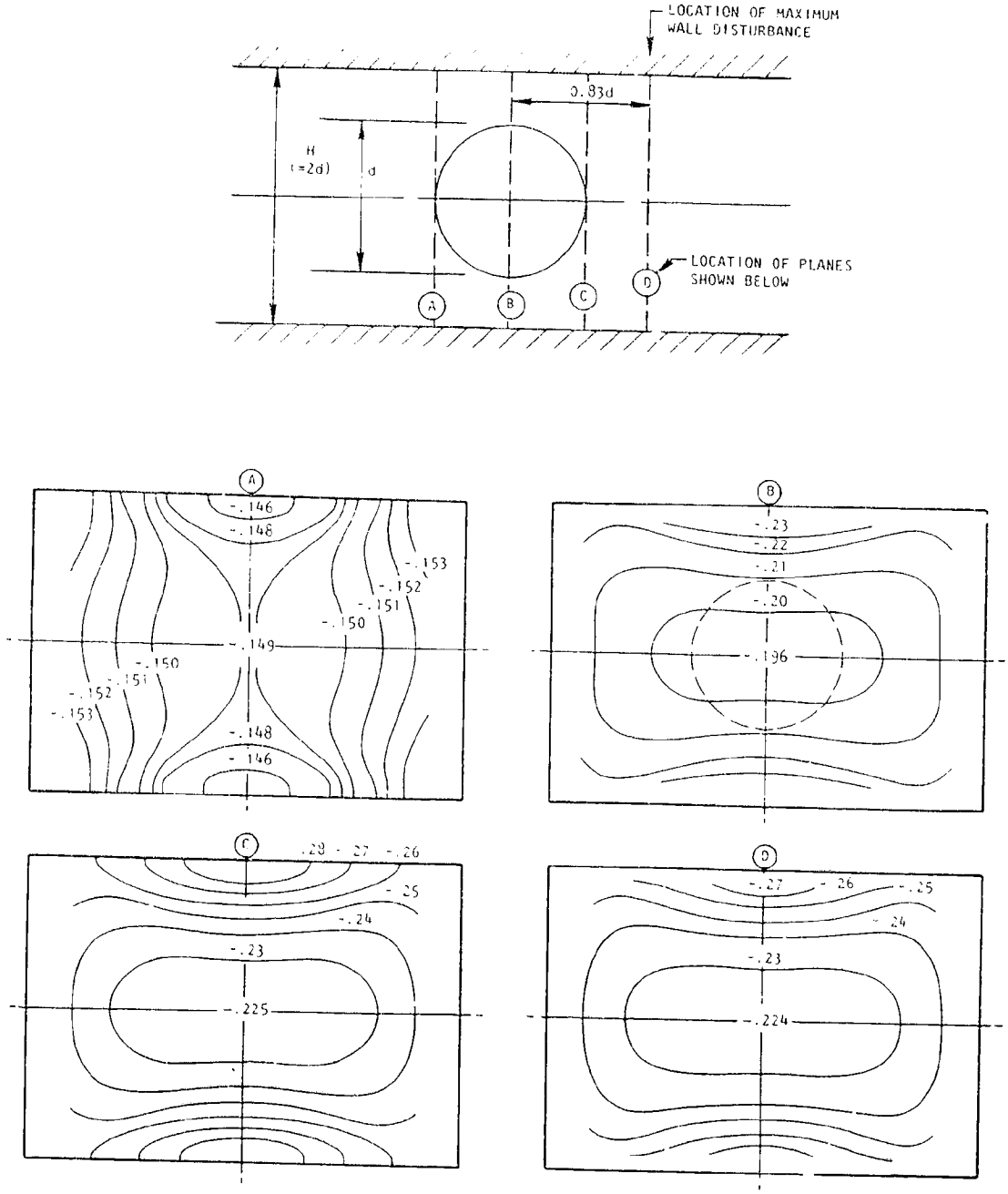

Figure 2.5 Distribution of blockage-induced pressure coefficients, across the tunnel cross-section, for a large subcritical sphere (S/C = 13.7%).

	AREA RATIO METHOD (REF. 7)	THOM (REF. 8)	HENSEL (REF. 9)	MASKELL (REF. 10)	HACKETT-WILSDEN
SUB-COMPACT† S/C = 4.8%	-2.4%	-6.9%	-6.3%	--	-7.3%
IDEALIZED SEDAN† S/C = 5.65%	-2.8%	-7.4%	-7.2%	-9.6%	-8.9%
VAN† S/C = 10.16%	-5.1%	-22.1%	-20.3%	--	-22.9%
SUBCRITICAL SPHERE S/C = 13.7%	-7.0%	-13.4%	-17.9%	-27 → -32%	-29.3%

†*From Ref. 6.*

Figure 2.6 Blockage corrections to drag coefficient by various methods.

DATE	TUNNEL + TEST #	IRAD PROJECT OR CONTRACT #	CONFIGURATION	DIMENSIONS	COMMENTS
SEPT 74 AND DEC 74	LOCKHEED 16½' × 23½' TESTS 140, 145	74R490	NORMAL FLAT PLATES	SEE FIGURE 3.2	STING MOUNTED SEE FIGURE 3.2 AND REF. 1
MAR 78	LOCKHEED 30" × 43" TEST 036	78R490	FLAT PLATE WINGS	SEE FIGURE 3.3	FLOOR-MOUNTED HALF WINGS. TEST RANGE α = 0° TO 90°
JULY 77 SEPT 77	LOCKHEED 30" × 43" TEST 030 LOCKHEED 16½' × 23½' TEST 238	77R490	SPHERES	12" AND 14" DIA. 8.5", 12" AND 15" DIA.	SEE FIGURE 3.4 AND REF. 3
MARCH 75 JAN 76	LOCKHEED 30" × 43" TEST 015 NASA/AAMRDL 7' × 10' TEST 195-I	CONTRACTS NAS2-8745 AND NAS2-9155	KNEE-BLOWN FLAP MODEL	20" POWERED SPAN 30" WITH TIPS NO SWEEP δF_{UPPER} = 76°	SEE FIGURE 3.5 AND REF. 2

Figure 3.1 Summary of biockage tests.

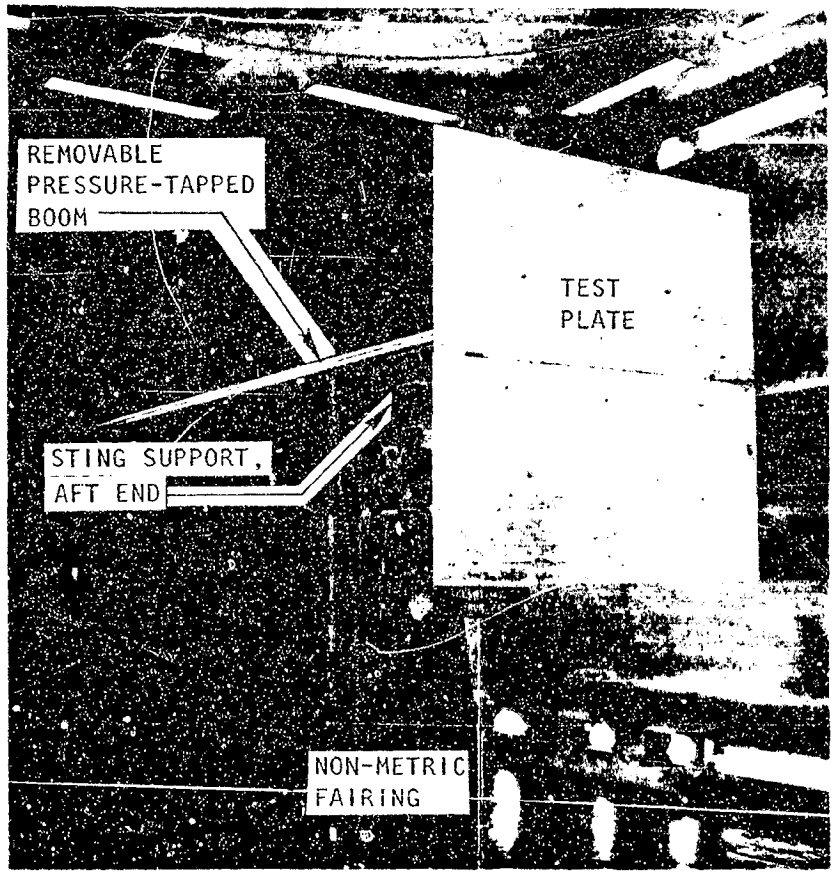

Figure 3.2 Details of normal plates tested in the Lockheed $16\frac{1}{4}' \times 23\frac{1}{4}'$ tunnel.

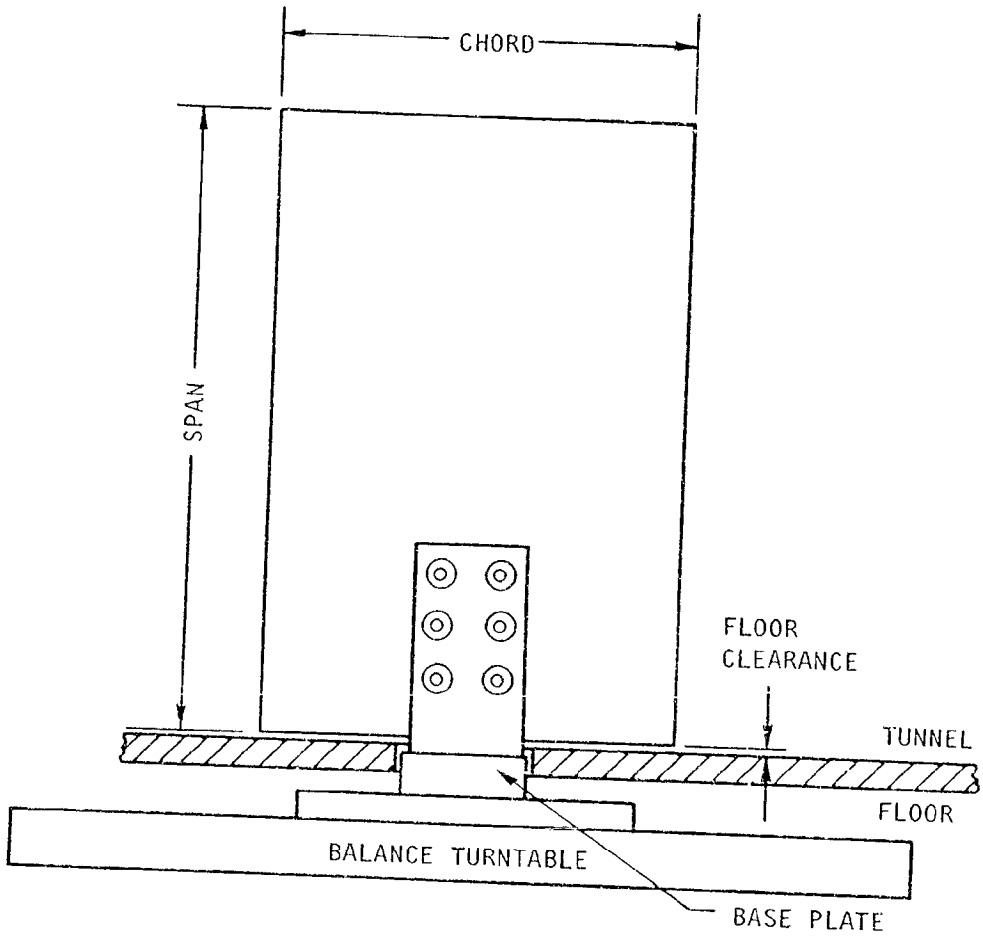

WING	CHORD IN.	SPAN IN.	THICKNESS IN.	BASE PLATE DIA. IN.	FLOOR GAP IN.	$R_N \times 10^{-6}$	S/C
W_1	3.67	5.50	0.093	1.125	0.050	0.720	1.56%
W_2	7.33	11.00	0.125	2.000	0.100	0.720	6.25%
W_3	9.18	13.75	0.141	3.000	0.125	0.720	9.78%
W_4	12.00	18.00	0.172	3.000	0.150	0.720	16.74%

Figure 3.3 Details of flat plate wings tested in the Lockheed 30" x 43" tunnel.

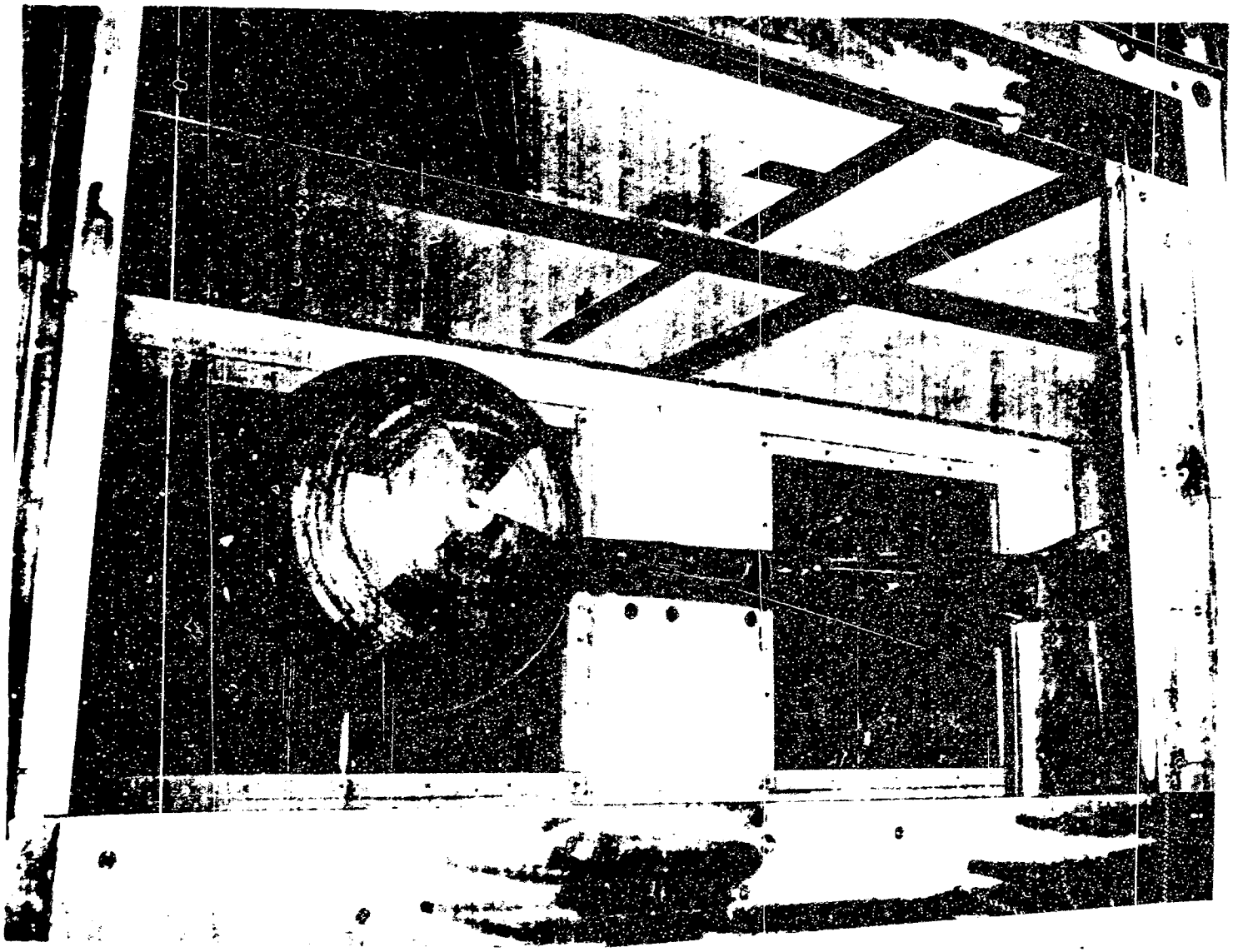

Figure 3.4 Fifteen-inch sphere in the Lockheed 30" × 43" tunnel (S/C = 13.7%).

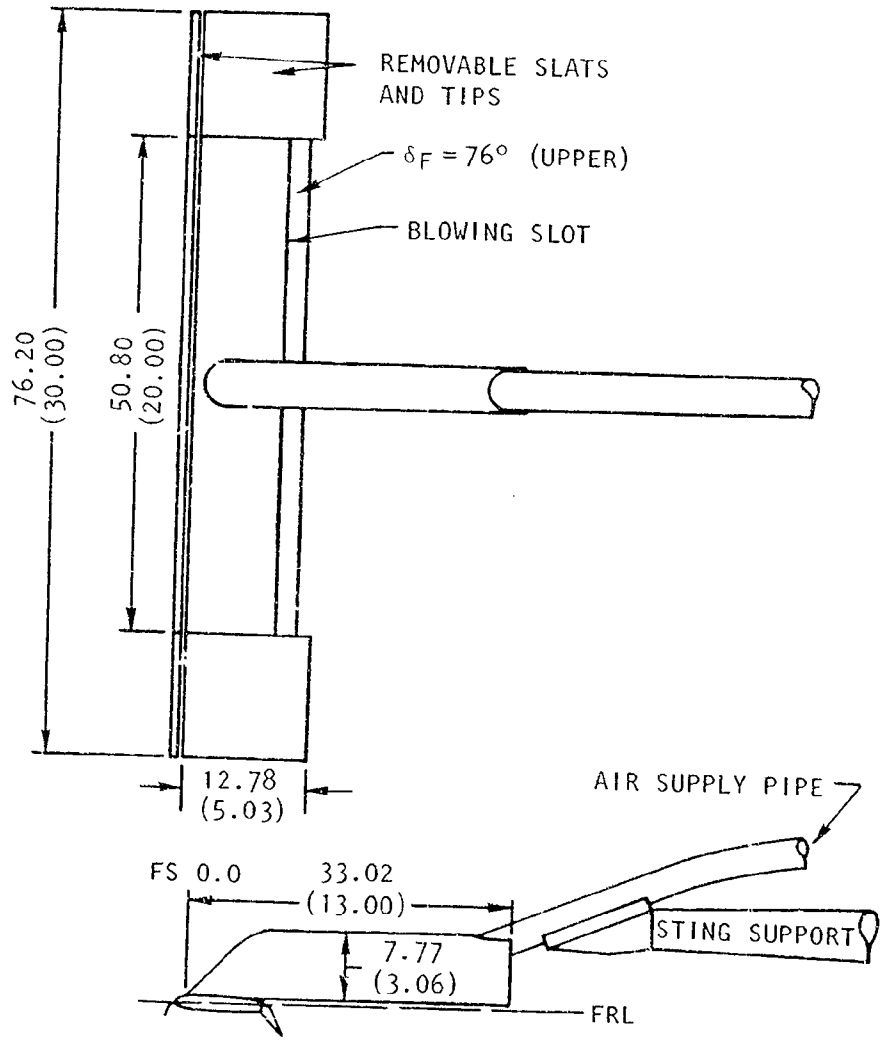

DIMENSIONS SHOWN IN INCHES (CM)

Figure 3.5 Dimensional details of KBF model.

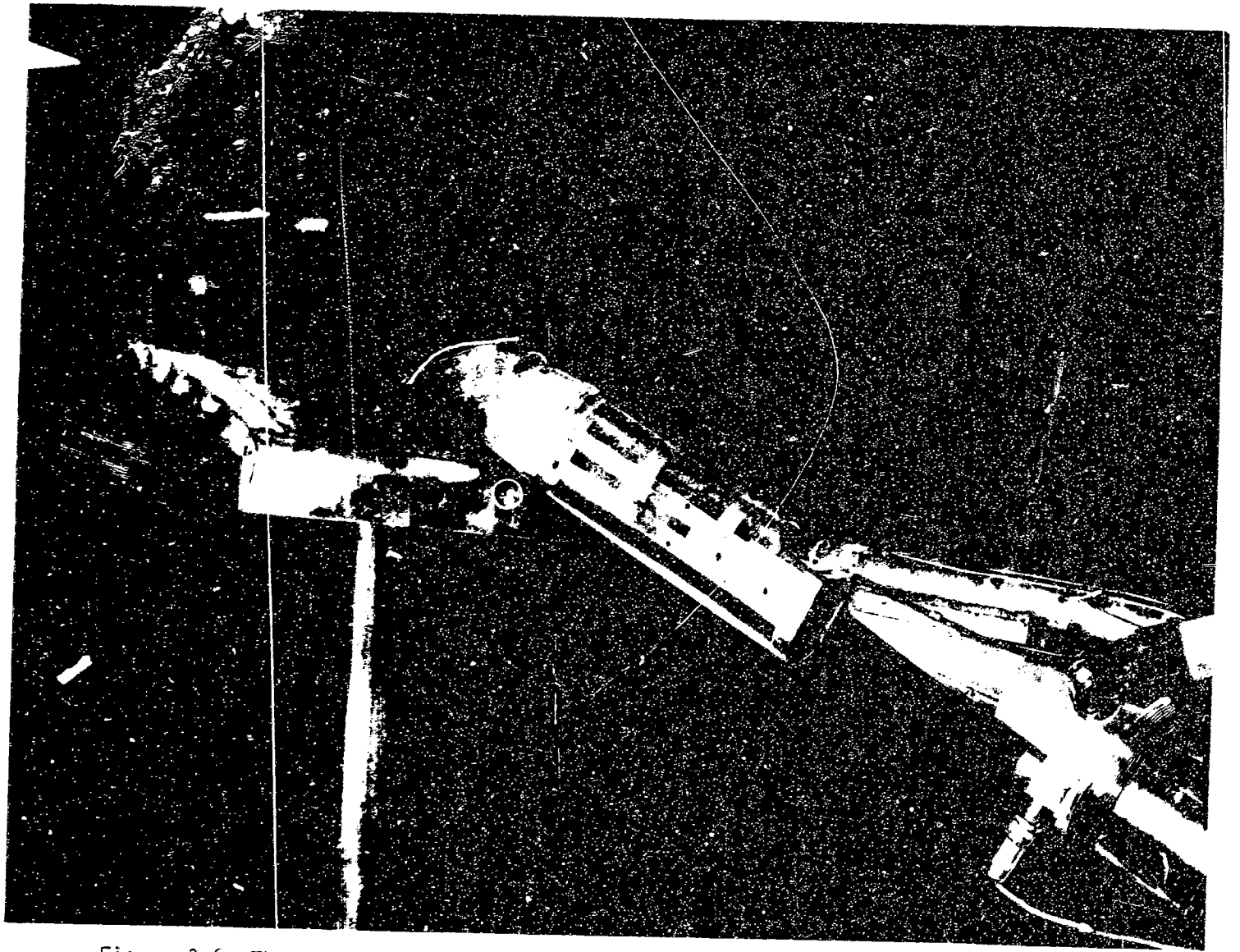

Figure 3.6 The unswept knee-blown flap model in the NASA/AAMRDL 7' x 10' tunnel.

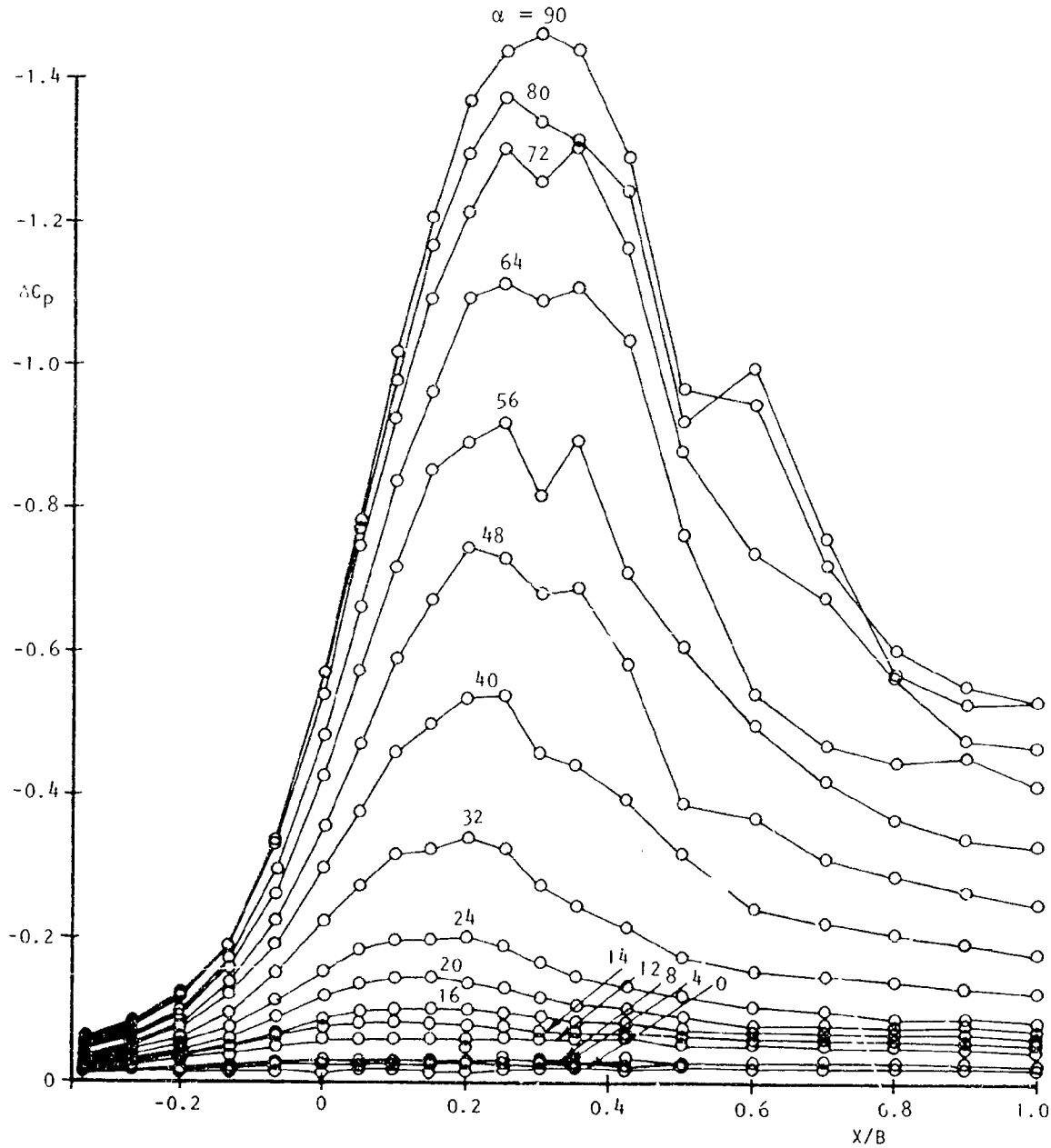

Figure 4.1 Ceiling pressure signatures for a floor-mounted semispan wing (Fig. 3.3) at $0° \leq \alpha \leq 90°$ (S/C = 16.7%).

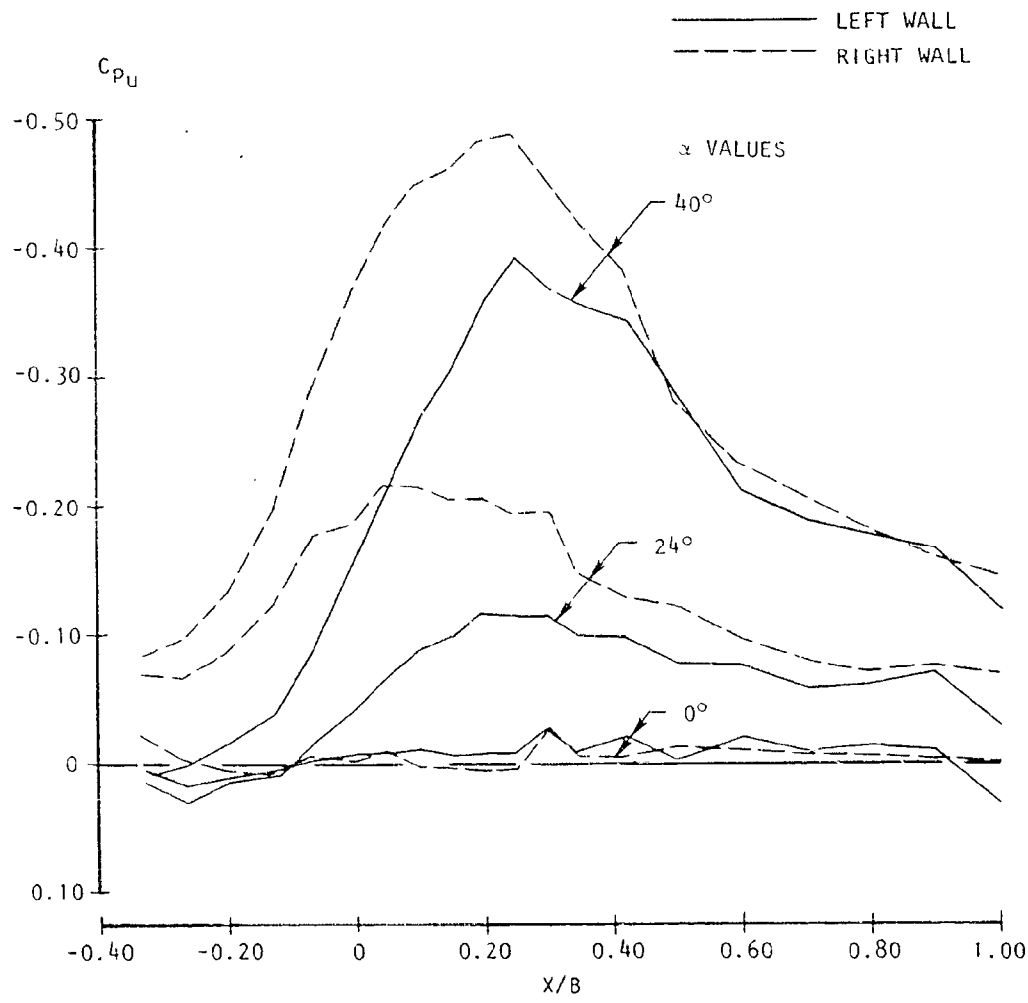

Figure 4.2 Wall Pressures at mid-height for a floor-mounted semispan wing (S/C = 16.7%).

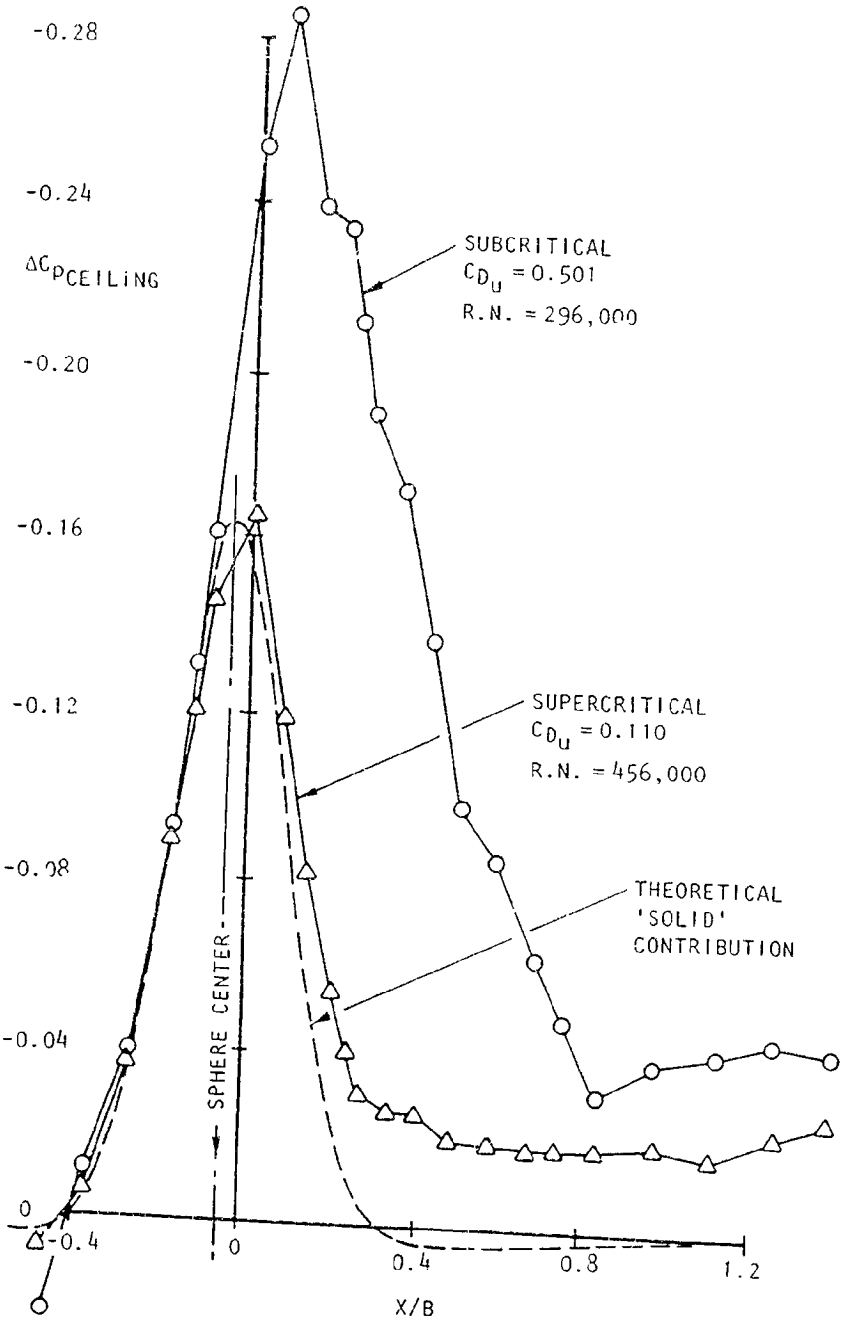

Figure 4.3 Measured Ceiling Pressure Distributions for Sub- and Supercritical Sphere Reynolds Numbers (S/C = 13.7%).

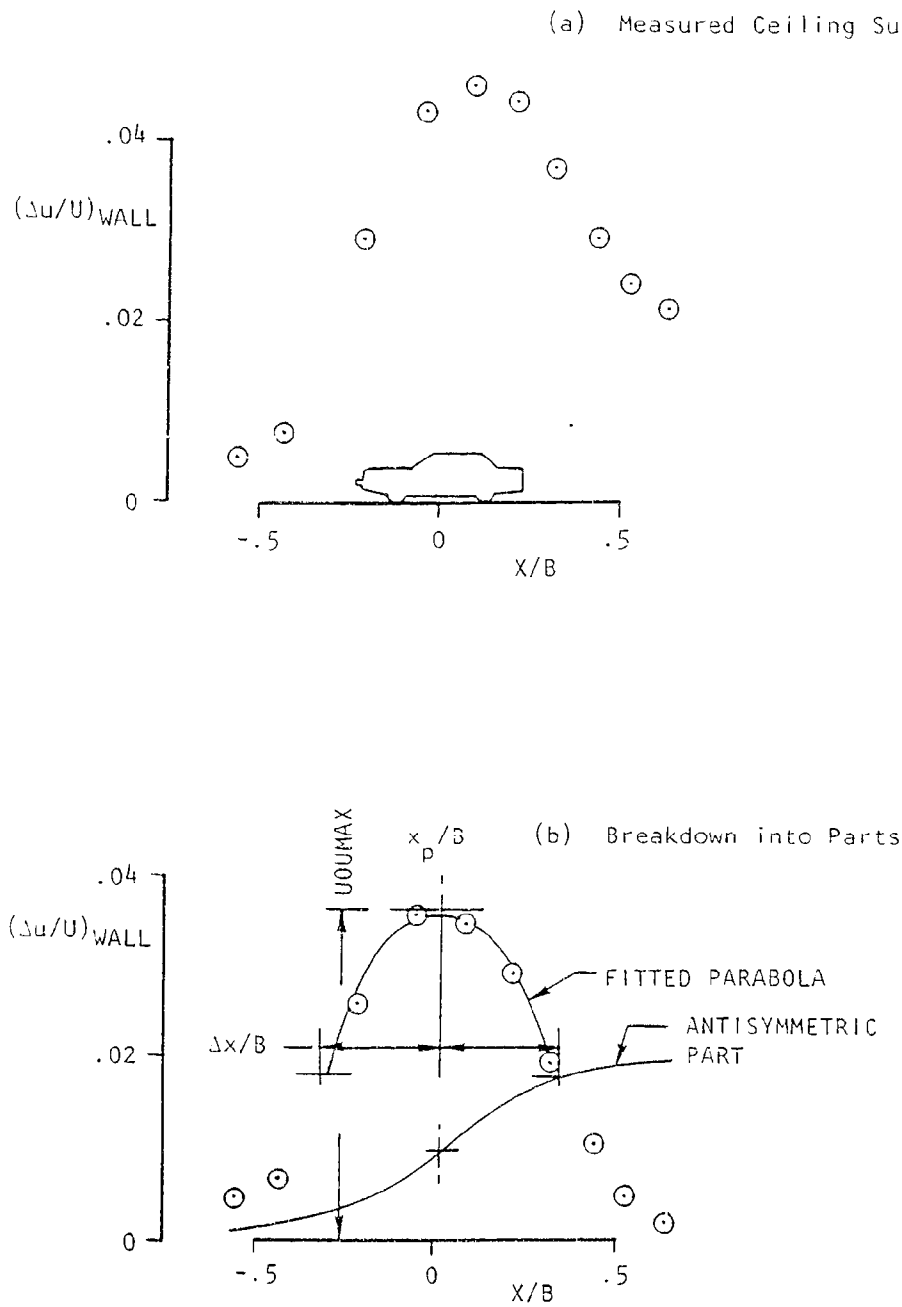

Figure 4.4 Resolution of measured supervelocities into symmetric and antisymmetric parts.

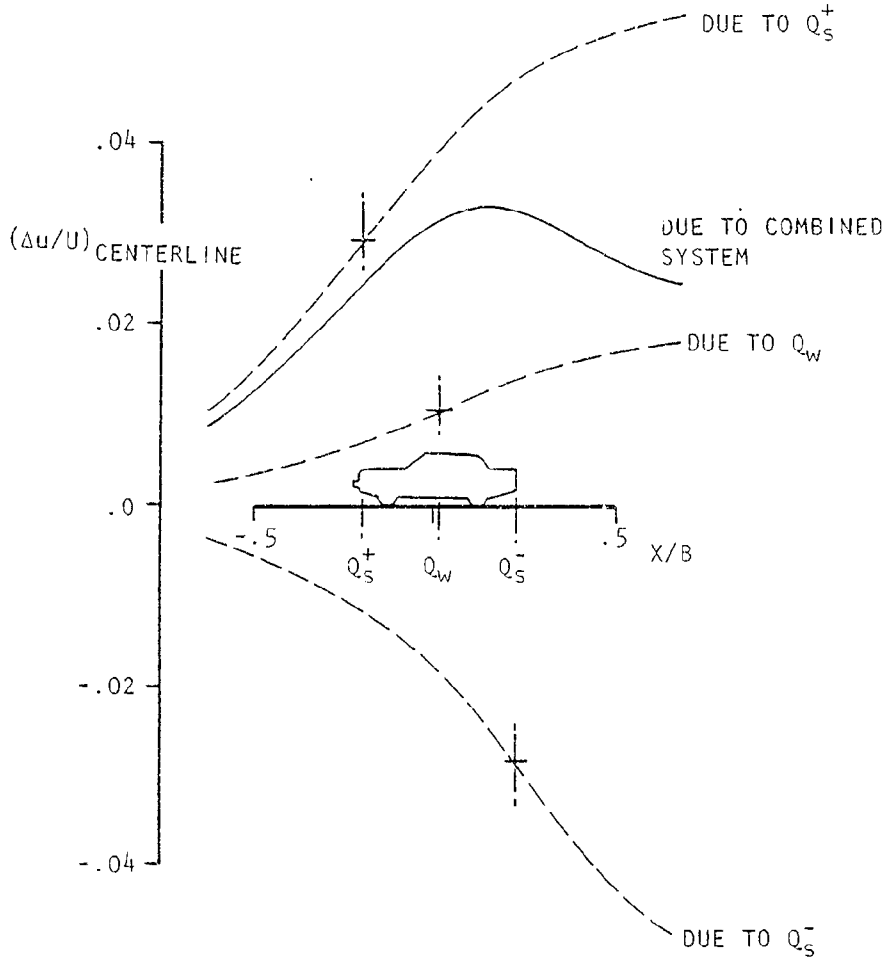

Figure 4.5 Buildup of tunnel centerline interference velocity from individual source and sink contributions.

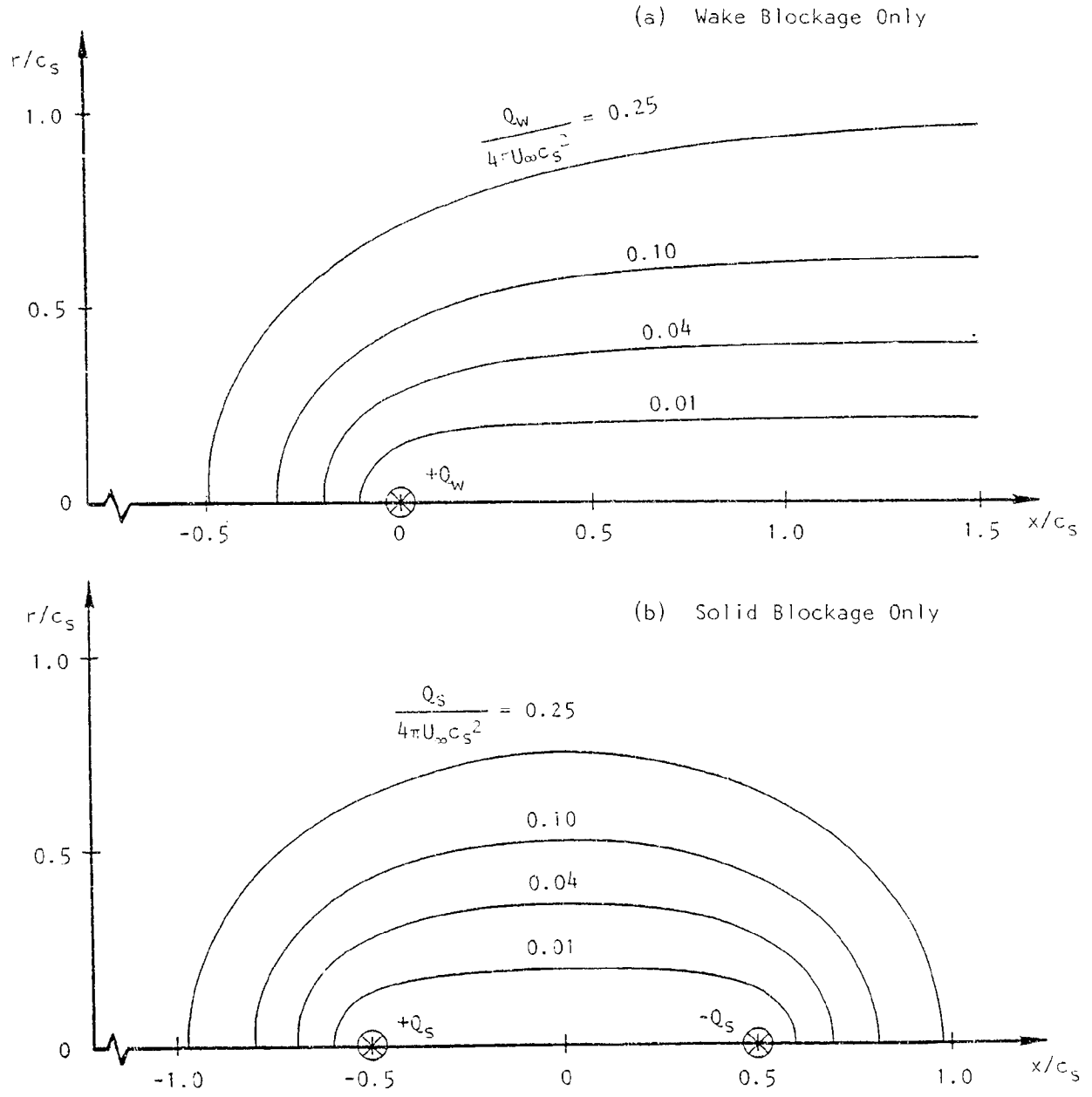

Fig. 5.1 Equivalent body shapes for limiting cases.

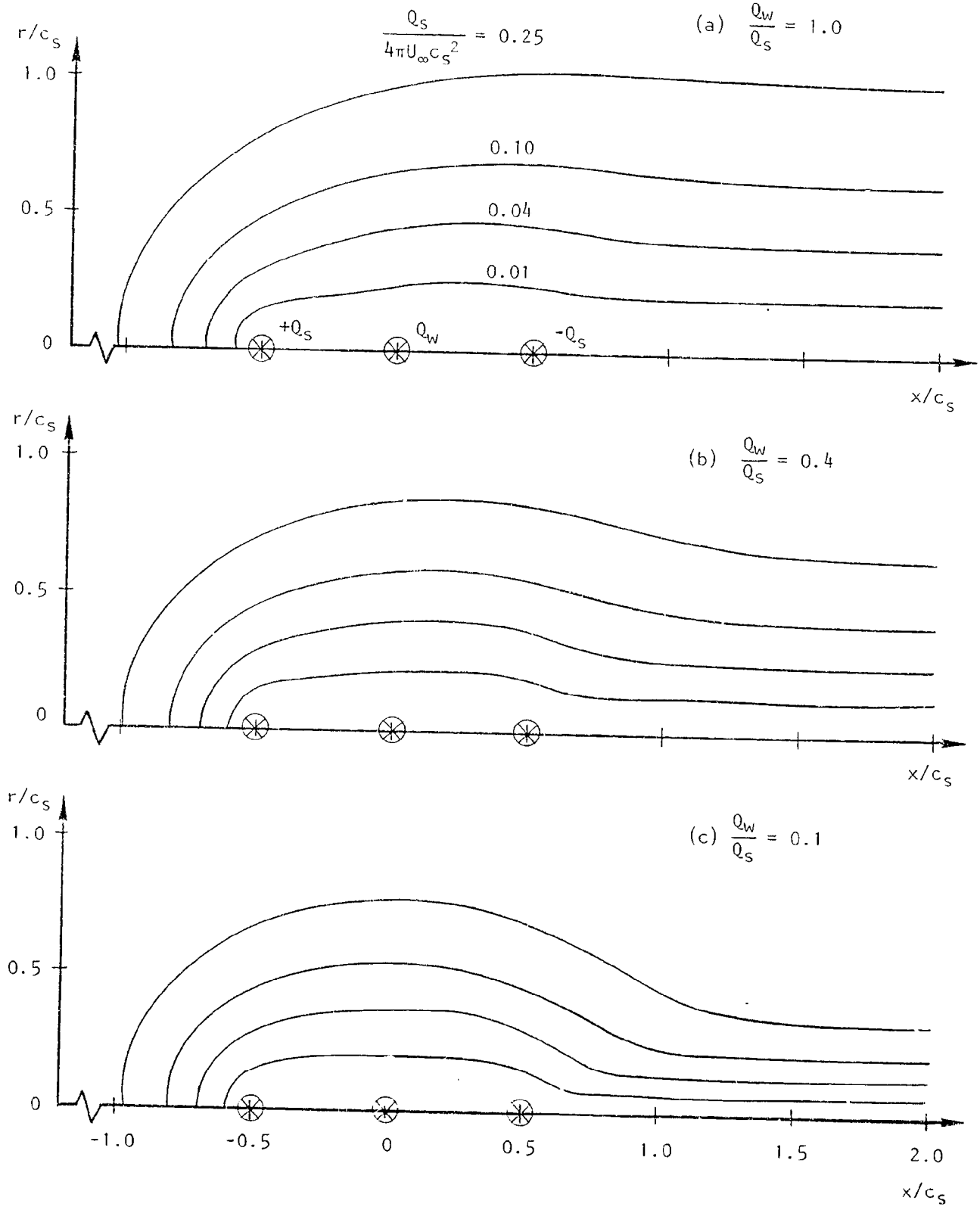

Figure 5.2 Equivalent body shapes for combined wake and solid blockage.

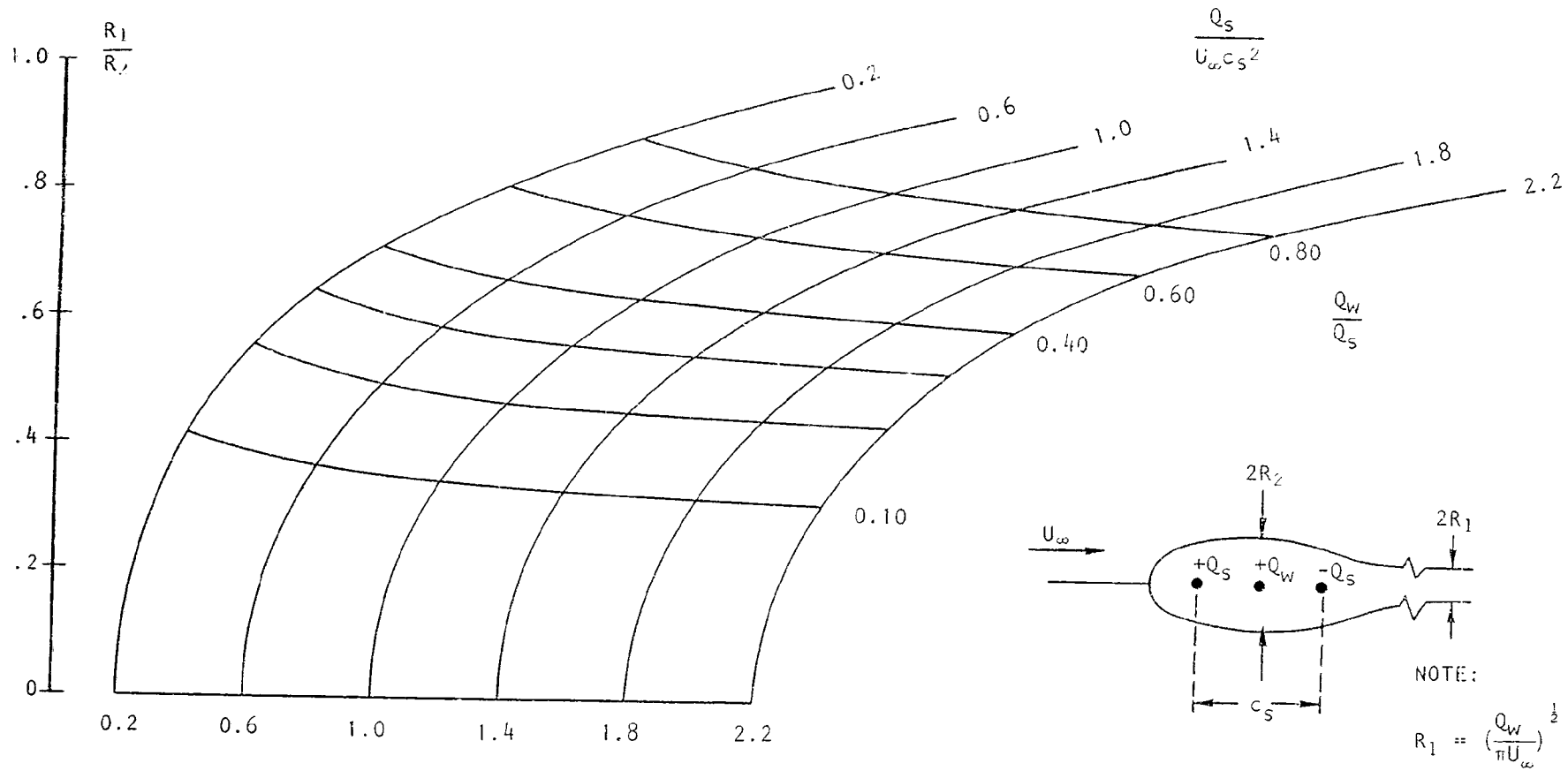

Figure 5.3 Determination of maximum radius of effective bodies.

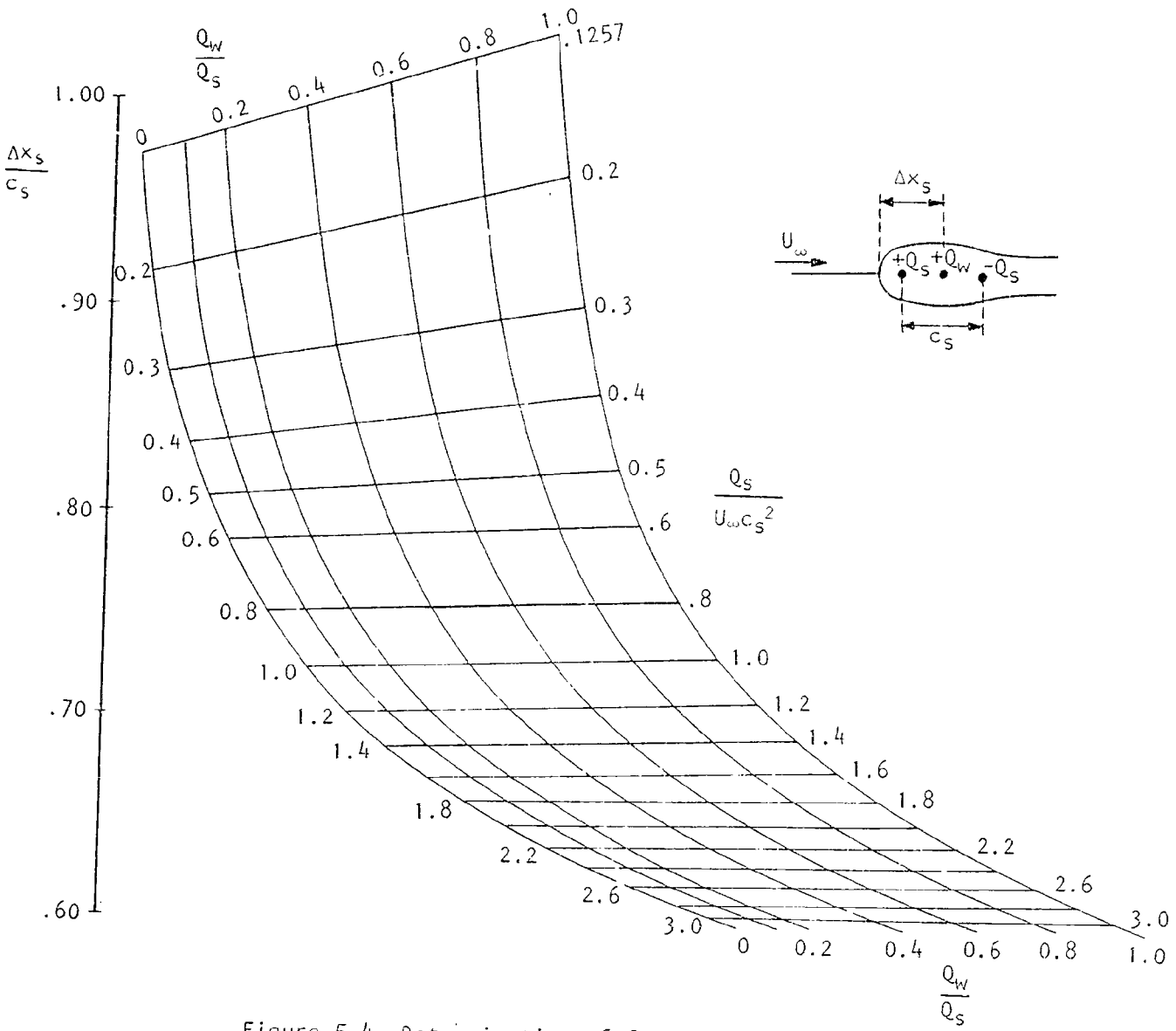

Figure 5.4 Determination of front stagnation point position for effective bodies.

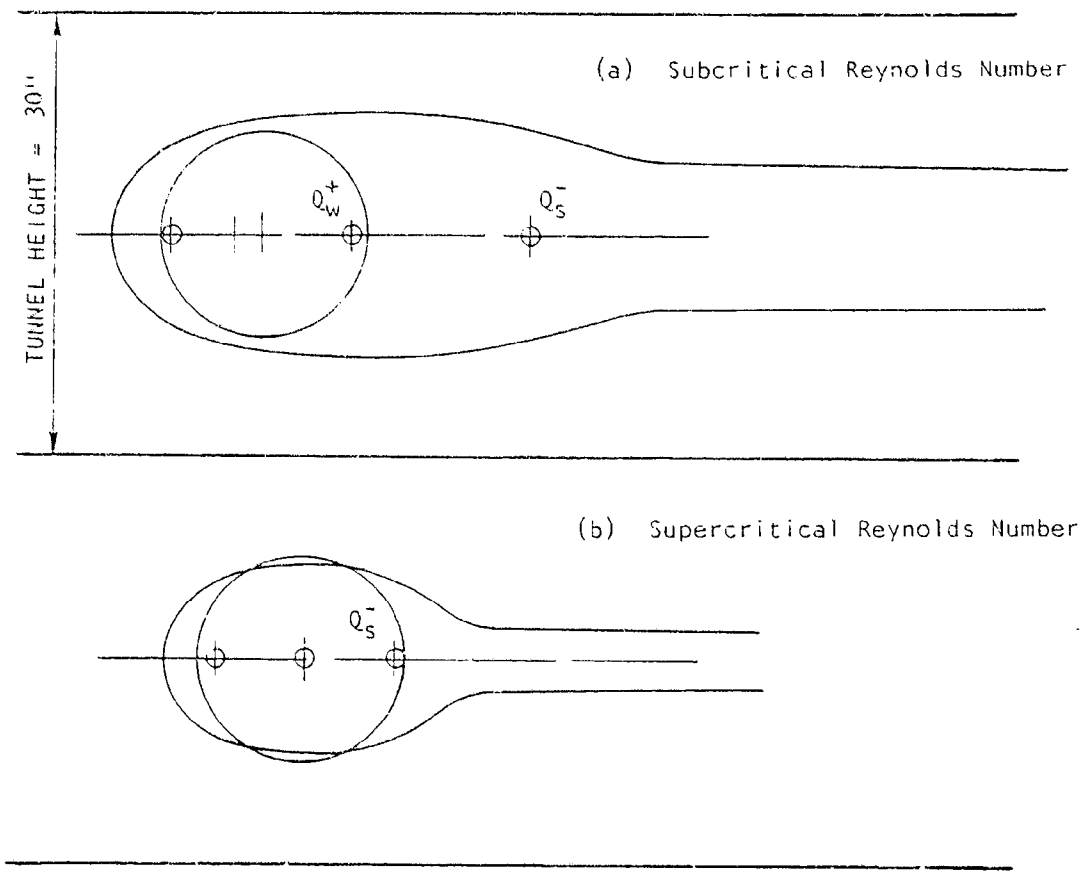

Figure 5.5 Effective body shapes for a 15-inch diameter sphere.

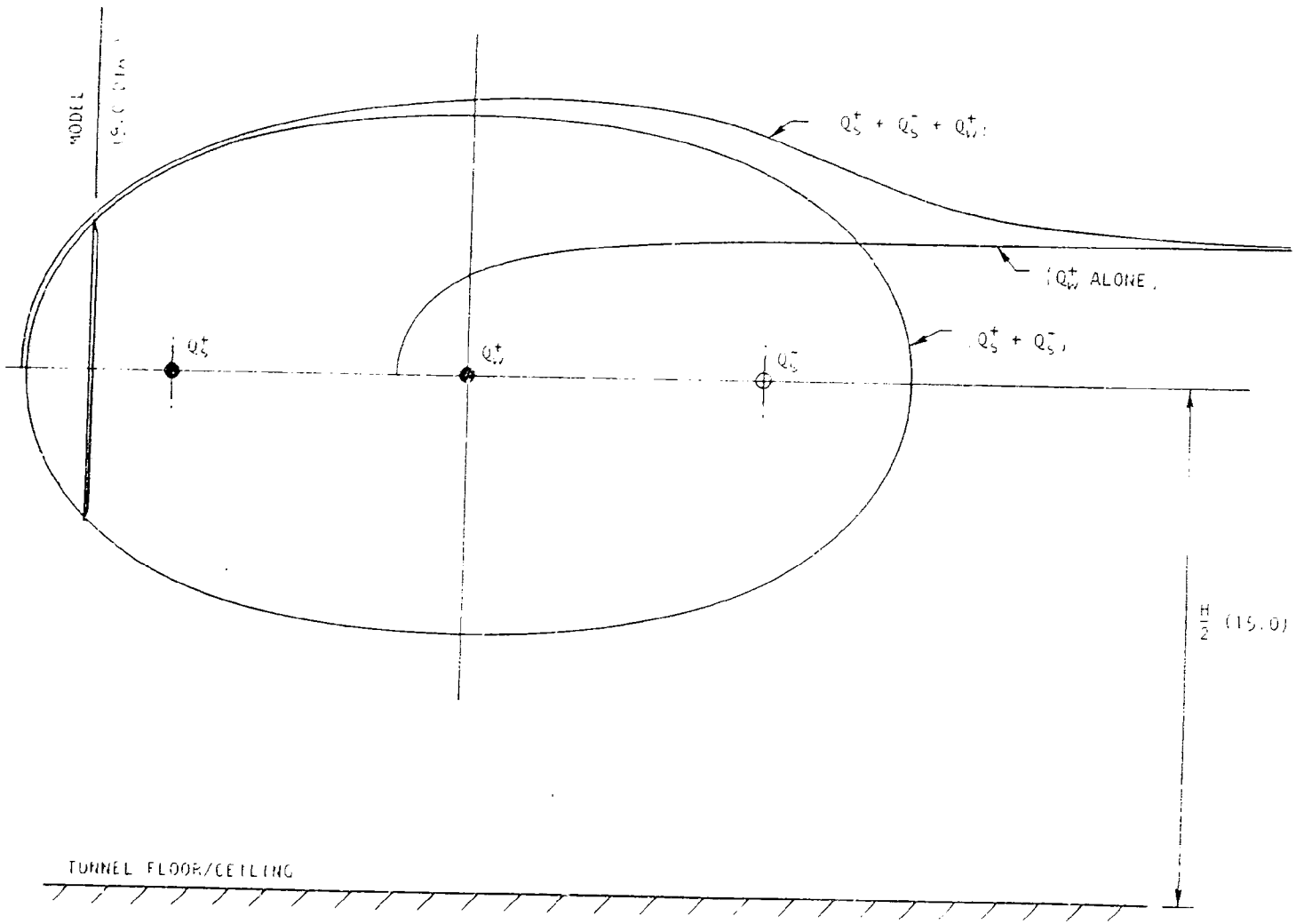

Figure 5.6 Effective body shape for flat disc (30" × 43" tunnel, S/C = 4.9%)

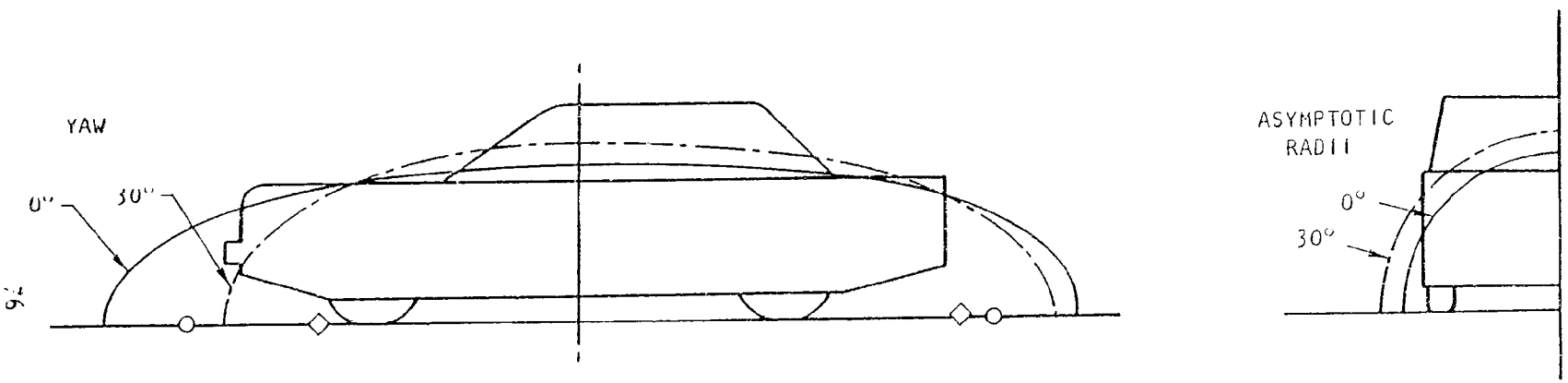

Figure 5.7. Calculated shapes for an idealized car model.

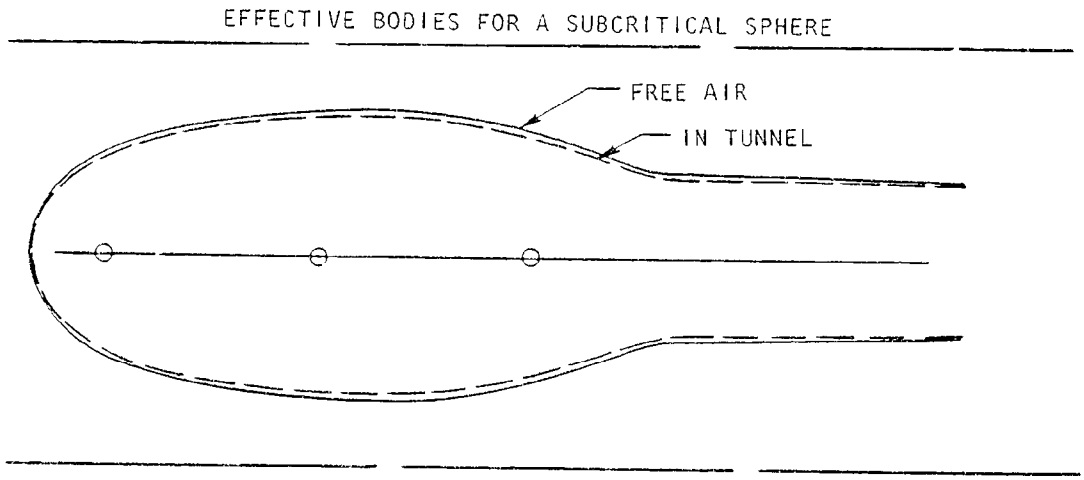

Figure 5.8 Distortion of effective model shape by tunnel-induced velocities.

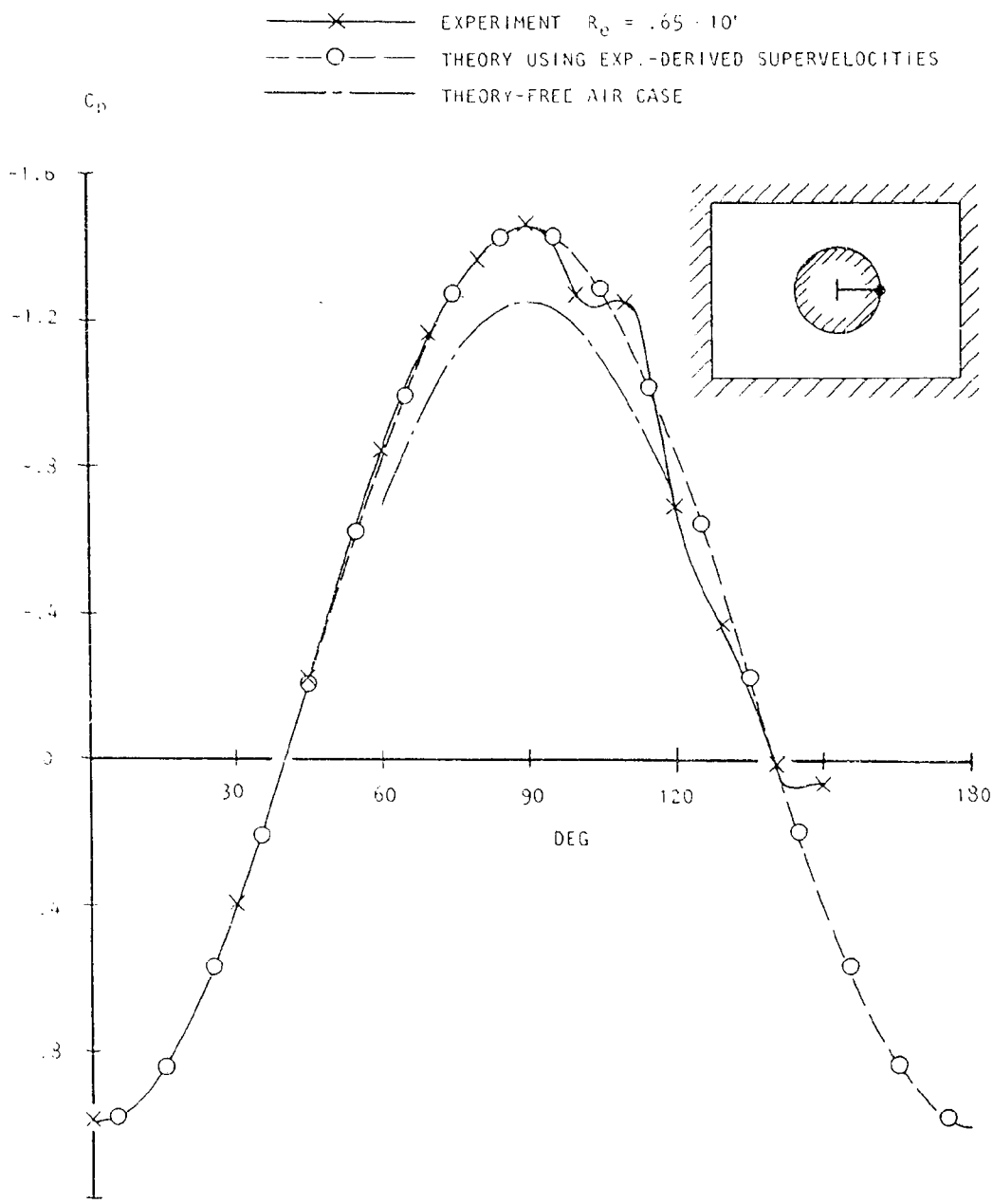

Figure 6.1 Prediction of tunnel-induced pressures for a supercritical sphere via a source-panel method.

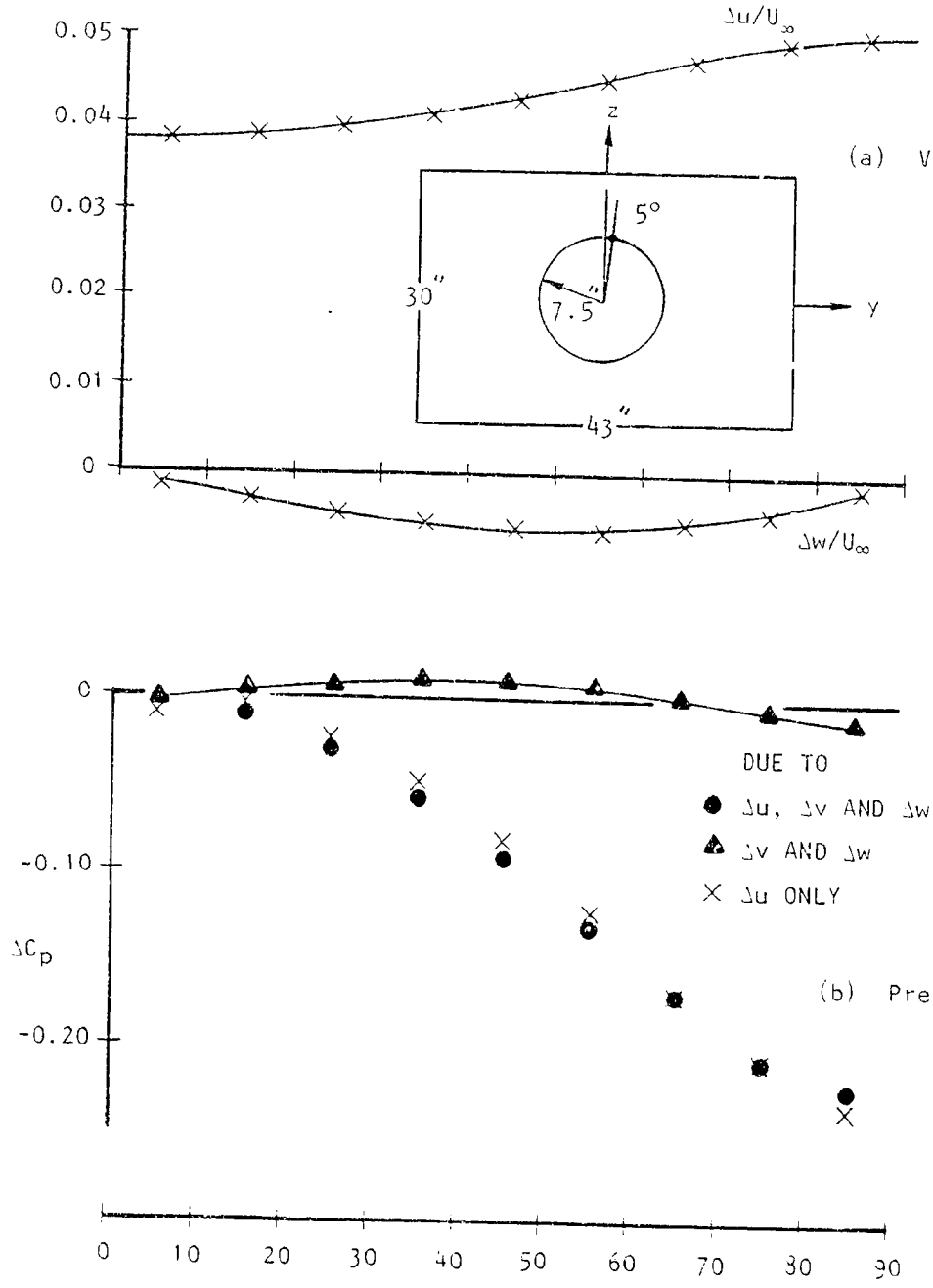

Figure 6.2 Velocity and pressure increments on a 15-inch sphere in a 30 × 43-inch test section.

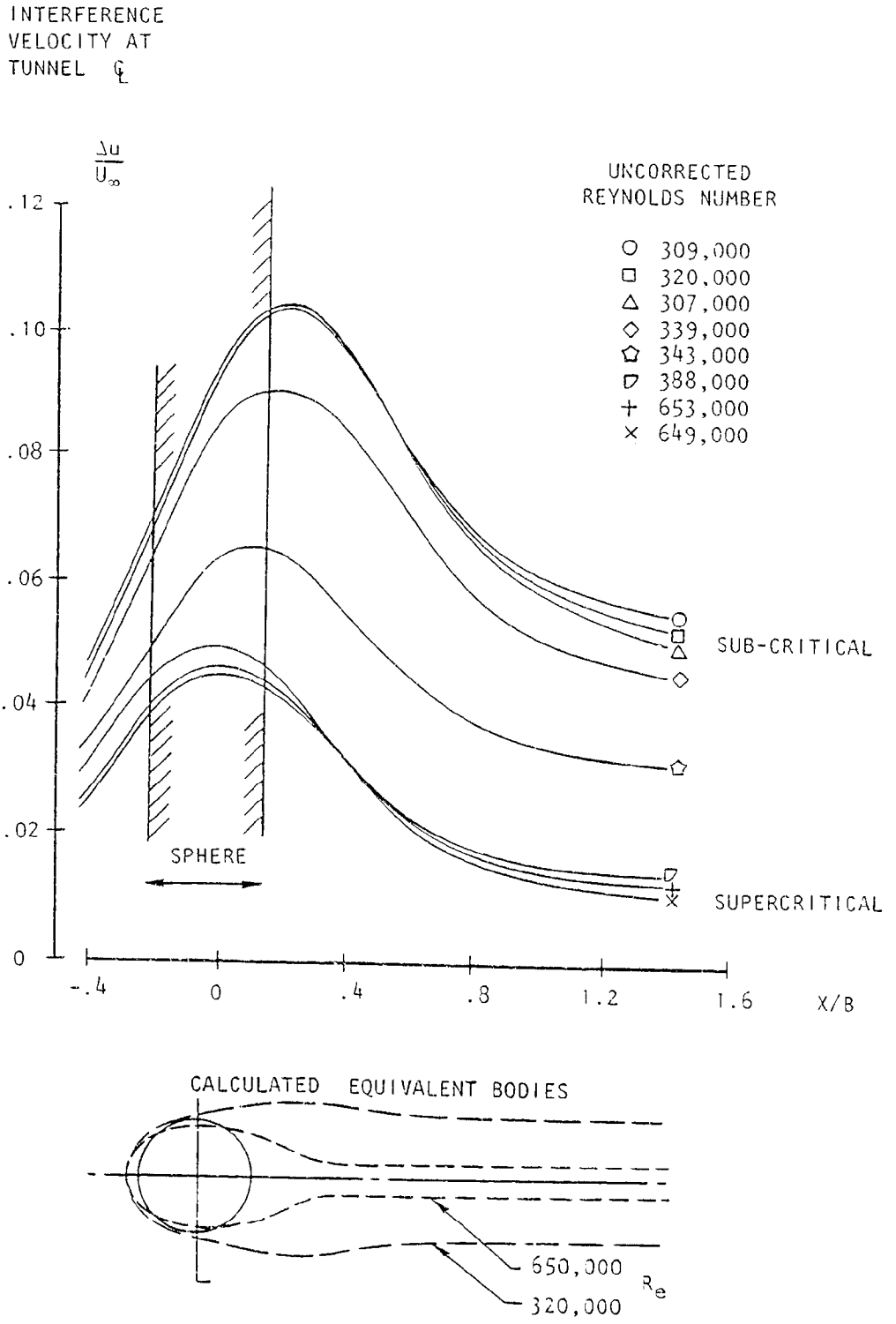

Figure 6.3 Effect of sphere Reynolds number on tunnel blockage velocity distribution: 15-inch sphere.

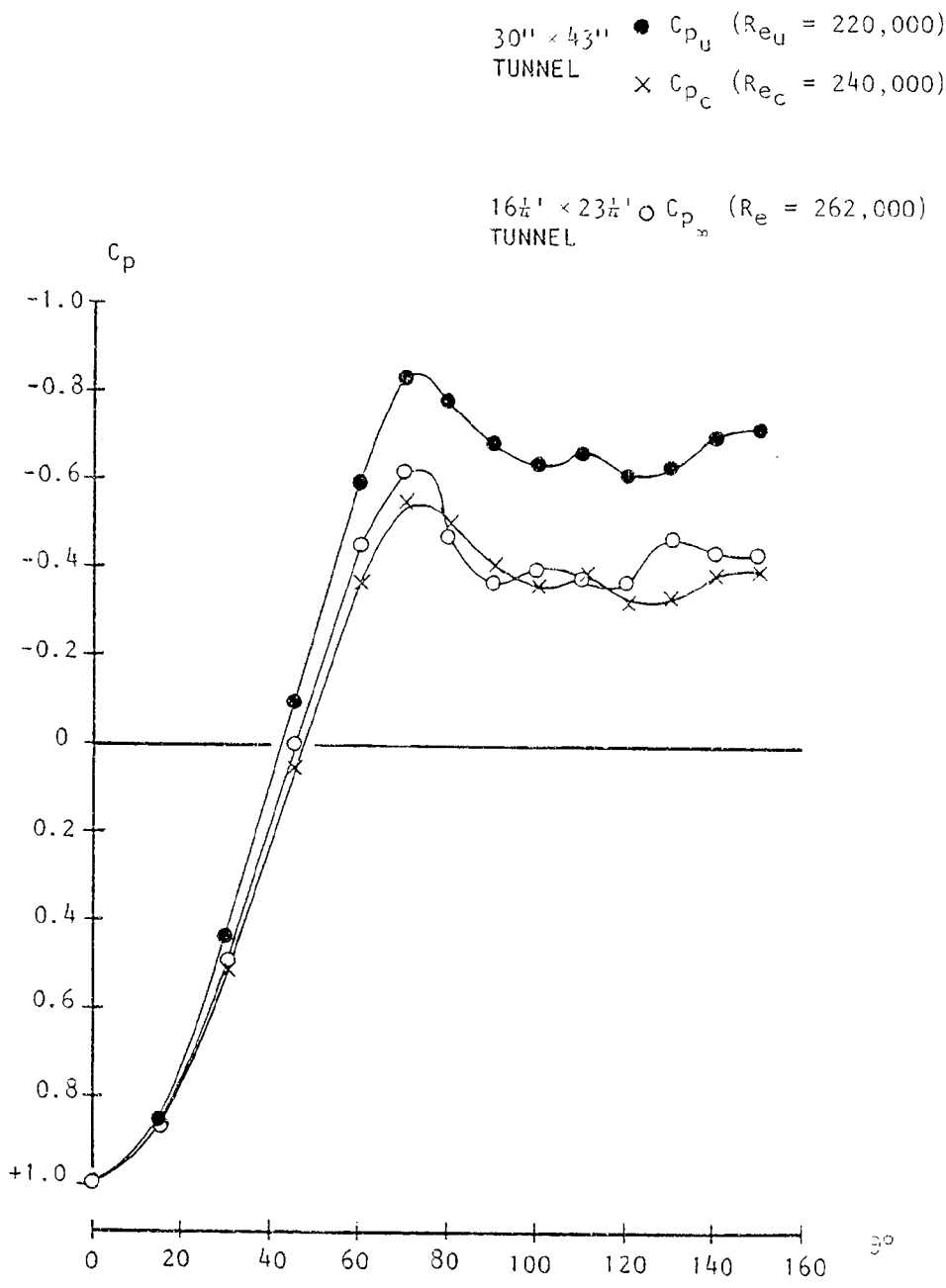

Figure 6.4 Application of pressure correction procedure to 15-inch sphere for $R_e < R_{e_{CRIT}}$

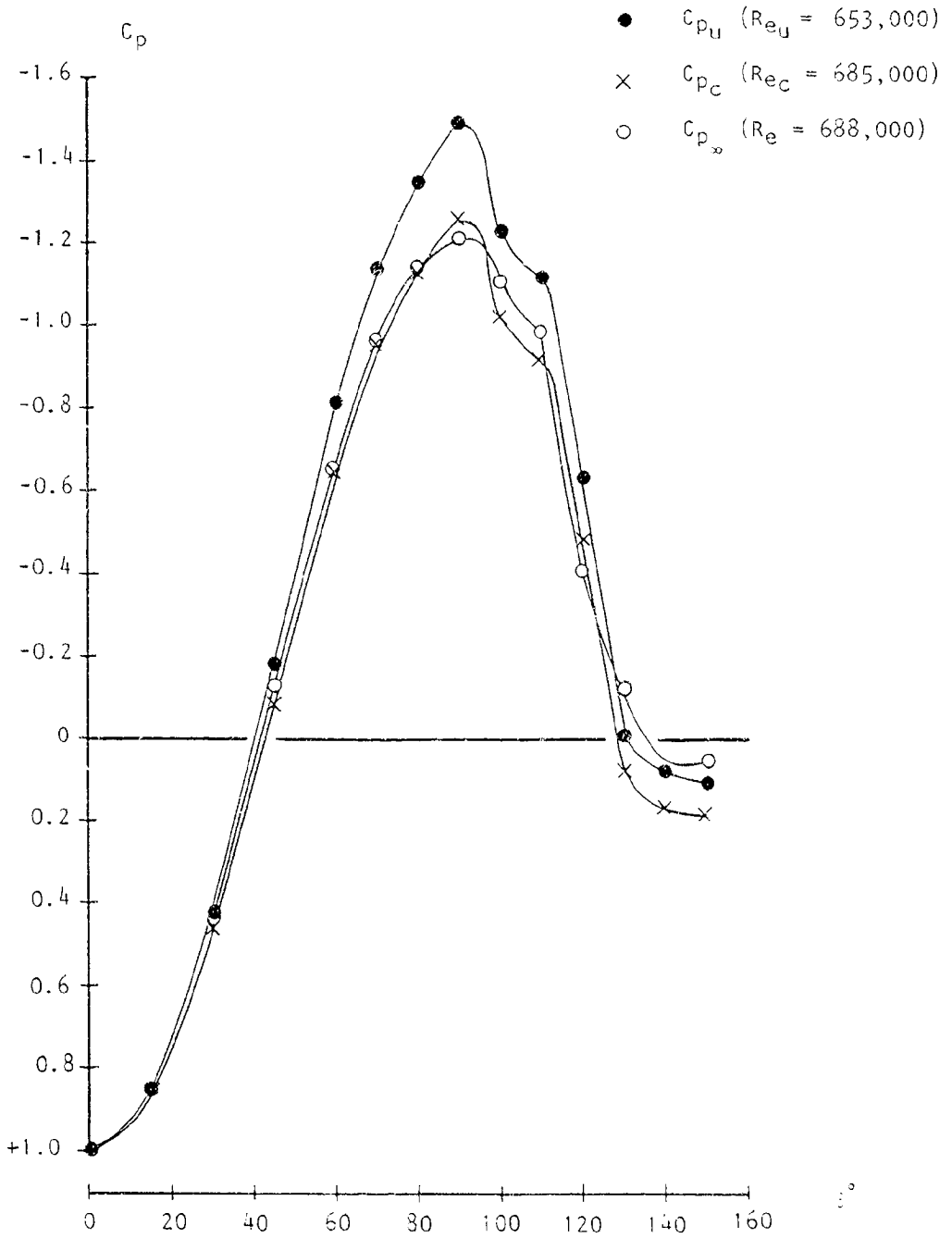

Figure 6.5 Application of pressure correction procedure at 15-inch sphere for $R_e > Re_{CRIT}$

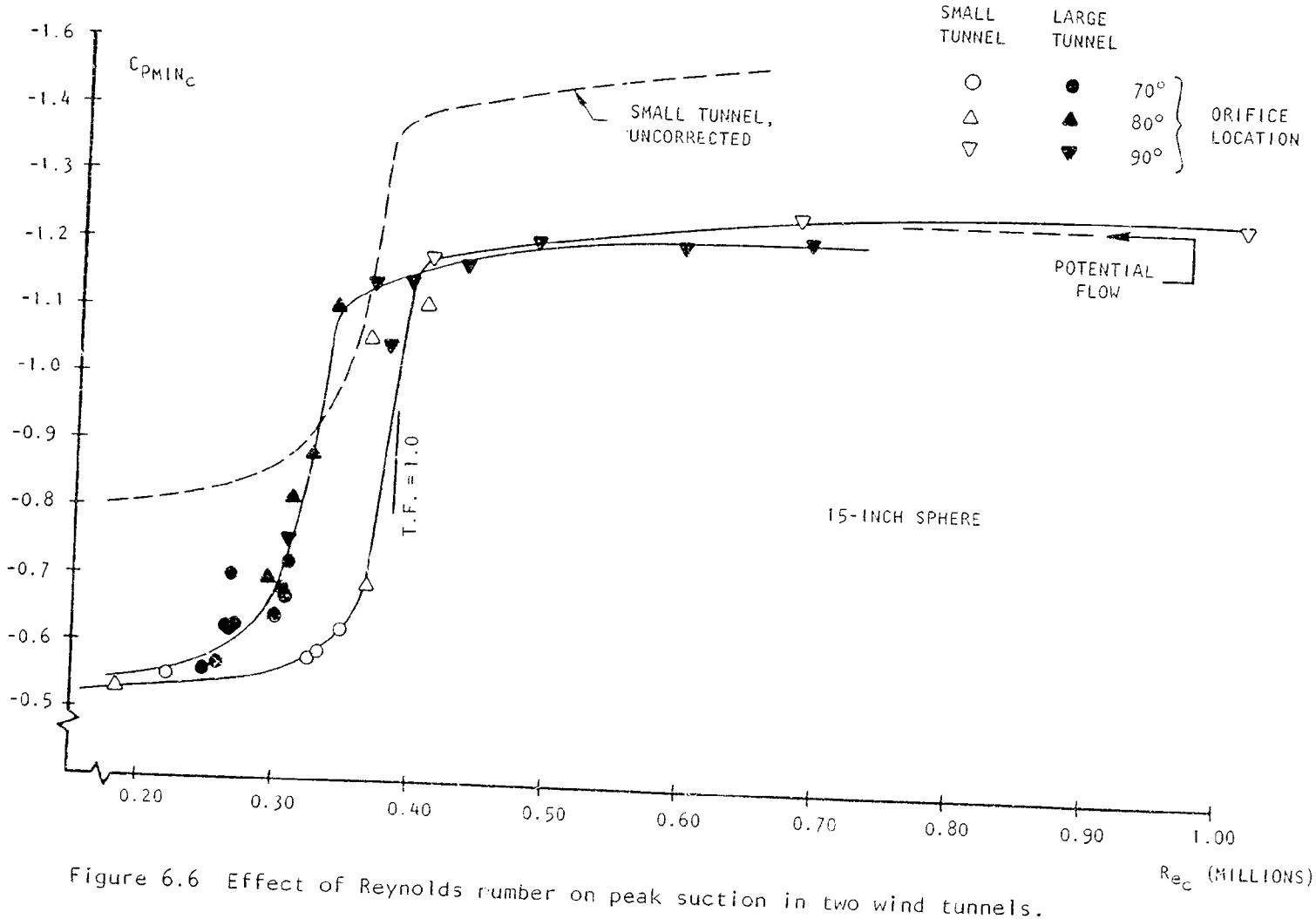

Figure 6.6 Effect of Reynolds number on peak suction in two wind tunnels.

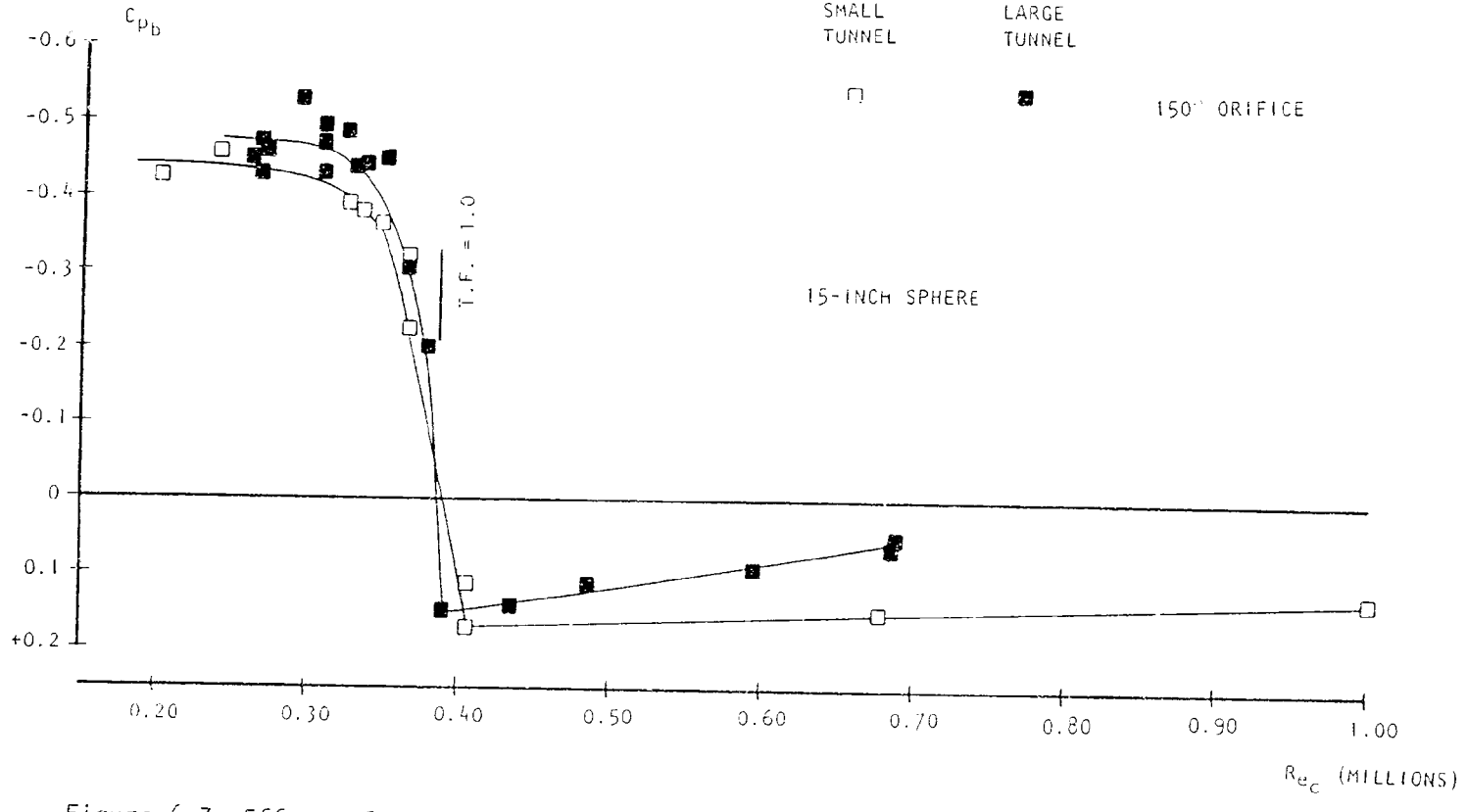

Figure 6.7 Effect of Reynolds number on base pressure in two wind tunnels.

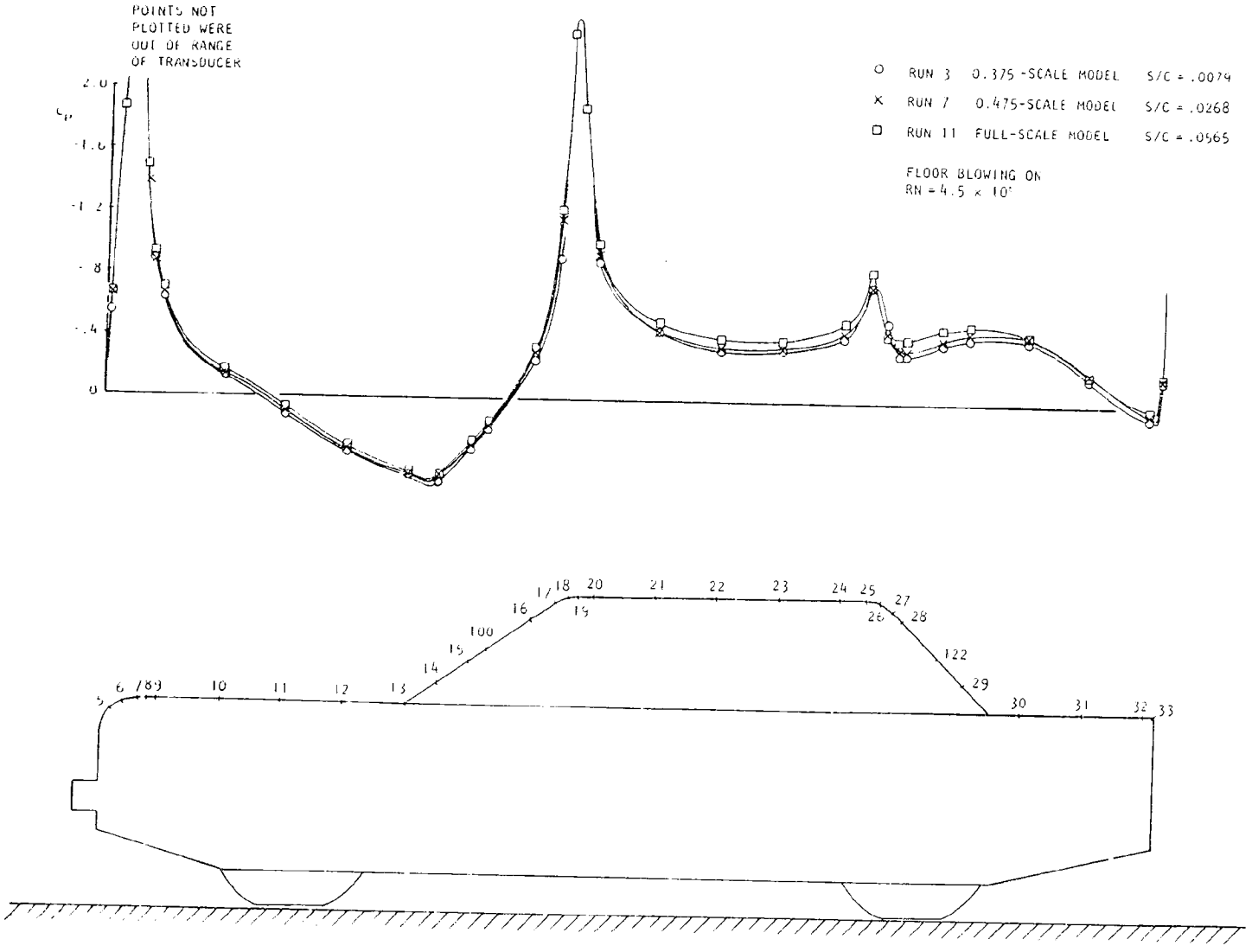

Figure 6.8 Pressure distributions on car centerline - no corrections applied.

C - 7

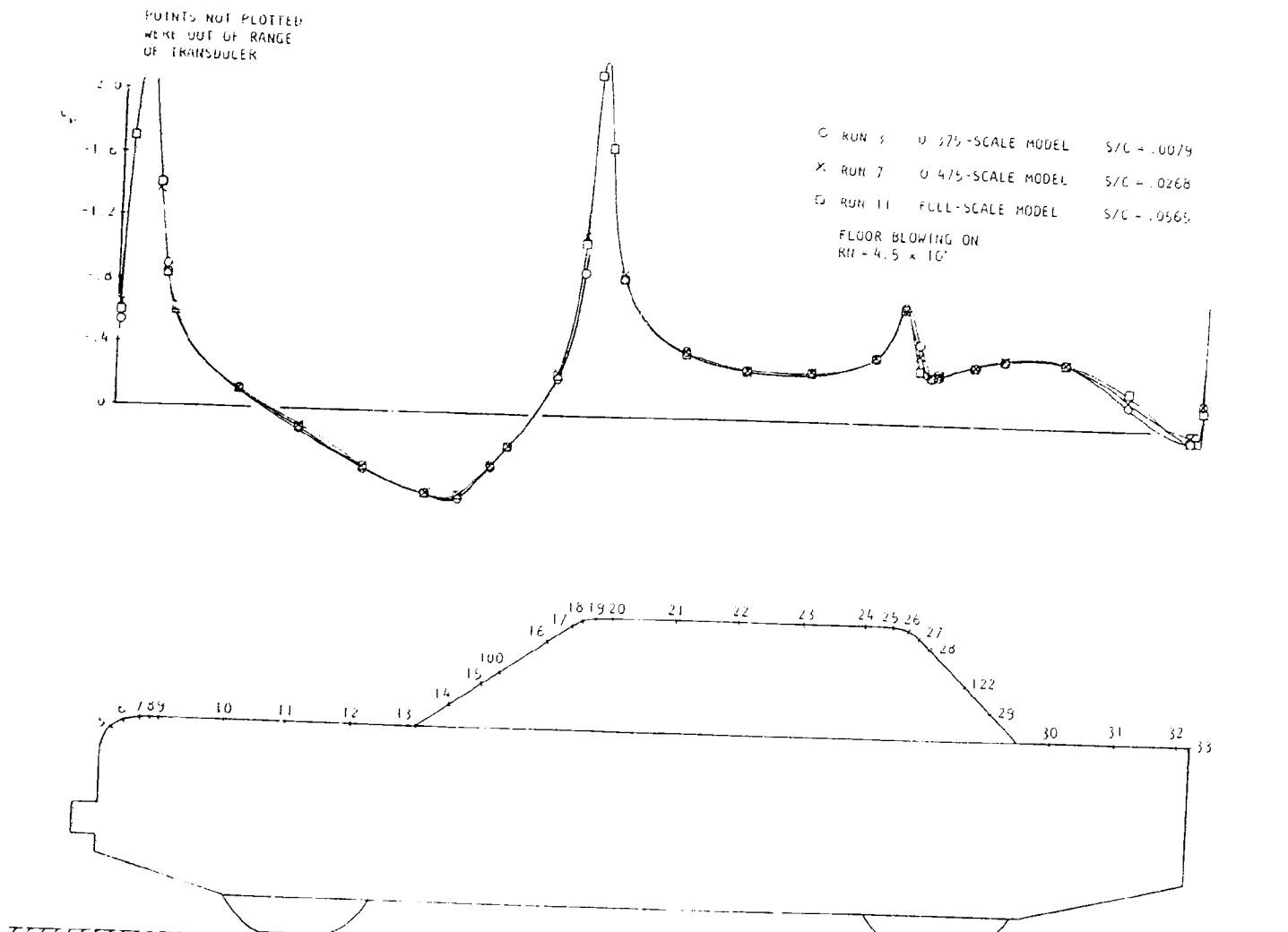

Figure 6.9 Pressure distributions on car centerline - corrected using wall signature method.

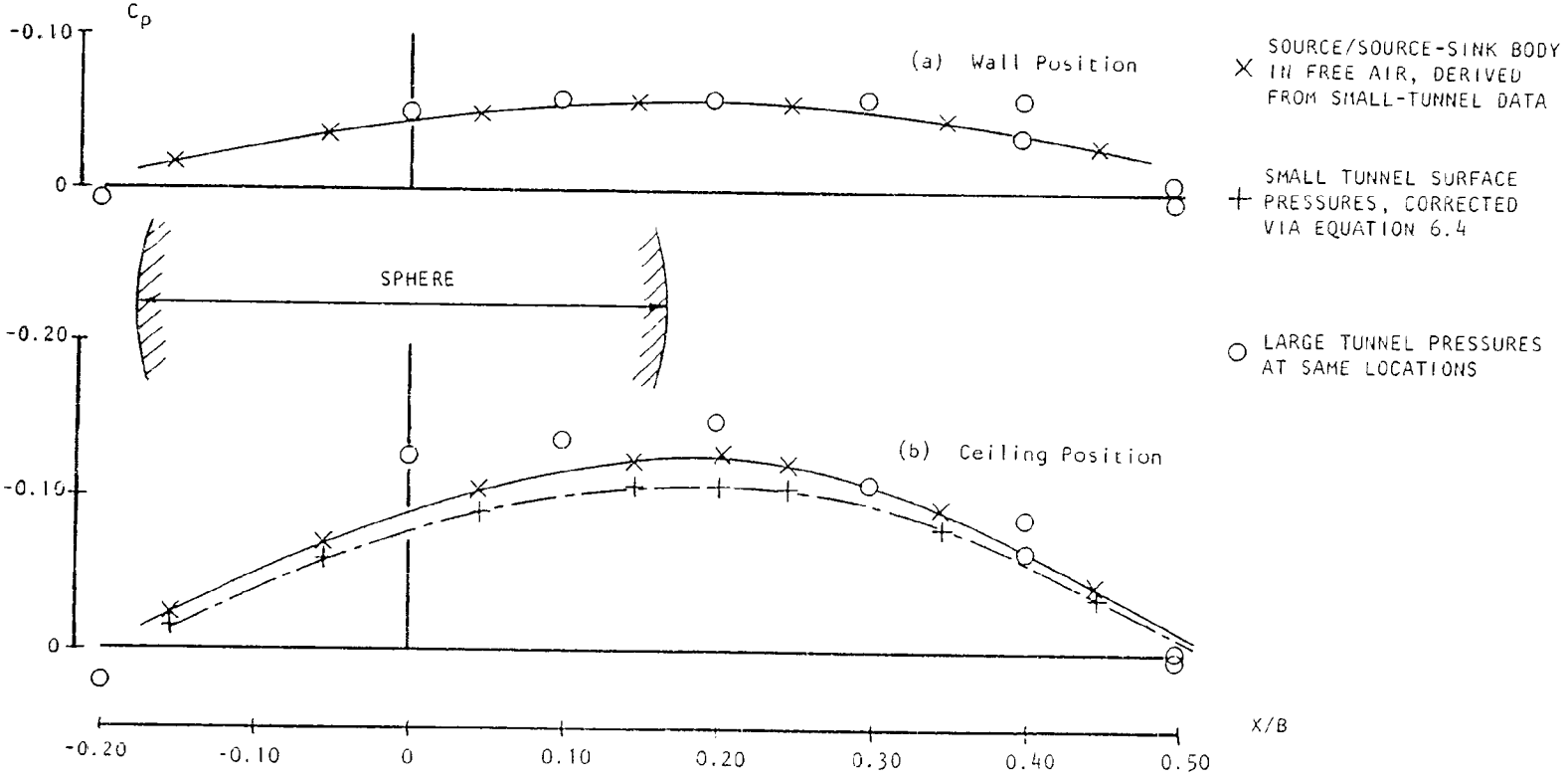

Figure 6.10 Determination of off-body, free-air pressures – Subcritical 15" sphere.

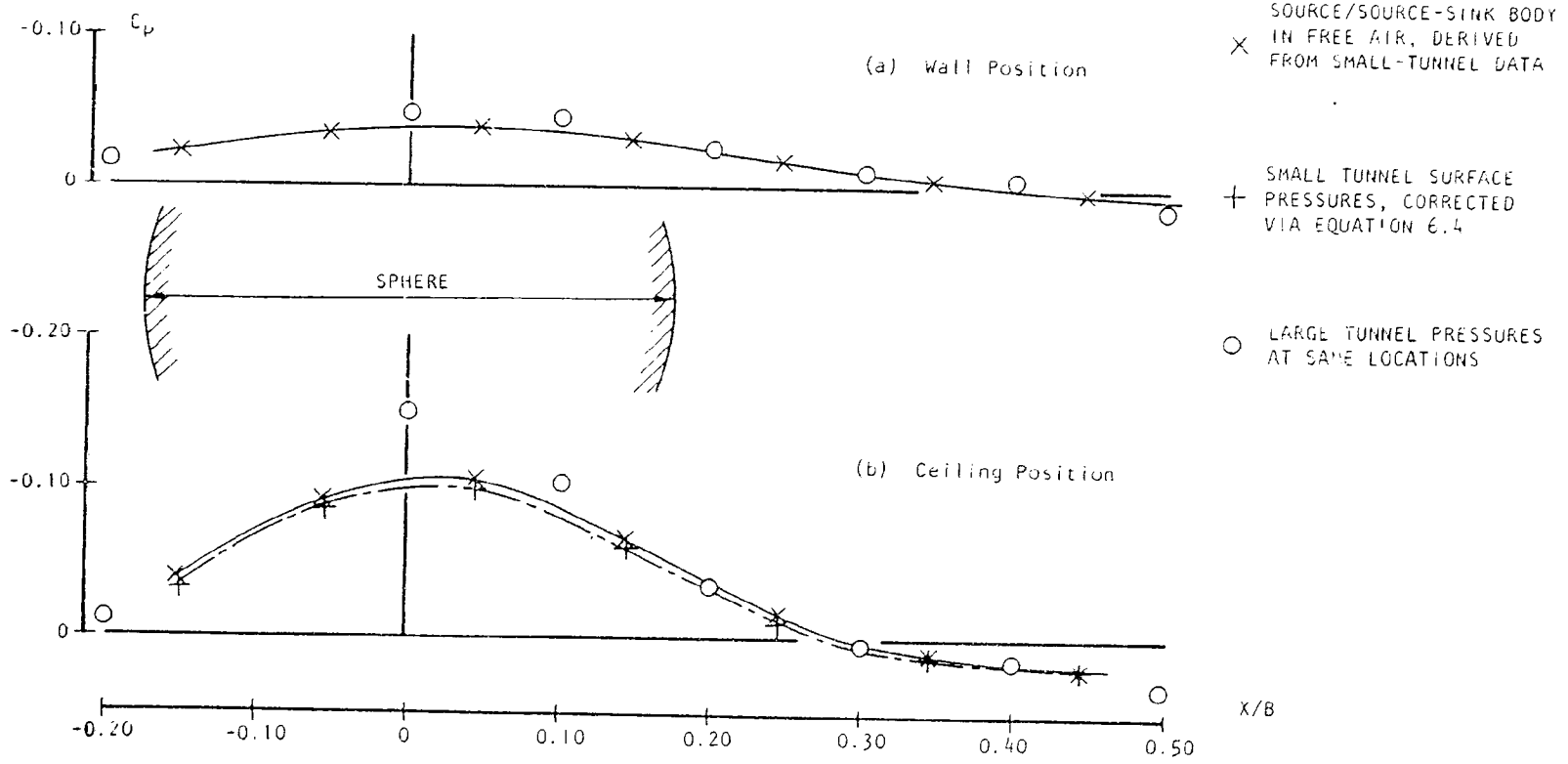

Figure 6.11 Determination of off-body, free-air pressures - Supercritical 15" sphere.

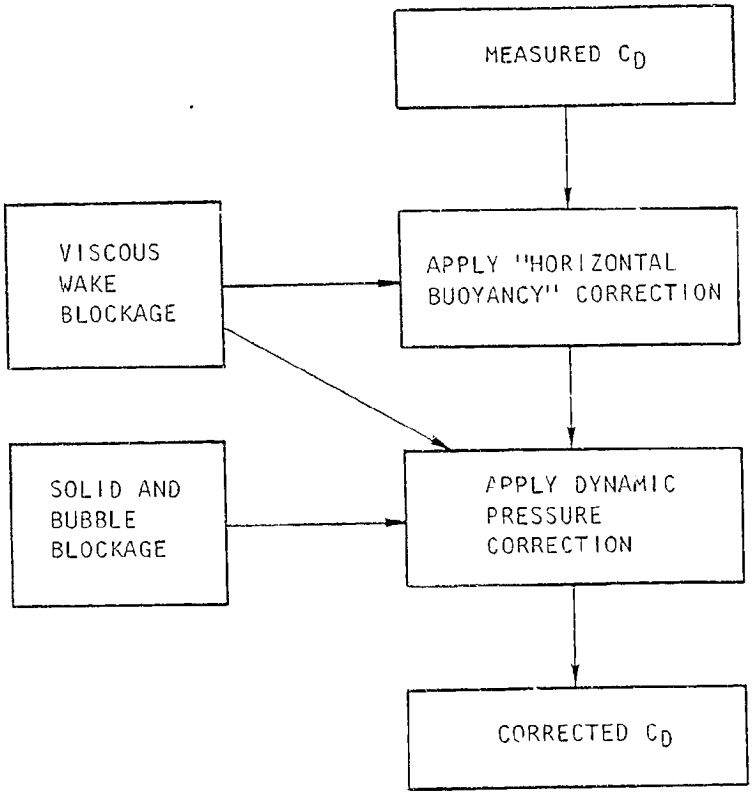

Figure 7.1 Drag correction sequence.

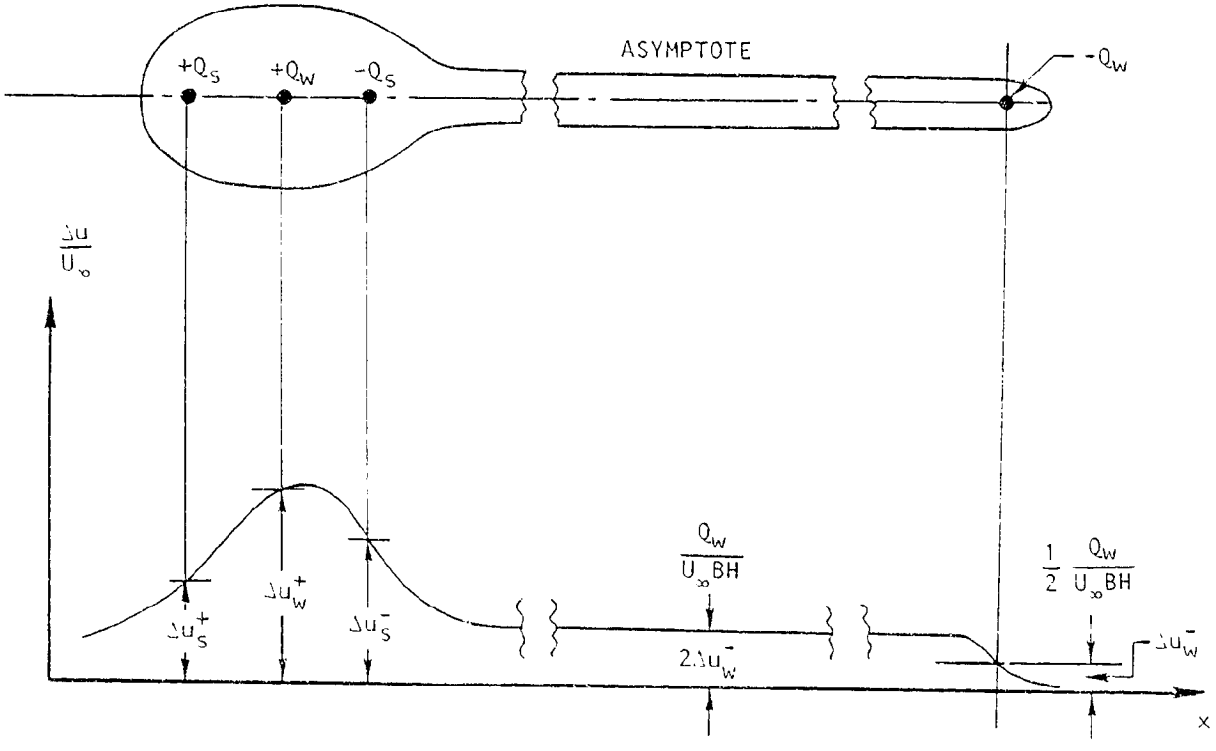

Figure 7.2 Flow model for blockage estimation.

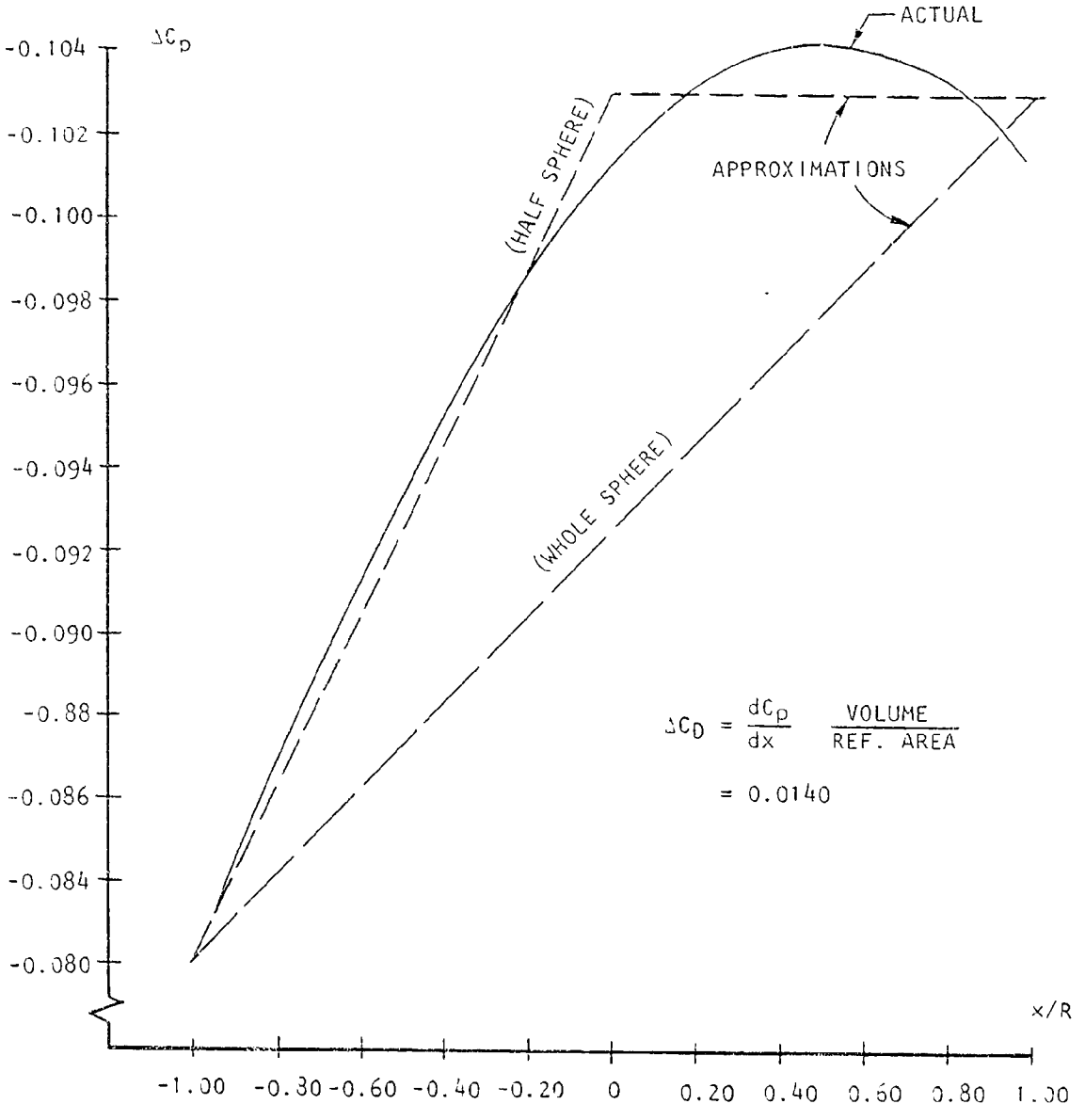

Figure 7.3 Conventional determination of buoyancy drag.

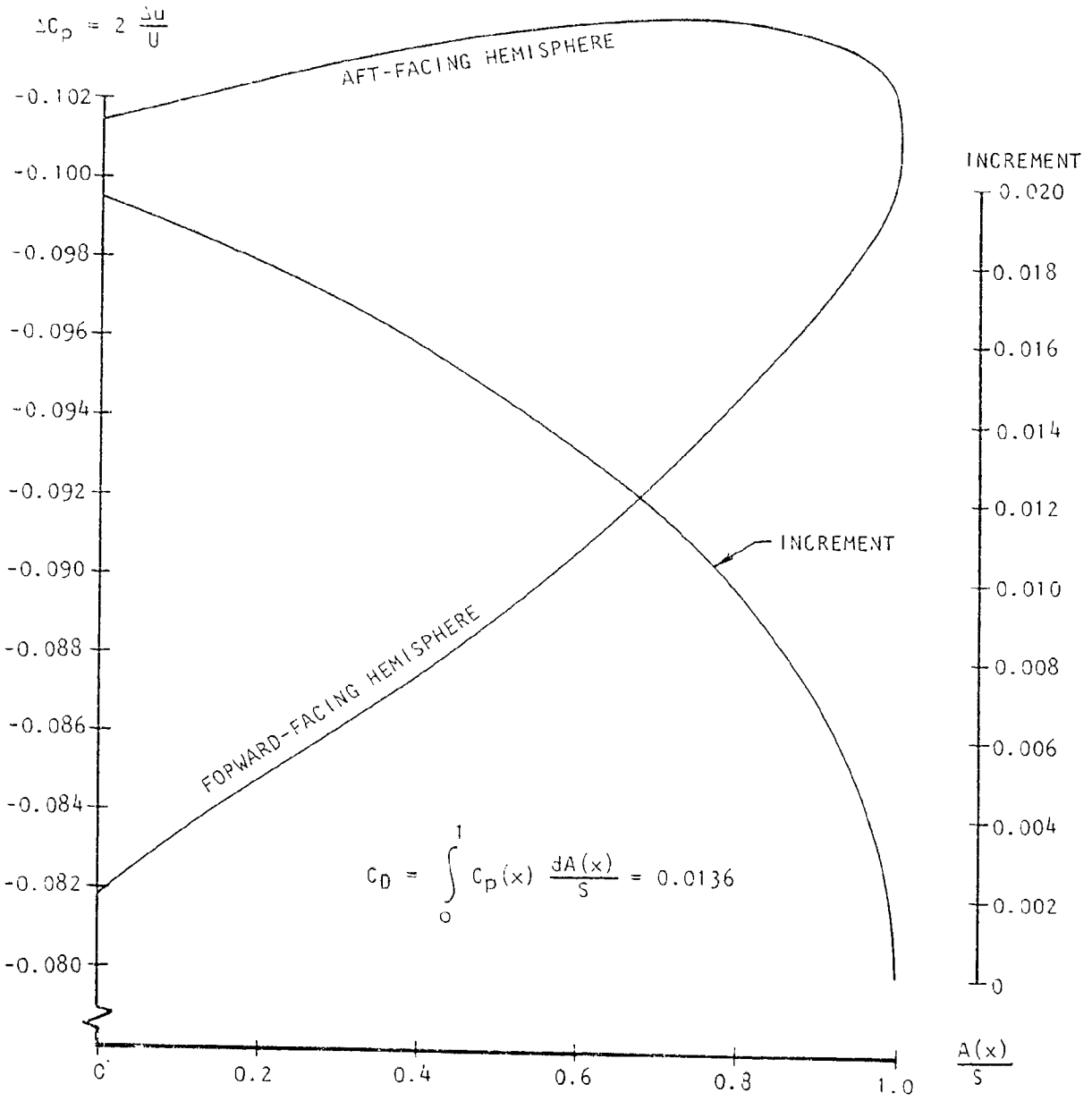

Figure 7.4 Buoyancy drag integration using linearized ΔC_p's.

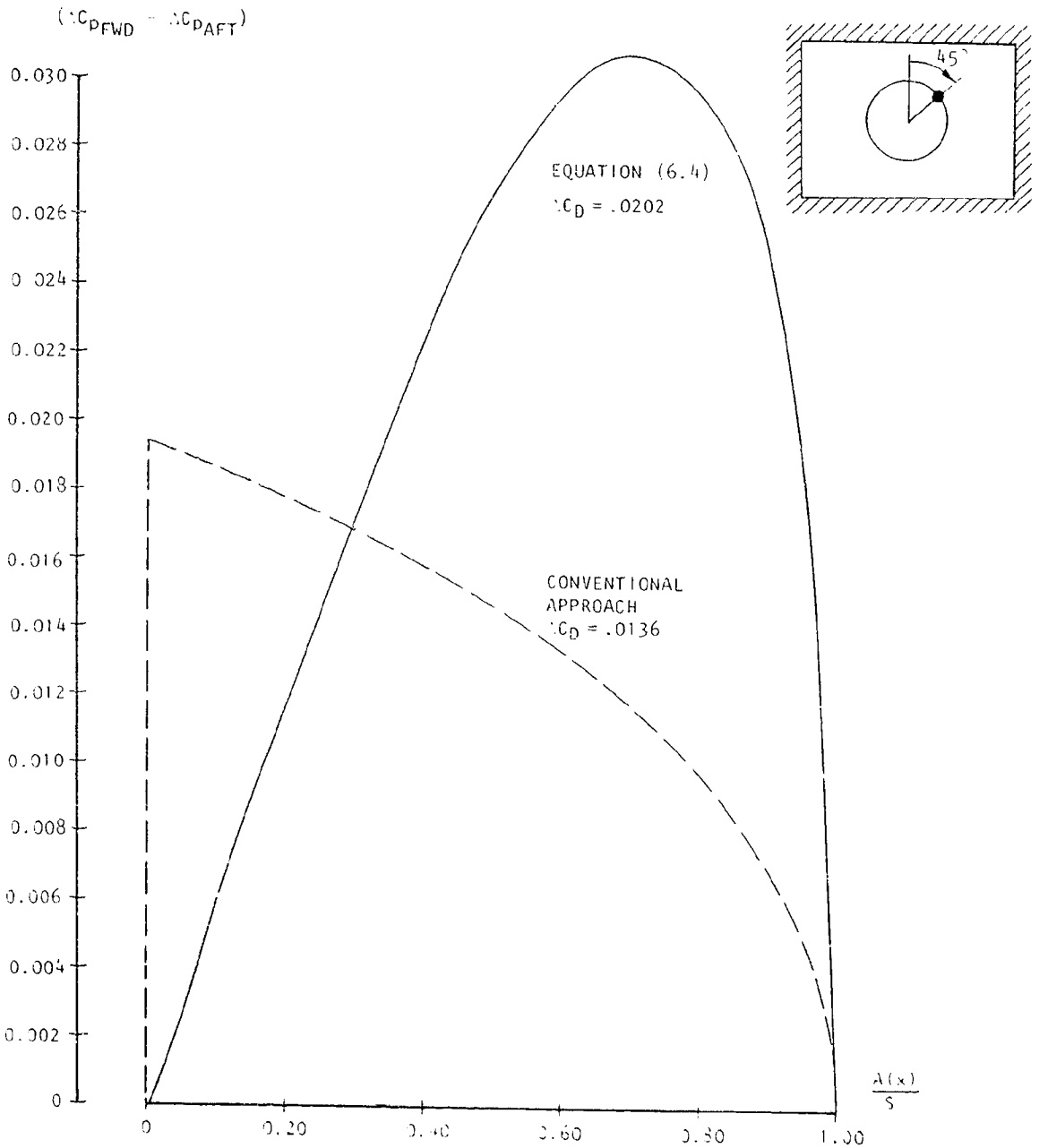

Figure 7.5 Buoyancy drag integration using equation (6.4).

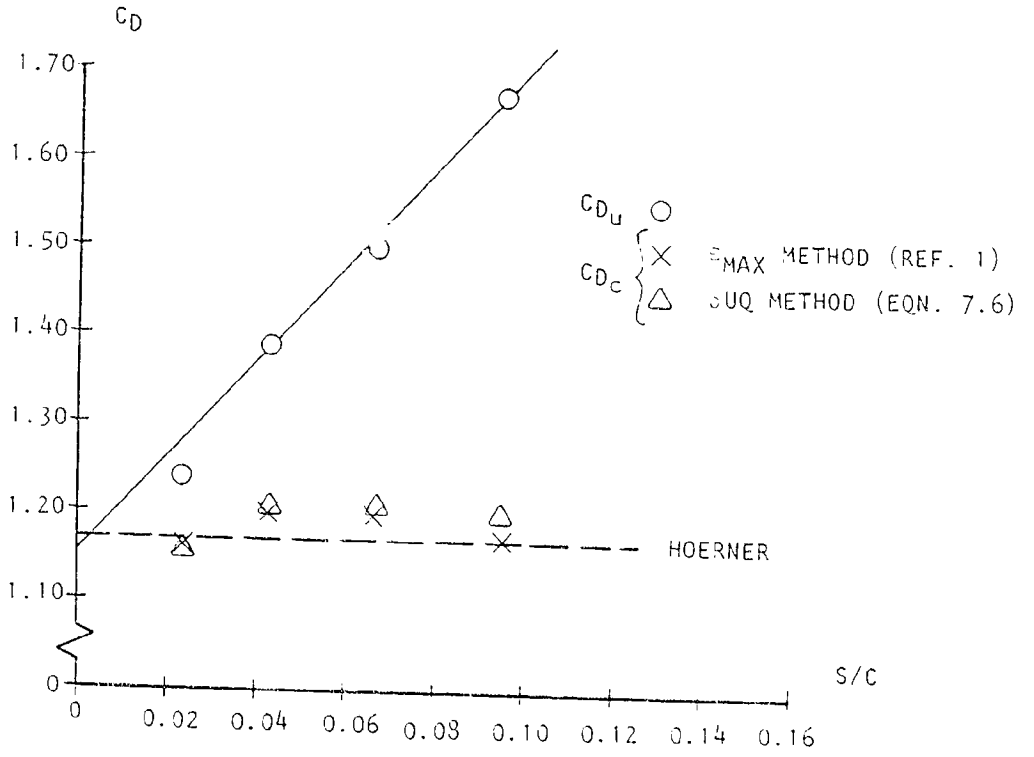

Figure 7.6 Drag of square normal plates in the 16½ × 23½-foot tunnel.

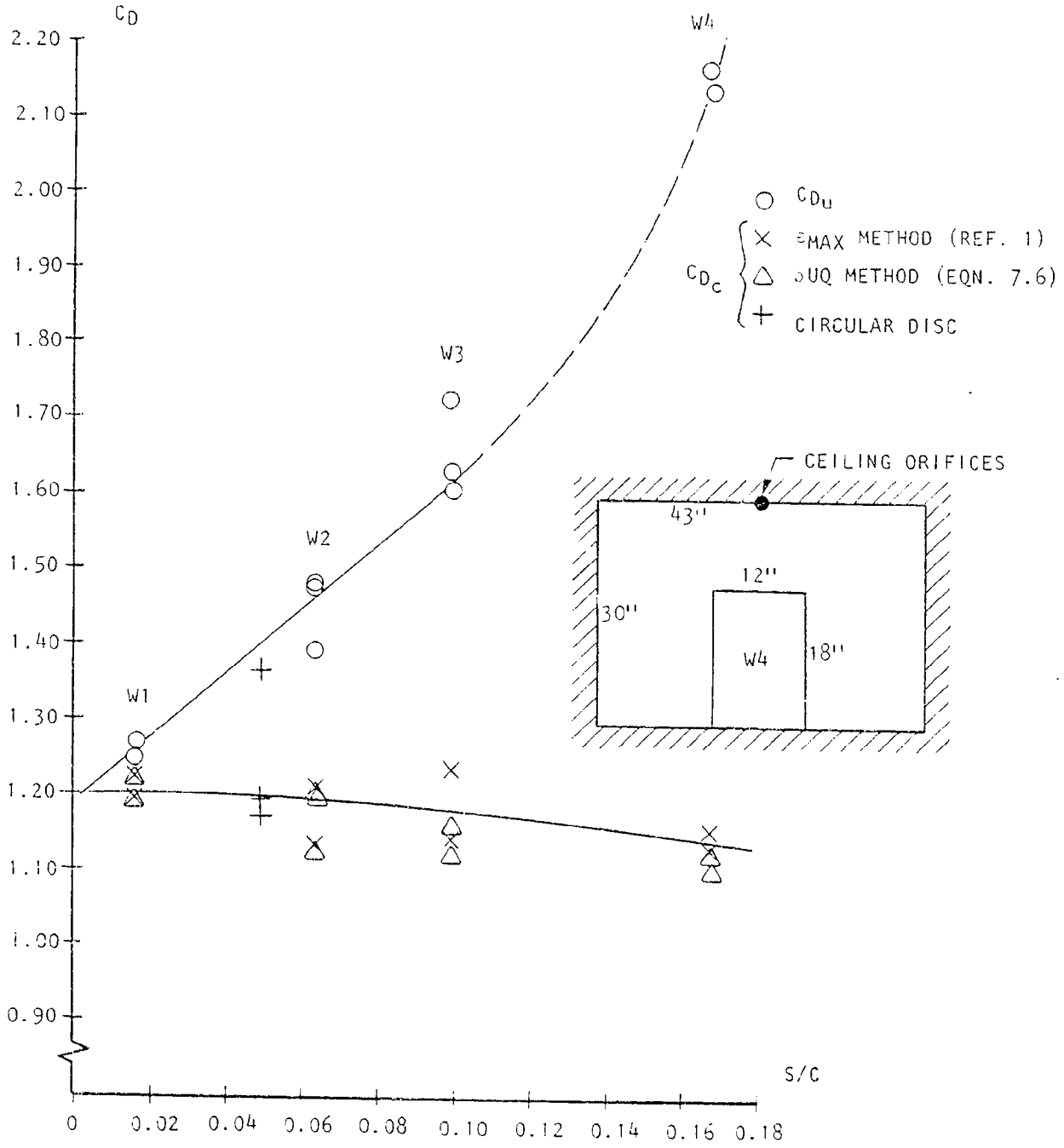

Figure 7.7 Drag of rectangular plates in the 30" x 43" tunnel.

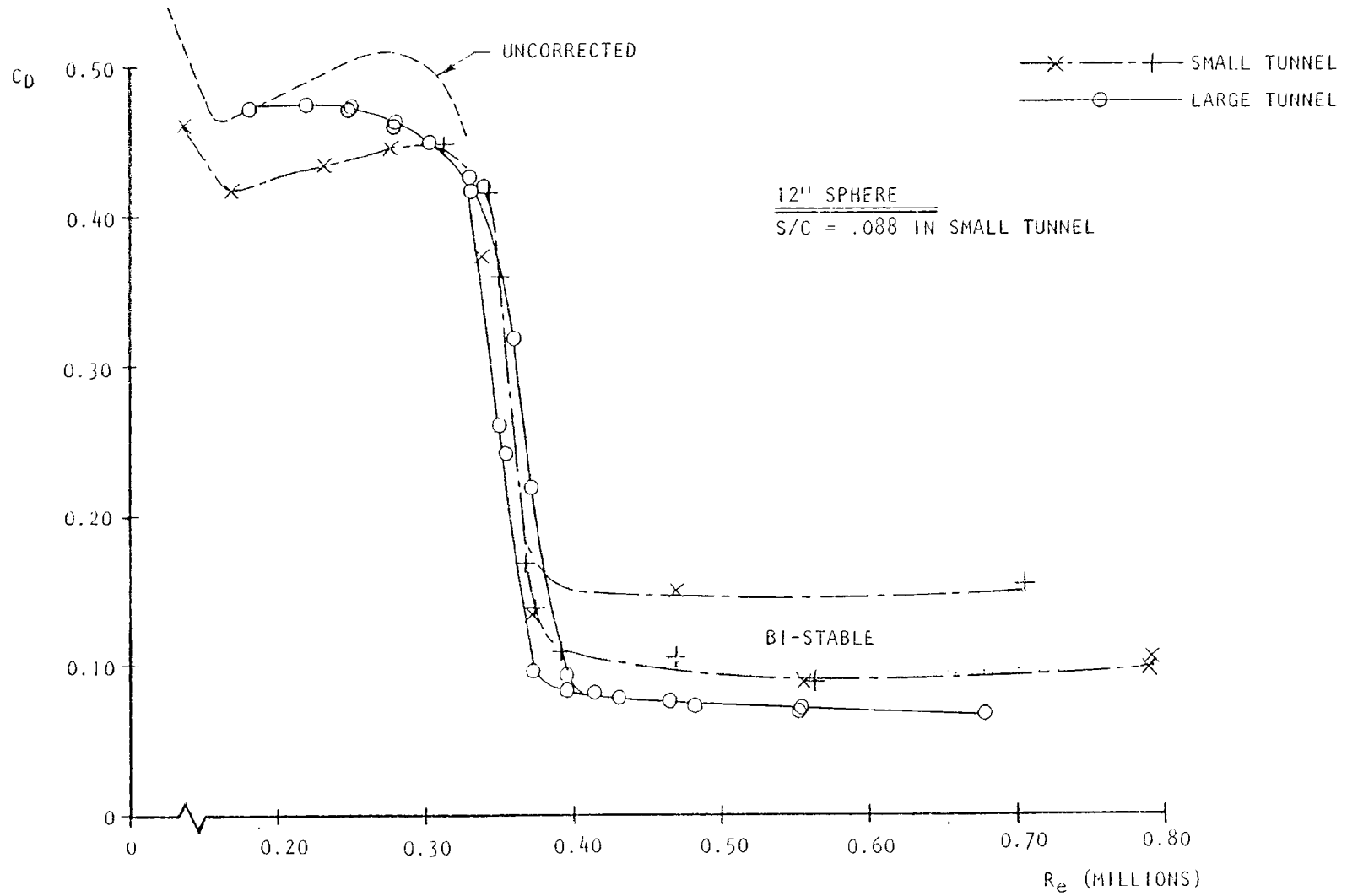

Figure 7.8 Large-tunnel and corrected small-tunnel drag coefficients for a 12-inch sphere.

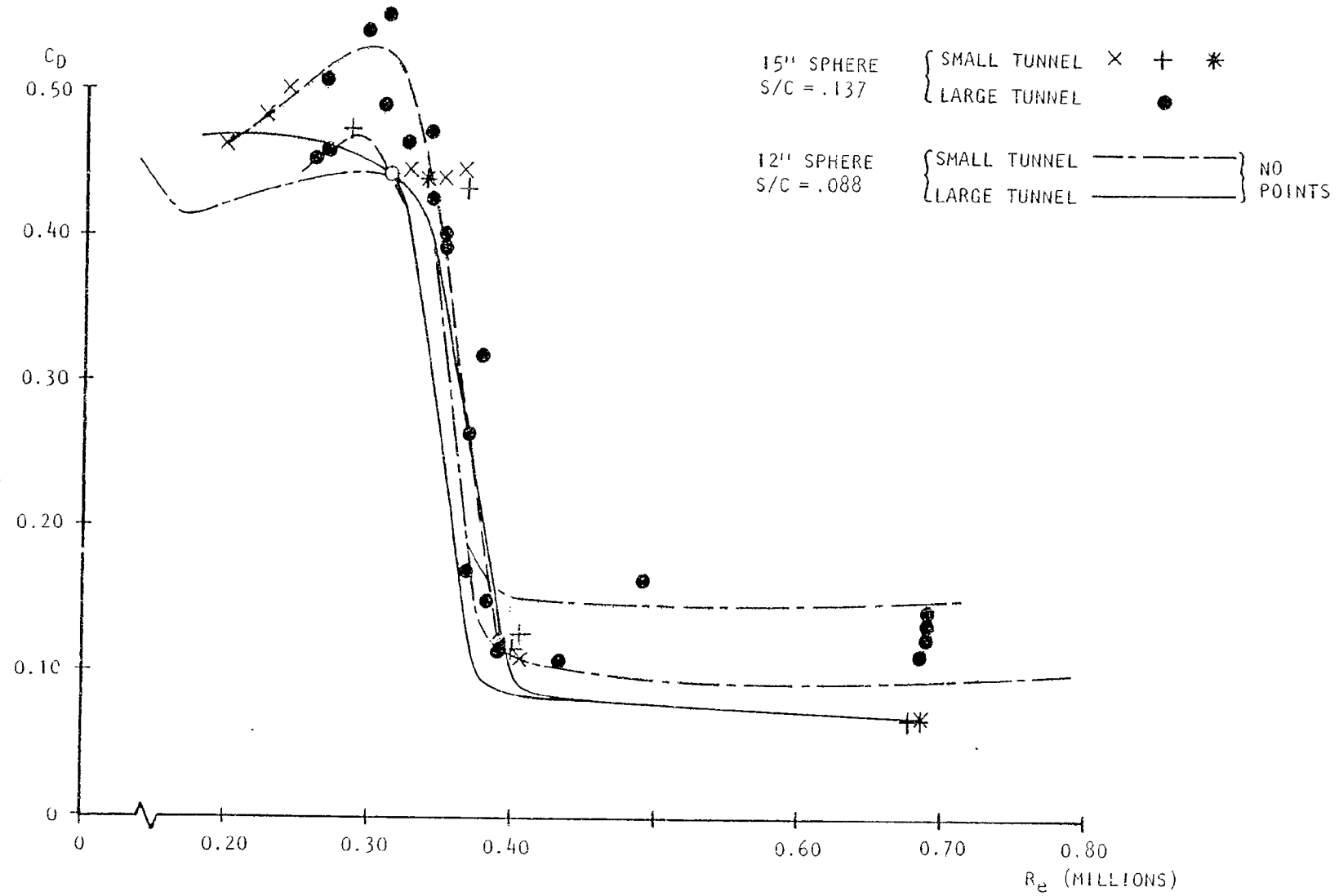

Figure 7.9 Large-tunnel and corrected small-tunnel drag coefficients for 15- and 12-inch spheres.

SYMBOL	WING	S/C	Re_u (MILLION)
○	W4	16.7%	.460
+	W3	9.8%	.454
×	W2	6.3%	.453
◇	W1	1.6%	.433

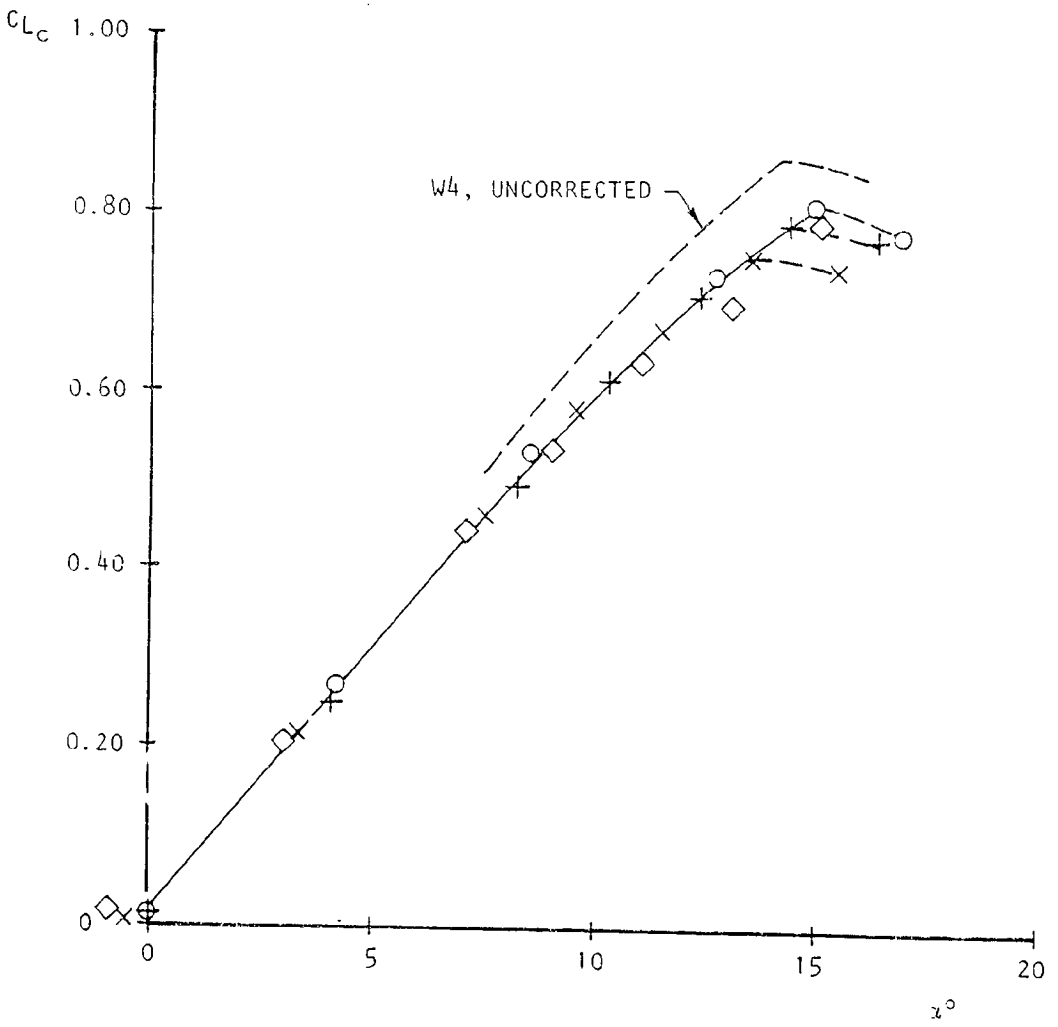

Figure 3.1 Lift correlation for four AR-3 flat plate wings.

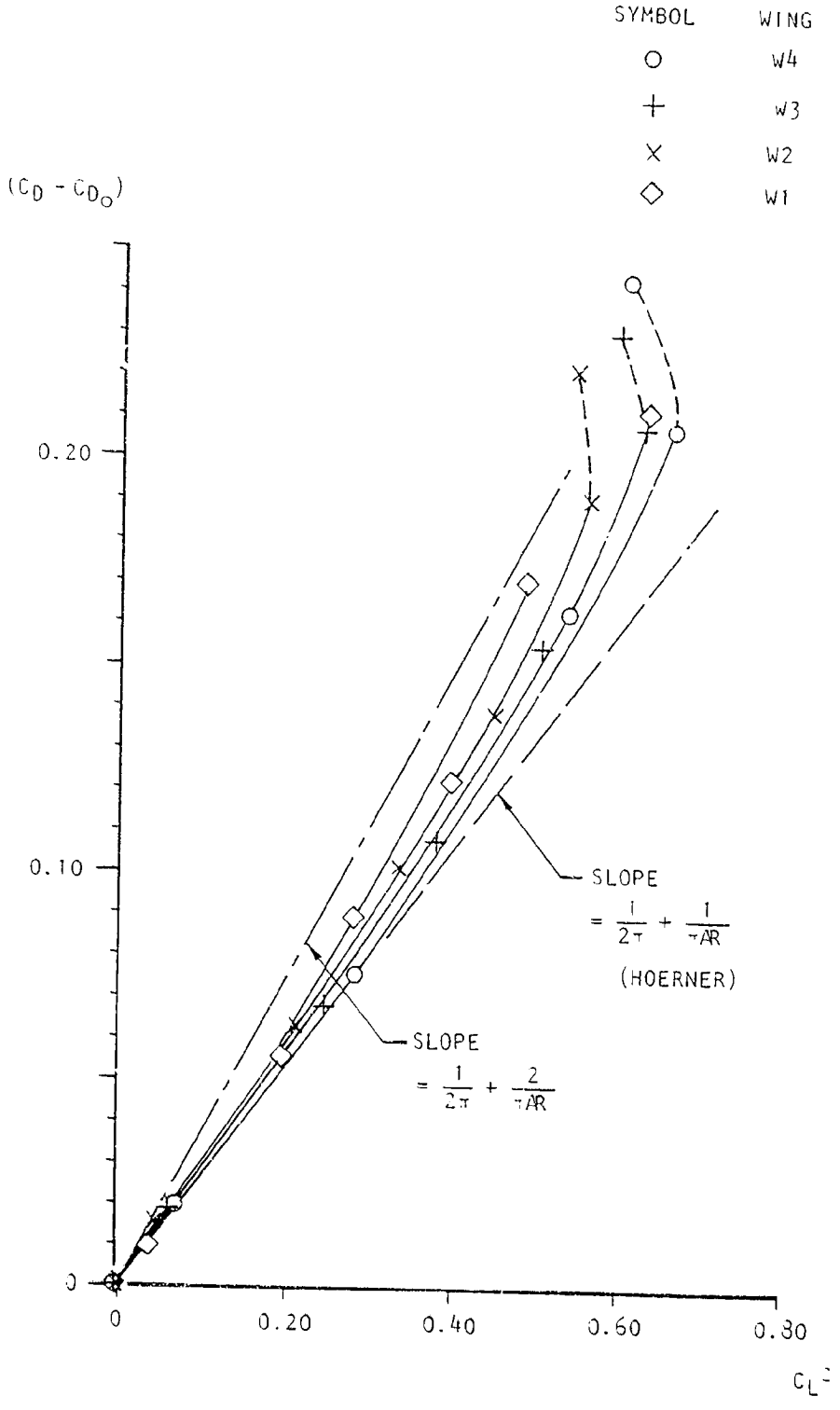

Figure 3.2 Drag correlation for four AR-3 flat plate wings.

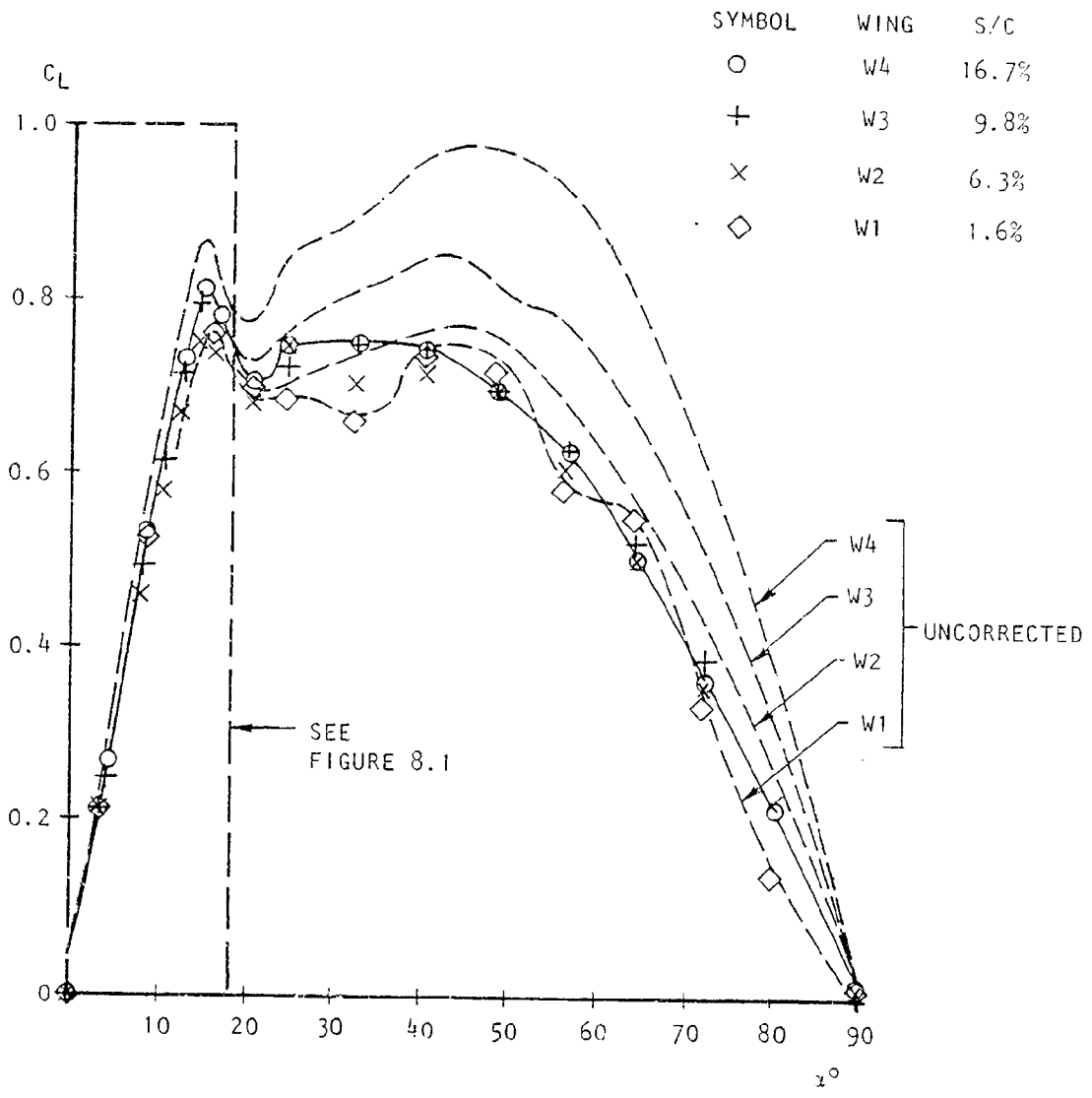

Figure 8.3 Lift correlation for R-3 flat plates at high angles of attack.

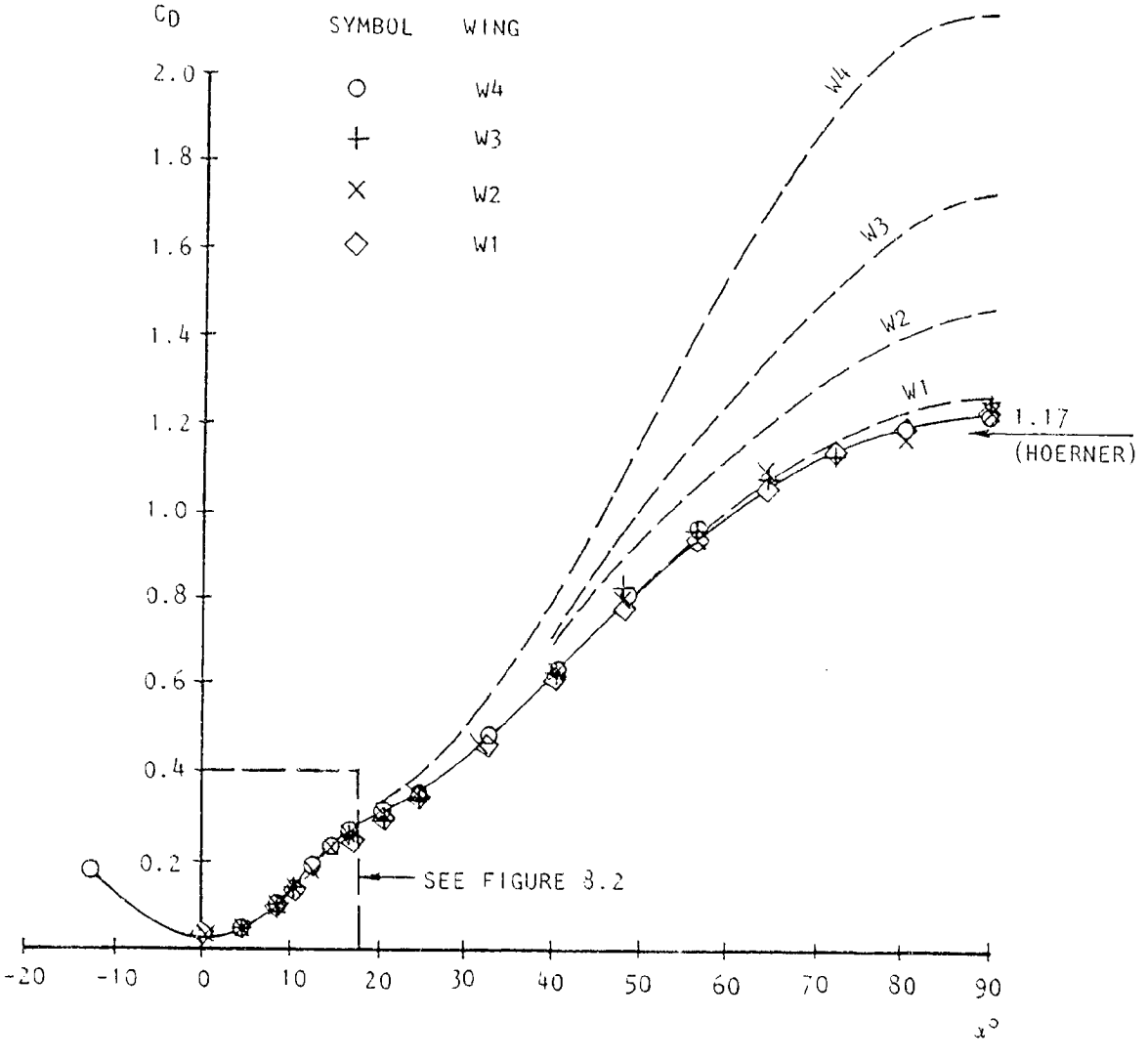

Figure 3.4 Drag correlation for AR-3 flat plates at high angles of attack.

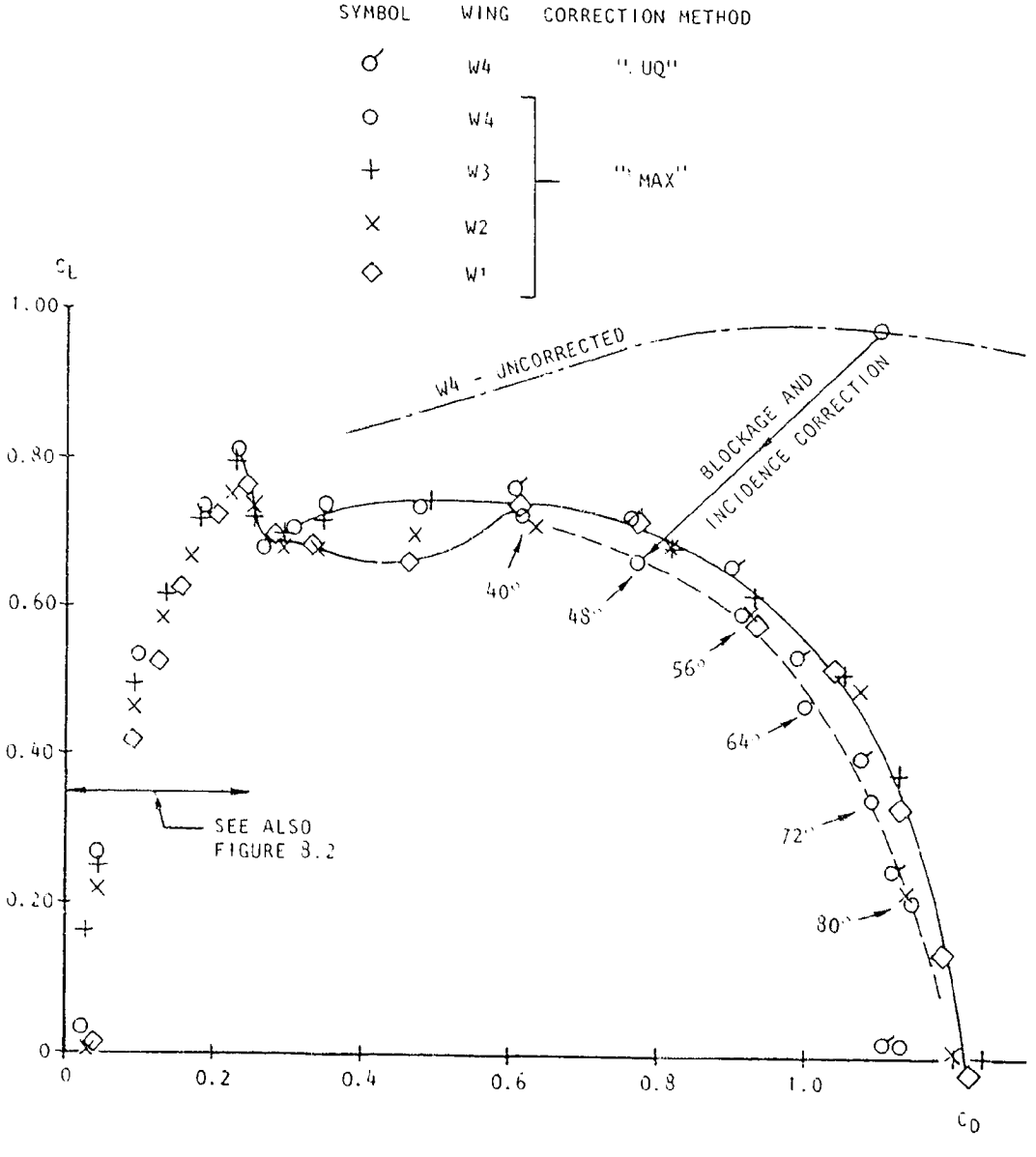

Figure 8.5 Drag Polar for AR-3 flat plates at high angles of attack.

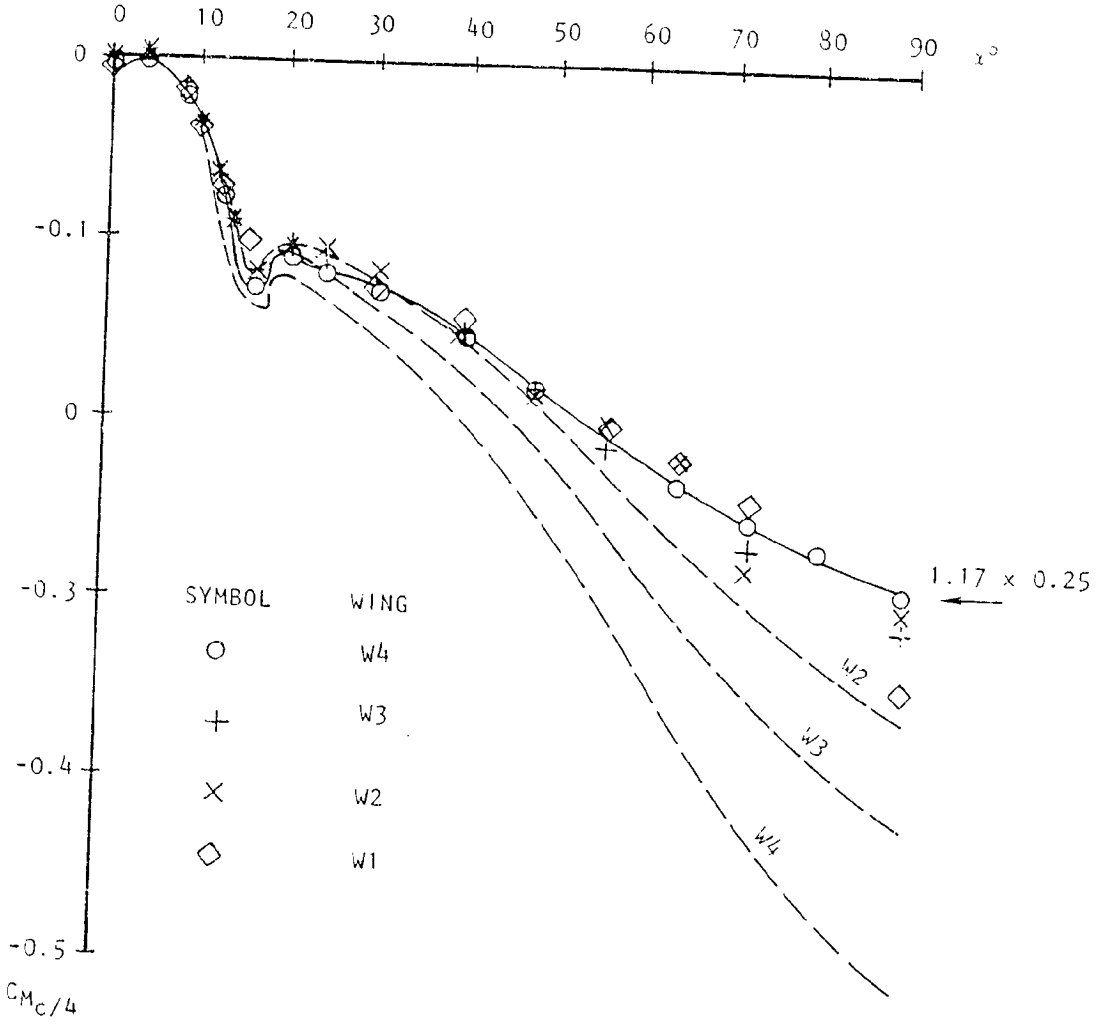

Figure 3.5 Pitching moment correlation for flat plates at high angles of attack.

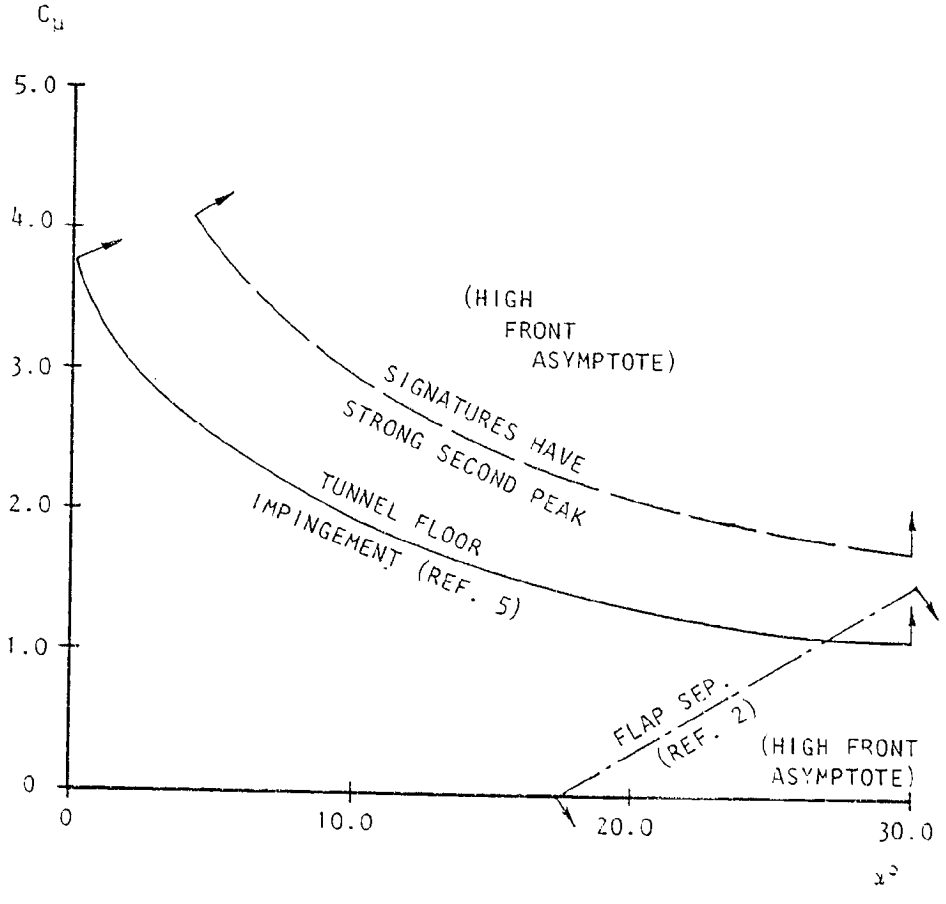

Figure 3.7 Occurrence of floor impingement and flap separation for KBF model in 30" x 43" tunnel.

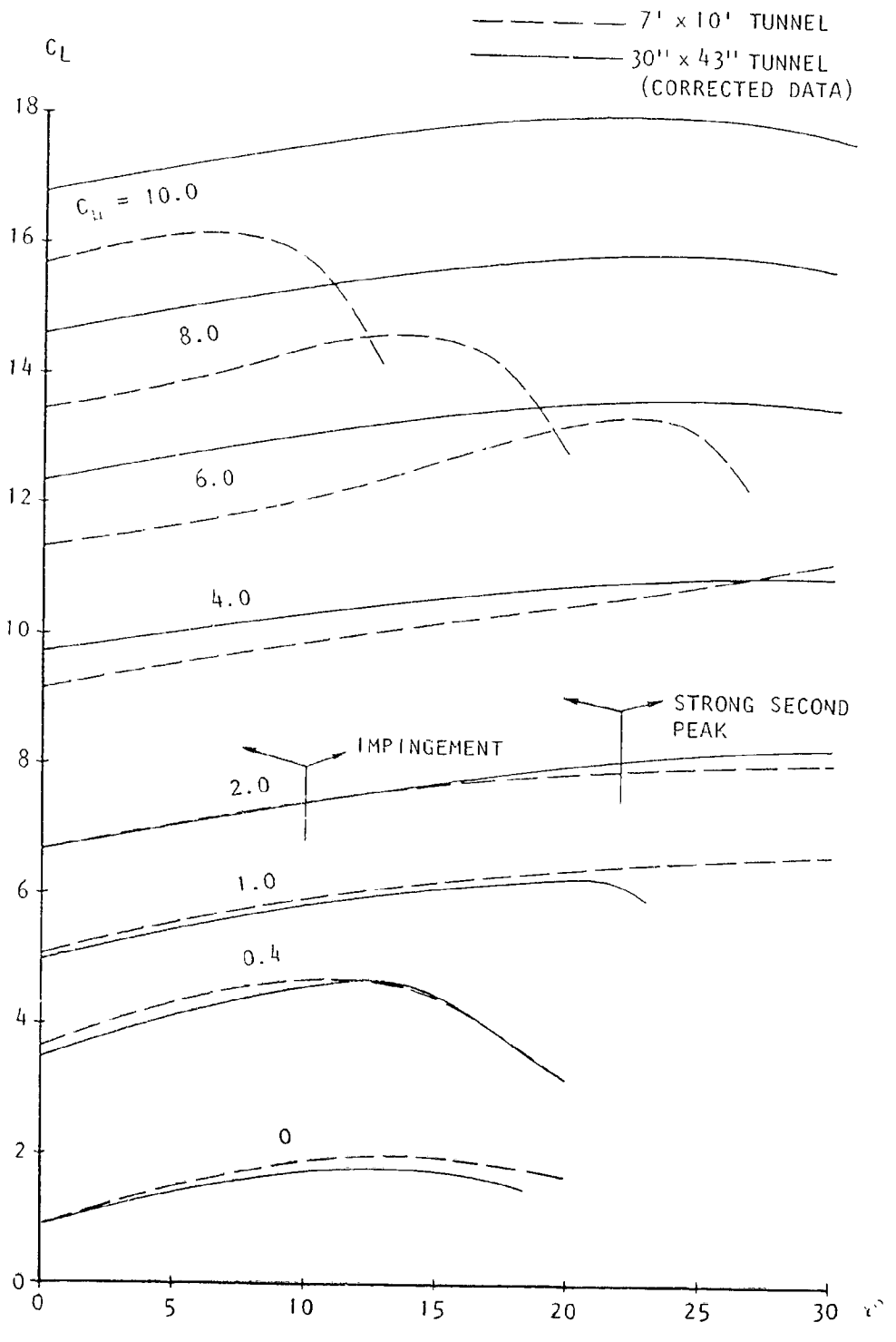

Figure 8.8 Large tunnel and corrected small tunnel lift for knee-blown flap model, including highest power settings.

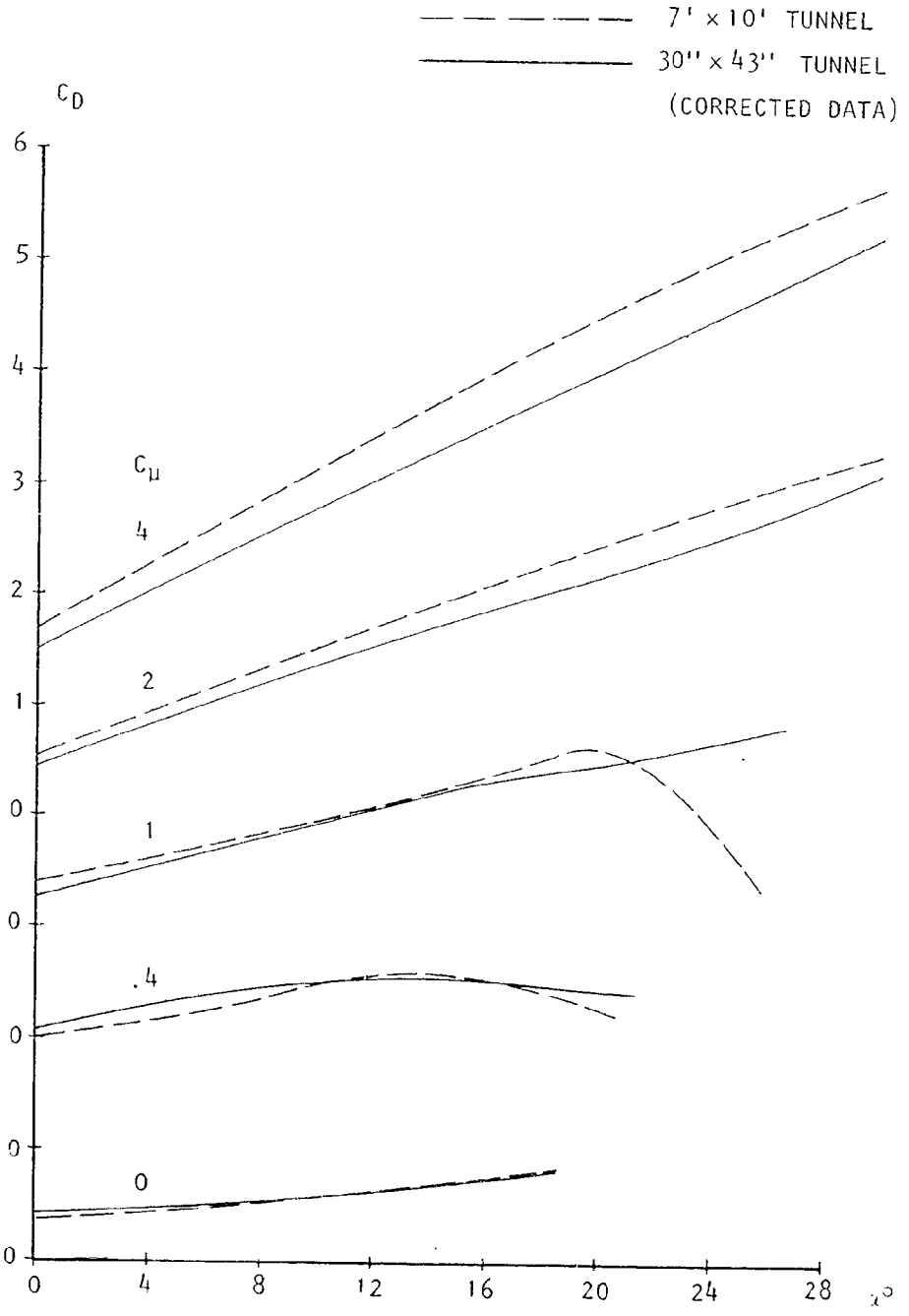

Figure 8.9 Large tunnel and corrected small tunnel drag for KBF model.

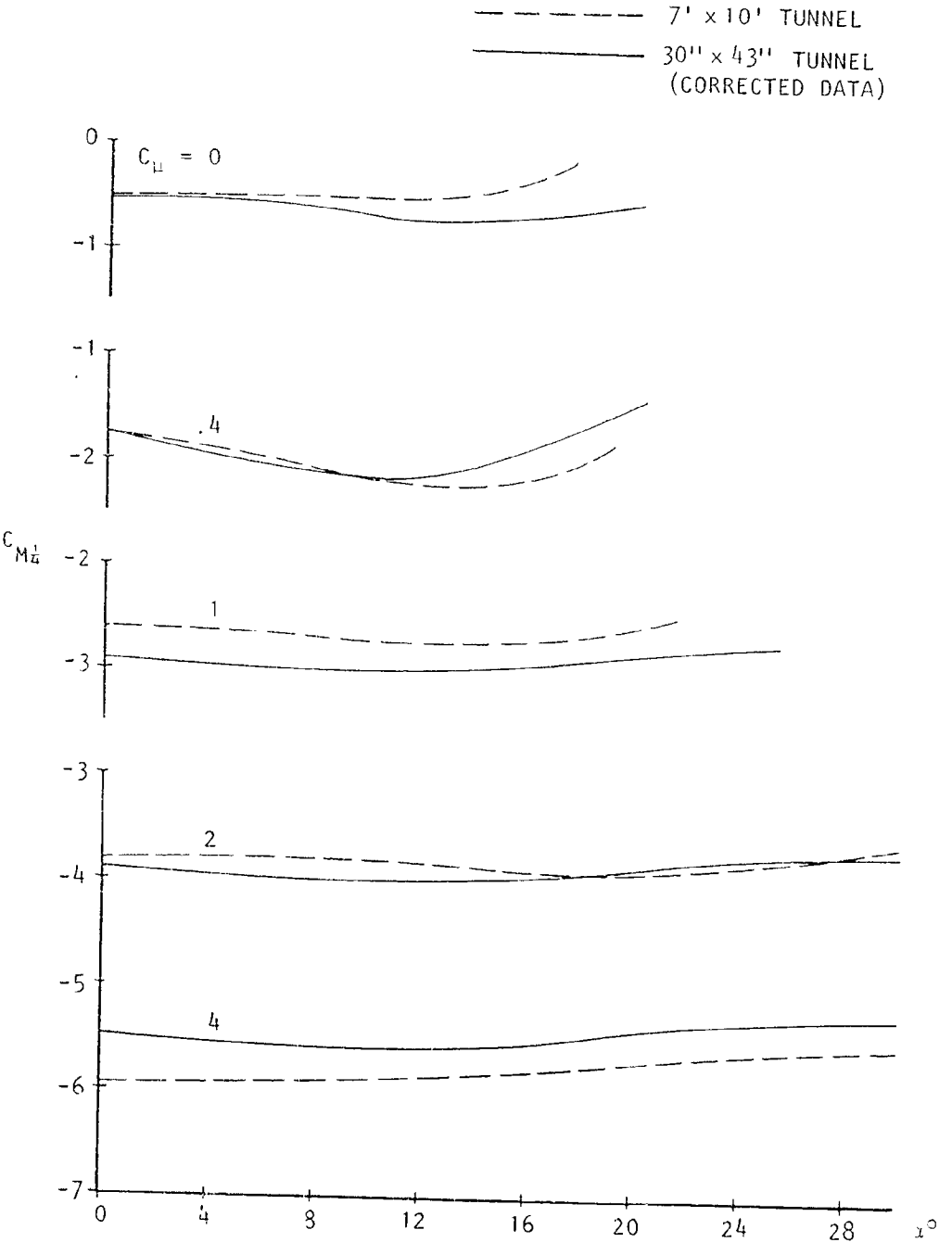

Figure 8.10 Large tunnel and corrected small tunnel pitching moments for knee-blown flap model.

APPENDIX I

PROGRAM DESCRIPTION

APPENDIX I

PROGRAM DESCRIPTION

The blockage program was initially developed for the Lockheed 16¼' x 23¼' low speed wind tunnel using, initially, its CDC 1700 computer and later its TI 990 system. Complex pressure signatures, arising from powered model testing, in the Lockheed 30" x 43" tunnel led to further refining of the program, using that facility's Lockheed MAC-16 computer. The program has been further tidied up for implementation on the NASA CDC 7600 system.

This appendix gives an overview of the program together with the input and output information needed for its use. No reference to the main text of this report should be needed in order to run the program. Listings of the program are given in Appendices II and III, and the required working charts may be found in Appendices IV and V. The information available on the 7600 consists of the program itself and three data packages (working charts for the appropriate tunnel configurations). This information is stored under the identification CORSIGLIA and the following names:

NAS2-9883A	Program and library.
NAS2-9883B	Charts for .699 aspect ratio rectangular tunnel.
NAS2-9883C	Charts for 40' x 80' center tunnel mount.
NAS2-9883D	Charts for 40' x 80' semispan floor mount.

General Structure. - The general structure of the computer program is shown in Figure A1*. A listing is given in Appendix II. The program can be conveniently considered in three parts: input, computation and output. A fourth part, not shown, is the library. This consists of miscellaneous routines, some of which are standard systems library features on the 7600. They were required for the Lockheed mini-computer, and have been retained in anticipation of the program eventually being transferred back to a mini-computer. A listing of these routines is given in Appendix III.

---

* Page 117

Basically, the program accepts the tunnel wall pressure signature and subtracts from it the empty tunnel signature, leaving the signature due to the presence of the model. This signature, defined by a pressure coefficient distribution, is converted to a velocity increment distribution.

The velocity distribution is split into a symmetric and an anti-symmetric component. The source-sink pair that would produce the symmetric component and the source that would produce the antisymmetric component, are derived from the included working charts. It is then possible to calculate the velocity distribution, along the tunnel centerline, that results from tunnel effects stemming from this source and source-sink pair combination. The resulting blockage parameters are displayed.

The velocity distribution along the tunnel wall, also calculated from the combination, is displayed graphically, on the line printer, together with the test data to show the degree to which the program is matching the test data.

Two additional, optional, printouts are available. The first is output from within the computational portion of the program to facilitate debugging. This may also provide a better understanding of the program's attempts to handle a non-standard velocity signature. The second option is a breakdown of the the components that make up the wall and center tunnel velocity distributions.

Input. - The required input to the program can be considered in three parts. These are, initially the working charts, secondly the main input and finally the run input.

The input format for the working charts can be seen in the program listing (Appendix II) in the subroutine EPSTAB. The data blocks provided (named in the beginning of the appendix) are complete and in the necessary format for immediate insertion into the program.

Subsequent input is shown in the program listing in the subroutine EPSINP.

Main Input

The main input portion of this consists of the following cards:

(1) IPR ITEST 215

IPR - Output device number (line printer)
ITEST - Test number.

(2) ATUN BTUN 2F8

ATUN - Tunnel cross-sectional area (ft^2)
BTUN - Tunnel reference width (ft)

For the Ames 40' x 30' tunnel, BTUN = 80 and ATUN = 2857 for center tunnel tests and ATUN = 5713 for floor-mounted half models.

(3) TITLE 20A4

TITLE - Test description

(4) BMOD BFAC XMOD 3F8

BMOD - Model span (ft)
BFAC - Ratio of source length to model span (assume 1.0)
XMOD - Axial position of model (ft)

(5) NWST 15

NWST - Number of pressure readings (maximum = 21)

(6) XWST(1) XWST(2) XWST(NWST) 10F8

XWST - Array of pressure tap axial positions (ft)

(7)

CPEM(1)	CPEM(2)		CPEM(NWST)

10F8

CPEM - Array of empty tunnel pressure coefficients.

(8)

XMC	XMA	VOLM	SF	AR	DELTA

6F8

XMF - Forward extremity of model location (ft)
XMA - Aft extremity of model location (ft)
VOLM - Model volume (cu. ft)
SF - Wing area (sq. ft)
AR - aspect ratio
DELTA- interference factor
} for incidence corrections

The interference factor (δ) is that obtained from Pope (ref. 7).

(9)

LU	IUSES	IUSEE	ILIST	IDEBUG	ITAB

615

LU - Plotter device number (LU=0)
IUSES - Forward asymptote identification
IUSEE - Aft asymptote identification
ILIST - Additional output option (ILIST≠0)
IDEBUG - Debugging output option (IDEBUG≠0)
ITAB - Working charts output option (ITAB≠0)

The testing of floor-mounted models requires that the image system (the floor being the axis of symmetry) be recognized. Tunnel area, reference width, model geometry and interference factor should include this image.

Run Input

(1)

--	ALPHA

F8, F6

ALPHA - Angle of attack (degrees).

(2) | CPWST(1) | CPWST(2) | ... | CPWST(NWST) | 10F8

CPWST - Array of pressure coefficients

(3) | QU | PU | 2F8

QU - Uncorrected tunnel dynamic pressure (psf)

PU - Uncorrected tunnel static pressure (psfa)

(4) | CODE | CMUU | CLU | CDU | CMU | 5F8

CODE - (Run number) + (Point number) /100

CMUU - Uncorrected power coefficient

CLU - Uncorrected lift coefficient

CDU - Uncorrected drag coefficient

CMU - Uncorrected pitching moment coefficient

(5) | IOPT | I5

IOPT - Next input option (-1 Terminate, 0 New run input, 1 New main input)

A sample input is shown in Table 1.*

Computation. - An outline of the computation procedure is shown in Figure A2. Practical and theoretical considerations of the measured velocity distribution show that a similar distribution can be obtained from a distribution of line sinks and sources along the centerline of the tunnel. The purpose of this section is to determine the source and source-sink pair that would generate a signature matching that measured. The effect of the source and of the source-sink pair is to generate two velocity distributions which are respectively antisymmetric and symmetric about a plane in the approximate vicinity of the model.

* Page 119

The amplitude of the antisymmetric portion (UOUMIN) is determined from the forward and trailing asymptotes of the measured velocity distribution (UOU). The axis of antisymmetry (XVOB) is initially assumed to be at the model position (XMOB) and the distribution determined (UAOU). Subtraction of the distribution from the test data leaves the symmetric component (USOU).

A parabola is fitted to the upper portion of the symmetric data, using a least squares fit routine, and the axis of symmetry (XPOB) determined. If this is appreciably different from the assumed position (XVOB), the antisymmetric distribution is recalculated at the new position, and the above process repeated.

The source (QFW) that would generate the antisymmetric distribution, is directly proportional to the amplitude of this distribution and is positioned at the axis of antisymmetry. The source-sink pair, strength (QFS) and spacing (CSOB), are determined from the working (or look-up) charts and are a function of the amplitude of the symmetric distribution (UOUMAX) and the width of the distribution at the half-amplitude height (DXOB).

This information is now sufficient to calculate the theoretical distribution of velocity at the wall (UOUW) and along the tunnel centerline (SIGUOU). Not shown on the flow chart of Figure A2 is a check on the validity of the assumed asymptotes. If conditions are not asymptotic at the selected forward and aft data points (determined by IUSES and IUSEE), then the calculated curve (UOUW) will not pass through these selected data points. This is checked at the end of the first pass through the calculation and the asymptotes modified by the amount of miss.

Provision is made for the program to bypass the source-sink estimation, in the event that it is unable to adequately curve fit the USOU data, and proceed to a subroutine named PUNT. In this case the blockage, at the model position, is estimated directly using a version of Hensel's method (ref. 9) and no distributions are available.

Additional information on the program is available in the form of comments on the listing in Appendix II.

Debug Output. - The setting of IDEBUG≠0 will result in output similar to that shown in Table 2. The first line (U/U) is the test data. The curve extremities are to be defined by the first point (IUSES=1) and the third from last point (IUSEE=-3).

The next six lines represent one pass through the iteration loop. A5-7 represents the three coefficients of the antisymmetric curve A5, A6 and A7. UA/U and US/U are the antisymmetric distribution and the residue (U/U - UA/U). The next line, labelled XV/B gives in turn, the assumed axis of antisymmetry (XVOB), the coefficients A5, A6 and A7, the coefficients of the parabola A, B and C, the amplitude of the symmetric curve (UOUMAX), the width at the half-amplitude (DXOB) and the location of the axis of symmetry (XPOB).

At the conclusion of the first pass through the iteration loop, the program bypasses the iteration check and calculates the total wall distribution (UOUW) and checks the validity of the selected asymptotes. The iteration output is repeated. Note that the forward asymptote (point 1 in the UA/U data) has been decreased by .0006 and the aft asymptote by .0001. The axis of antisymmetry and symmetry was initially assumed zero and calculated to be -.0327. On the second pass an assumption of -.0327 gave an answer of -.0351 which is within the required limits and the iteration terminated.

The next line of data, labelled BS/B, gives the inputs to the working plots, BSOB and DXOB together with the results from Chart I and Chart II. The final line of data, labelled XM/B, gives the extremities of the model (inputs), and the velocities at these points, and finally the buoyancy factor (DCPDX).

Normal Output. - An example of normal output is shown in the upper half of Table 3. The symbols on the plot are 'O' for the test data and 'X' for the matching calculated distribution The supplied coefficients are shown as

measured, with blockage corrections and with incidence corrections per Pope (ref. 7).

The following data consists of the blockages (EPS) at the model position [X(MOD)/B] and at the position of maximum blockage [X(MAX)/B], the source-sink strength (QS/UBM) and the single source strength (QW/UBH). The model span (BS/B) and the width at half-amplitude of the symmetric velocity distribution (XV/B) provide the inputs for the working charts, giving the source-sink spacing (CS/B) and the source-sink strength term (UFM). US(MAX)/U is the amplitude of the symmetric curve. A5, A6 and A7 are the coefficients of the antisymmetric curve and DCDWB is the buoyancy factor.

The comment on the final line indicates the status during the iteration loop where divergent conditions or a jump to a Hensel computation (subroutine PUNT) may have been experienced.

Additional Output. - The lower half of Table 3 shows the additional output that is optionally available. It consists of the pressure point locations (X/B), the test pressure coefficients (CP) and the resulting velocity distribution (U/U). The antisymmetric component (UA/U), the residue (US/U) and the calculated wall distribution (UOUW) follow. The final three sets of data are the center-tunnel build-up of the potential blockage, viscous blockage and total blockage.

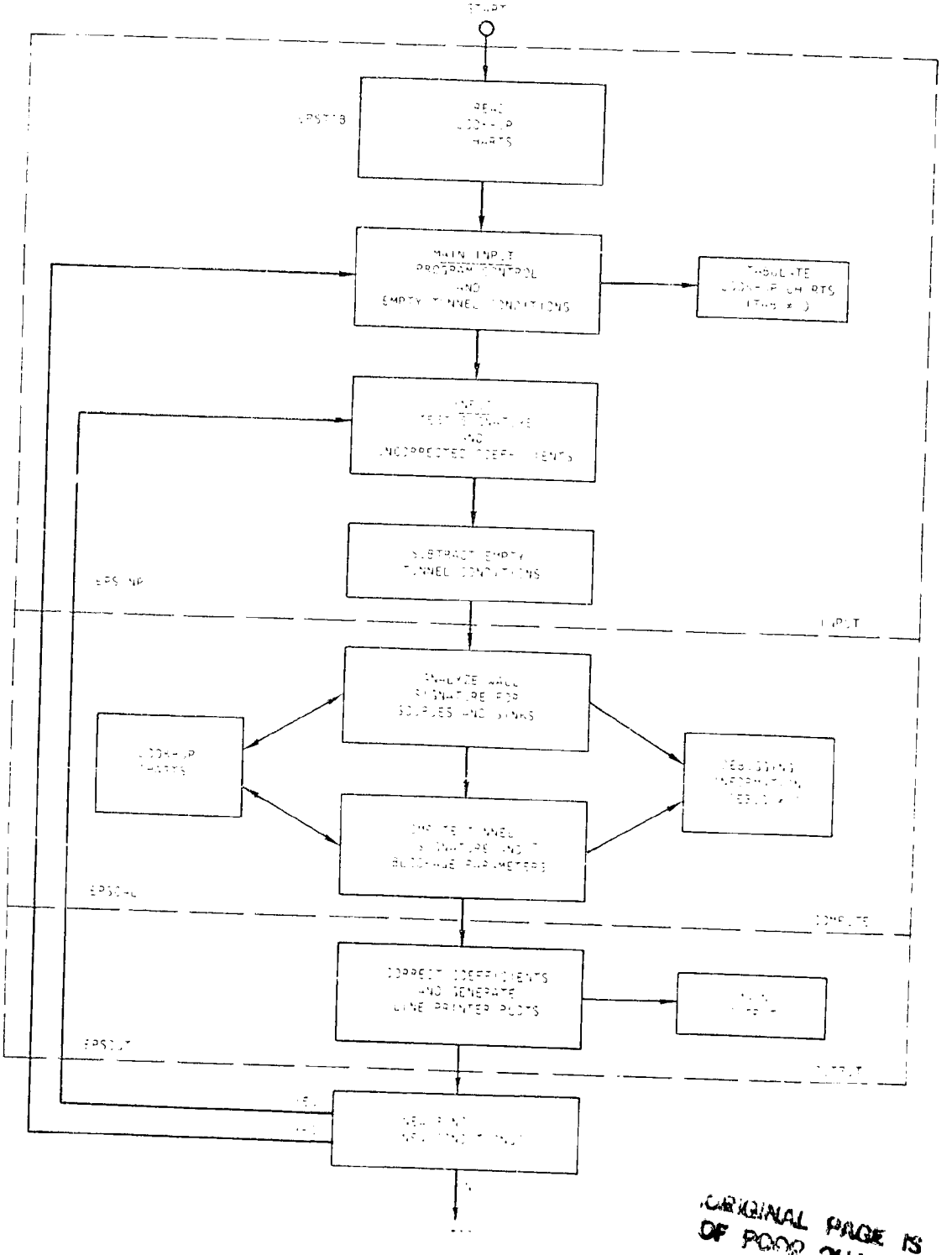

Figure A1 General structure of computer program.

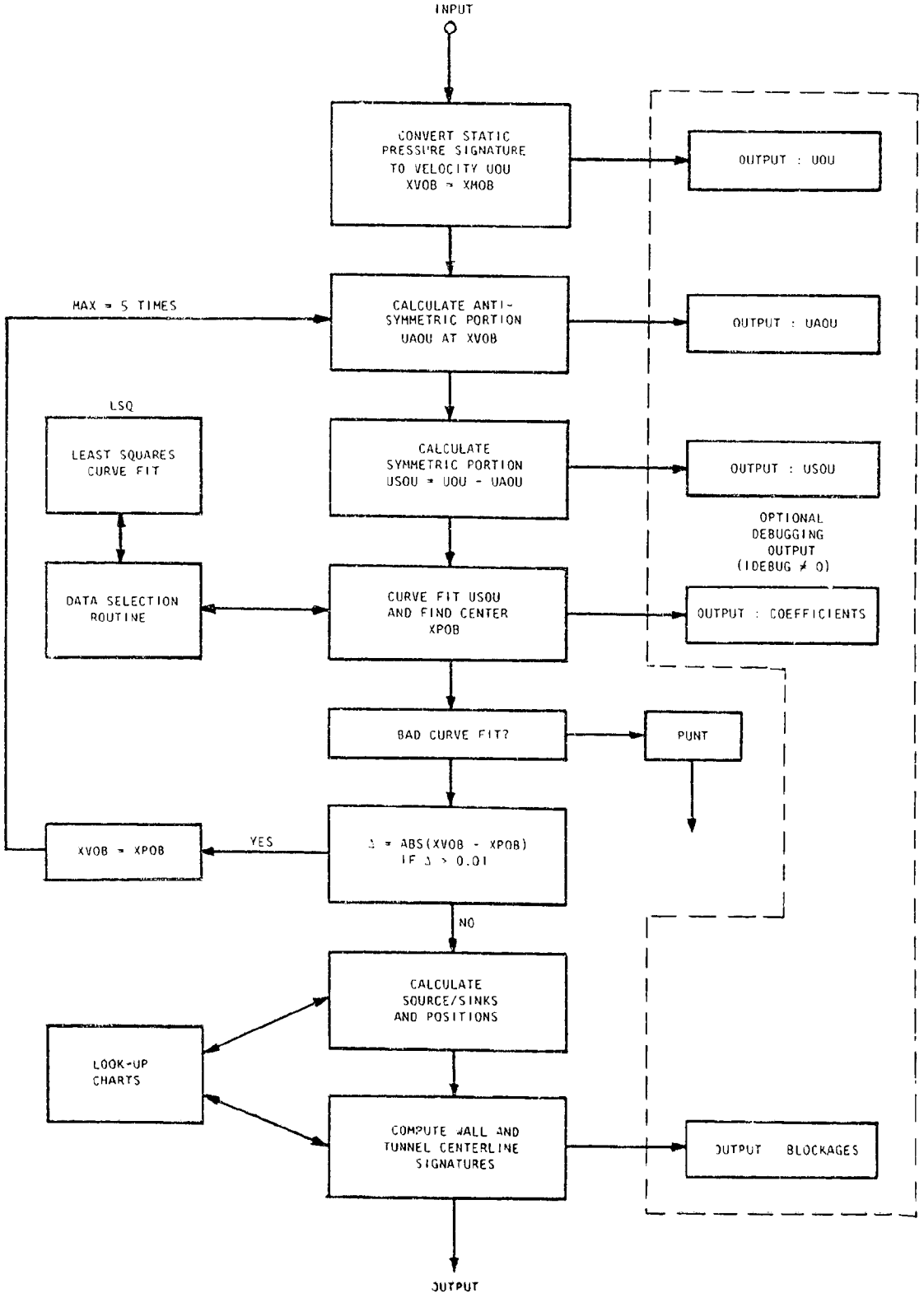

Figure A2 Outline of computational procedure.

```
     0    .27
    43.0     30.0
KBF - STRAIGHT WING - (MLI)
   20.00     1.00      .00     1.00      .00
    21     0
  -35.00   -20.00   -16.00   -12.00    -8.00    -4.00      .00     3.00     6.00     9.00
   12.00    15.00    18.00    21.00    25.20    30.00    36.00    42.00    48.00    54.00
   60.00
  -.0593   -.0338   -.0097   -.0149   -.0143   -.0210   -.0225   -.0189   -.0291   -.0261
  -.0384   -.0391   -.0498   -.0411   -.0434   -.0365   -.0580   -.0723   -.0716   -.0929
  -.0569
    -.47    12.53   100.61    80.00     5.014     .14
     0     1    -1     1     1     1
 ALPHA =   7.78
 -0.0811 -0.0371 -0.0144 -0.0217 -0.0289 -0.0414 -0.0519 -0.0648 -0.0744 -0.0759
 -0.0793 -0.0829 -0.0927 -0.0753 -0.0781 -0.0774 -0.0941 -0.1011 -0.1001 -0.0971
 -0.0946
    4.78 2037.99
  144.07   0.0000   1.0999   0.7323  -0.7844
   -1
```

Table 1 Sample program input.


```
DEBUGGING INFORMATION

  C/L   -.0091    .0016    .0023    .0034    .0073    .0101    .0146    .0226    .0224    .0246    .0202    .0217    .0212    .0189    .0162
         .0202    .0179    .0143    .0141    .0021    .0189

  AS-1   .0117   4.2365   0.0000
  CA/U  -.0091   -.0087   -.0082   -.0071   -.0051   -.0016    .0026    .0059    .0088    .0109    .0123    .0131    .0136    .0139    .0141
         .0142    .0143    .0143    .0143    .0143    .0143
  CS/U  -.0000    .0103    .0105    .0105    .0124    .0120    .0120    .0167    .0136    .0137    .0080    .0085    .0076    .0050    .0021
         .0060    .0036    .0000   -.0001   -.0122    .0046
  XV/B  0.0000    .0117   4.2365   0.0000   -.0228   -.0009    .0135    .0136    .5714   -.0196
  BS/B   .4651    .4500    .8668   1.3577

  AS-1   .0119   4.2365   0.0000
  CA/U  -.0097   -.0093   -.0087   -.0077   -.0056   -.0023    .0022    .0057    .0086    .0107    .0121    .0130    .0135    .0138    .0140
         .0141    .0141    .0142    .0142    .0142    .0142
  CS/U   .0005    .0109    .0111    .0111    .0129    .0124    .0124    .0169    .0138    .0139    .0081    .0087    .0077    .0051    .0022
         .0061    .0037    .0001   -.0000   -.0121    .0048
  XV/B  0.0000    .0119   4.2365   0.0000   -.0230   -.0015    .0138    .0140    .5764   -.0327

  AS-1   .0119   4.2365    .1383
  CA/U  -.0097   -.0091   -.0084   -.0071   -.0046   -.0008    .0039    .0071    .0097    .0114    .0126    .0133    .0137    .0139    .0140
         .0141    .0141    .0142    .0142    .0142    .0142
  CS/U   .0005    .0108    .0108    .0105    .0119    .0109    .0107    .0155    .0127    .0132    .0077    .0084    .0076    .0050    .0022
         .0061    .0037    .0001   -.0000   -.0121    .0048
  XV/B  -.0327    .0119   4.2365    .1383   -.0152   -.0011    .0125    .0126    .6725   -.0351
  BS/B   .4651    .4500    .8668   1.3577
  XM/B  -.0108    .2987   1.0111   1.0152   -.0006
```

Table 2 Sample debugging output.

TEST 27 RUN 149 POINT 7

KBE - STRAIGHT WING - (R1)

	ALPHA	CL	PL	CL	CD	CM	CMU
MEASURED	7.78	4.78	2037.94	1.9939	.7323	-.7944	0.0000
BLOCKAGE	7.78	4.93	2037.79	1.9336	.7110	-.7704	0.0000
INCIDENCE	8.57	4.93	2037.79	1.9236	.7376	-.7704	0.0000

EPS(MOD) = .0113 X(MLC)/B = 0.000 BS/B = .465 QS/QBM = .01333

EPS(MAX) = .0155 X(MAX)/B = .404 QX/B = .450 QX/QBM = .02388

M FACTOR = .6658 XV/B = -.033 QS/B = .867 A5 = .01194

DCDMB = -.0009 DS(MAX)/B= .013 QBM = 1.358 A6 = 4.23650

NORMAL COMPUTATION A7 = .13834

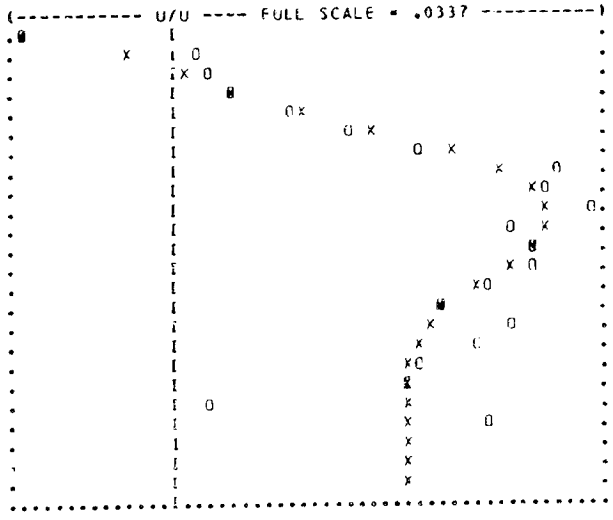

WALL/CEILING PRESSURE BLOCKAGE COMPUTION

X/B	-.8140	-.4651	-.3721	-.2791	-.1860	-.0930	0.0000	.0698	.1395	.2093	.2791	.3488	.4186	.4884	.5874
	.6977	.8372	.9767	1.1163	1.2558	1.3953									
CP	.0182	-.0055	-.0047	-.0068	-.0146	-.0204	-.0294	-.0457	-.0453	-.0498	-.0409	-.0438	-.0429	-.0382	-.0327
	-.0409	-.0361	-.0288	-.0285	-.0042	-.0382									
U/U	-.0091	.0016	.0023	.0034	.0073	.0101	.0146	.0226	.0224	.0246	.0202	.0217	.0212	.0189	.0162
	.0202	.0179	.0143	.0141	.0021	.0189									
UA/U	-.0097	-.0091	-.0085	-.0071	-.0046	-.0008	.0039	.0071	.0097	.0114	.0126	.0133	.0137	.0139	.0140
	.0141	.0141	.0142	.0142	.0142	.0142									
V/U	.0005	.0100	.0108	.0105	.0119	.0109	.0107	.0155	.0127	.0132	.0077	.0084	.0076	.0050	.0022
	.0061	.0037	.0001	-.0000	-.0121	.0048									
UA/U	-.0090	-.0024	.0007	.0039	.0075	.0118	.0165	.0195	.0216	.0225	.0224	.0213	.0198	.0182	.0163
	.0151	.0145	.0143	.0142	.0142	.0142									
UI/U	.0025	.0058	.0087	.0075	.0080	.0084	.0084	.0083	.0079	.0076	.0069	.0063	.0055	.0048	.0038
	.0028	.0020	.0014	.0010	.0008	.0007									
UV/	-.0078	-.0053	-.0042	-.0028	-.0010	.0009	.0029	.0044	.0058	.0071	.0082	.0091	.0099	.0106	.0113
	.0120	.0124	.0127	.0130	.0133	.0136									
EPS	-.0052	.0064	.0025	.0047	.0070	.0092	.0113	.0127	.0137	.0146	.0151	.0154	.0155	.0154	.0151
	.0149	.0145	.0141	.0141	.0141	.0142									

Table 3 Sample program output.

APPENDIX II

PROGRAM LISTING: AERODYNAMIC ROUTINES

```
      C --- BATCH DRIVER FOR BLOKE-SYSTEM WALL-PRESSURES BLOCKAGE CALCULATION
      C --- AMES CDC 7600 VERSION - D.E.LITTLEY - 1/11/79
      C ---
            PROGRAM MAIN(INPUT,OUTPUT,TAPE5=INPUT,TAPE6=OUTPUT)
            [illegible]
      C ---
      C --- INPUT LOOK-UP CHARTS
            CALL EPSTAB(C)
      C ---
      C --- INPUT DATA
            IS=1
         1  CALL EPSINP(IS,IPR,IUSES,IUSEE,IDEBUG,ILIST,LL,
           *            D1,D2,ALPHA,QU,PU,CMUL,CLL,CDL,CMU)
      C ---
      C --- CALCULATE BLOCKAGE
         2  CALL EPSCAL(IUSES,IUSEE,IDEBUG,IPR)
      C ---
      C --- TABULATED (LINE-PRINTER) OUTPUT
            CALL EPSOUT(IPR,ILIST,D1,D2,ALPHA,QU,PU,CMUL,CLL,CDU,CMU)
      C ---
      C --- GRAPHICS/PLOTTER DEVICES
            IF(LL.EQ.0) GO TO 1
            CALL EPSPLT(CLL)
            GO TO 1
            END
```

MAIN PROGRAM FOR THE COMPUTATION OF THE CORRECTE[illegible] TUNNEL CENTERLINE VELOCITY DISTRIBUTION FROM A SET OF STATIC PRESSURE TAPPINGS SET IN A WALL PARALLEL TO THE DIRECTION OF LIFT OF THE MODEL.

```
      SUBROUTINE INPSIN(IES,IPR,IUSES,IUSEE,IELOOG,IELIST,EG,
     *                  D1,D2,ALPHA,GG,PO,CMUG,CEG,CGG,CMU)
      COMMON IELIST IRUN,IPT,NMST,
     *       EPSM(6),XM0%,X%(9),U%M1(14),XMFUP,XMAUP,ATUS,ITUS,
     *       VELM,SF,XMST(21),CPMST(21),DUM2(147),CCEFF(3),TITLE(20)
      DIMENSION CPEM(21),DUM(21)
C ---
      IF(IS.EQ.1) GO TO 2
C ---
    1 READ(5,10) IOPT
      IF(IOPT) 7,4,2
C ---
    2 READ(5,10) IPR,IELIST
      READ(5,11)
      READ(5,12) (TITLE(I),I=1,20)
      READ(5,11) EMEE,BPAC,XMGO
      READ(5,10) NMST
      READ(5,11) (XMST(I),I=1,NMST)
      READ(5,11) (CPEM(I),I=1,NMST)
      READ(5,11) XMF,XMA,VOL%,SF,AR,DELTA
      READ(5,10) EG,IUSE5,IUSEE,IELIST,IELEDUG,ITAP
      IS=2
      IF(ITAP.NE.5) CALL OPSTAP(IPR)
      GO TO 1
    3 XM2(I)=XM2(I)/XTON
      SL=DELTA*XF/ 
      GG=2(.,1415926*AR)
C ---
    4 READ(5,11) ALPHA
      READ(5,11) (CPMST(I),I=1,NMST)
    5 READ(5,11) GG,PO
      READ(5,11) CGEE,CMUG,CLG,CGG,CML
C ---
      CALP=COS(ALPHA/57.3)
      XMF=XMF0L/BTON
      BSC=XMGG*PPAC/BTON
      XMEE=XMEE*CALP/BTON
      XMAC=XMA*CALP/BTON
      IRUN=IFIX(CLEE)
      IPT=IFIX(CGEE*100.+.01)-IRUN*100
      DO 6 I=1,NMST
    6 CPM2(I)=CPMST(I)-CPEM(I)
      RETURN
C ---
    7 STOP
C ---
   10 FORMAT(I5)
   11 FORMAT(6F10.0)
   12 FORMAT(20A4)
   13 FORMAT(A4,F5.2)
      END
```

SUBROUTINE READS IN THE INPUT.

MAIN INPUT S[illegible] IN[illegible] FOR [illegible] AN[illegible]
THE STATIC PR[illegible] REQUIRED [illegible] AN[illegible]
TUNNEL PR[illegible] SEQUENCES.

INPUT F[illegible] CASE INDIVIDUAL [illegible]
STATIC PRESSURE SIGNATURES, [illegible]
THE CHECKPOINTED AERO VARIA[illegible].

```
      SUBROUTINE EPSTAB (IWR)
      COMMON ZOM(6,15),N1,N2,N3,P(10),C(10),R(10,10),S(10,10),
     1  T(10),U(10)
      DIMENSION TITLE(20)
C ---
      IF(IWR.NE.0) GO TO 1
      READ(5,6) N1,N2,N3
      READ(5,7) TITLE
      READ(5,8) (P(J),J=1,N1)
    1 READ(5,8) (C(I),I=1,N2)
      DO 2 I=1,N2
    2 READ(5,8) (R(I,J),J=1,N1)
      DO 3 I=1,N2
    3 READ(5,8) (S(I,J),J=1,N1)
      READ(5,8) (T(I),I=1,N3)
      READ(5,8) (U(I),I=1,N3)
      DO 4 I=1,6
      RETURN
C ---
    4 WRITE(IWR,12) TITLE
      WRITE(IWR,13) (P(J),J=1,N1)
      WRITE(IWR,11)
      DO 5 I=1,N2
    5 WRITE(IWR,14) C(I),(R(I,J),J=1,N1)
      WRITE(IWR,15)
      WRITE(IWR,13) (P(J),J=1,N1)
      WRITE(IWR,11)
      DO 6 I=1,N2
    6 WRITE(IWR,14) C(I),(S(I,J),J=1,N1)
      WRITE(IWR,17)
      WRITE(IWR,11)
      WRITE(IWR,16) (T(I),I=1,N3)
      WRITE(IWR,11)
      WRITE(IWR,16) (U(I),I=1,N3)
      DO 7 I=1,6
      RETURN
C ---
    6 FORMAT(3I4)
    7 FORMAT(20A4)
    8 FORMAT(10F8.6)
   11 FORMAT(1H )
   12 FORMAT(1H1///5X,20A4//5X,21H** CS/B TABLE (XCSB))
   13 FORMAT(1HC,14X,4HB/B//5X,4HR/C/8,3X,10F7.3)
   14 FORMAT(4X,F5.3,3X,10F7.3)
   15 FORMAT(1HO/5X,31H** (U/(CS/B**2))MAX TABLE (XUB))
   17 FORMAT(1HO/5X,25H** U/(CS/B**2) TABLE (XUB))
   16 FORMAT(1H ,5X,5HX/B  ,1X,10F7.3/12X,10F7.3)
   18 FORMAT(1H ,5X,5HXUB  ,1X,10F7.4/12X,10F7.4)
      END
```

```
      SUBROUTINE EPSCAL(IUSES,IUSEE,IDEBUG,IPR)
      COMMON ITEST,IRUN,IPT,NMST,
     *       EPSMCL,XMOB,BSOU,QFS,EPSMAX,XP,CXCB,QFM,HENSEL,XVOB,
     *       CSOBI,AS,QCOR,UCUMAX,UFMAX,AG,AZ,XMFCB,XMACB,ATLN,
     *       BTLN,VELM,SF,XMST(21),CPMST(21),CDU(21),UAOU(21),USOU(21),
     *      UOUR(21),UOUP(21),UOUV(21),SIGUEC(21),A,B,C,
     *       TITLE(20),NBS,NDX,NX,XBSOB(10),XOXCB(10),CSOB(10,10),
     *       XUFM(10,10),XXOB(20),XLF(20),XC(1),XF(1)
      DIMENSION TIT(2)
      DATA TIT/4HEC/L ,4HUA/O,4HUS/O,4HXV/B,4HBS/B,4HXM/B/
C ---

C --- CONVERT CP TO C/UO AND FIND END ASYMPTOTE
C ---
      IF(IDEBUG.EQ.0) GO TO 1
      WRITE(IPR,101)
    1 DO 2 I=1,NMST
    2 UOU(I)=SQRT(1.-CPMST(I))-1.
      UOUAS=0.
      IF(IUSES.NE.0) UOUAS=UOU(IUSES)
      XVO =XMOB
C ---

C --- ANTI-SYM ART ASYMPTOTE AND COEFFICIENTS
C ---
      NCC=0
      III=0
      WRITE(IPR,100) TIT(1),(UOU(I),I=1,NMST)
      IF(IUSEE.GT.0) GO TO 5
      NMST=NMST+IUSEE
    4 UOUMIN=UOU(NMST)-UOUAS
      UU=0.0259*ABS(UOUMIN)
      IF((UOU(NMST)-UOU(NMST-1)).LT.UU) GO TO 8
      NMST=NMST-1
      GO TO 4
    5 UOUMIN=0.
      DO 6 I=1,IUSEE
      K=NMST-I+1
    6 UOUMIN=UOUMIN+UOU(K)
      UOUMIN=UOUMIN/IUSEE-UOUAS
      NMST=NMST-IUSEE/2
      GO TO 8
    7 DI=0.
      III=1
      IF(IUSES.GT.0) DI=UOUMI(IUSES)-UOUAS
      D2=UOUMIN*UOUAS-UOUM(NMST)
      UOUAS=UOUAS-DI
      UOUMIN=UOUMIN+DI+D2
    8 AS=0.5*UOUMIN
      AG IS [illegible]
C ---
```

SUBROUTINE FOR COMPUTING THE TUNNEL CENTERLINE BLOCKAGE PARAMETERS. INFORMATION FOR DEBUGGING THE PROGRAM, OR UNDERSTANDING PROBLEM SIGNATURES, CAN BE OBTAINED BY MAKING IDEBUG=1 IN THE MAIN INPUT.

CONVERSION OF THE PRESSURE DISTRIBUTION (CPMST) TO A VELOCITY DISTRIBUTION (UOU), AND DETERMINATION OF THE TRAILING ASYMPTOTE (UOUAS) WHICH IS ASSUMED TO BE ZERO (FOR IUSES=0), OR POINT NUMBER IUSES (FOR IUSES NOT ZERO).

THE TRAILING ASYMPTOTE (UOUMIN) IS DETERMINED BY AVERAGING THE LAST IUSES DATA POINTS (FOR POSITIVE IUSES), OR BY USING THE LAST IUSEE DATA POINT (FOR NEGATIVE IUSES).

IN THE LATTER CASE THE SELECTED DATA POINT IS CHECKED TO SEE IF IT IS PART OF A SEVERE PEAK IN THE DATA, IN WHICH EVENT, SUCCESSIVELY MORE FAR POINTS ARE SELECTED UNTIL THE TROUGH IS LOCATED.

THE COEFFICIENTS OF THE ANTI-SYMMETRIC PORTION, AS AND AG, ARE THEN DETERMINED.

```
C --- GENERATE ANTI-SYM PORTION, SUBTRACT AND CURVE-FIT RESIDUE
C ---
    9 A7 C.-4*C0*P2G
      DO 11 I=1,NMST
      AA=A0*AA5(I)+A7
      DACC(I)=A5*CC.*TANH(AA)+CDCAS
   10 DSUB(I)=DCC(I)-DACC(I)
      IF(I.EQ.DBG.EC.C) GO TO 11
      WRITE(IPR,1C2) A5,A6,A7
      WRITE(IPR,1CC) TIT(2),(DACC(I),I=1,NMST)
      WRITE(IPR,1C0) TIT(3),(DSUB(I),I=1,NMST)
   11 I=NMST
      CALL CFSFIT (XFST,DSUB,1,A,B,C,DDUMAX,XP08,DXDP)
      IF(I.EQ.DBG.EC.C) GO TO 12
      WRITE(IPR,1CC) TIT(4),XV08,A5,A6,A7,A,B,C,DDUMAX,DXD8,XP08
   12 IF(DXDP.GT.C.45) DX08=0.45
      IF(DXDP.GT..0) GO TO 13
      CALL PONT
      RETURN
C ---

C --- EXAMINE ITERATION CONVERGENCE
C ---
   13 DELP=XP08-XV08
      ADELP=ABS(DELP)
      IF(ADELP.LT.C.CL) GO TO 19
      IF(ITIM+1)/3-1) 14,15,19
   14 DELX=XP08-XV08
      XVDP=XP08
      ITIM=ITIM+1
      GO TO 9
   15 IF(DELX/DELP) 16,19,17
   16 IF(NCC.EQ.1) XP08=(XP08+XV08)/2.
      NCC=1
      IF(ADELP-2.*ABS(DELX)) 14,18,18
   17 IF(ADELP-   ABS(DELX)) 14,18,18
    1 XV08=XP08
      ITIM=0
      GO TO 9
   19 CONTINUE
C ---

C --- INTERPOLATE TABLES TO DETERMINE CS/B AND DE(MAX)
C ---
   20 CSUB1=DTAB2(BSDB,DX08,XBSDB,XDXDP,NBS,NDX,2,2,CSUB,10,IERR)
      IF(CSUB1.GT..C5) GO TO 21
      CSUB1=0.05
   21 DEMAX=DTAB2(BSDB,DX08,XPSDB,XDXDB,NBS,NDX,2,2,XDEM,10,IERR)
      IF(DEMAX.GT..1) GO TO 22
      DEMAX=.1
C ---
C --- COMPUTE (SOLID+BUBBLE) AND (VISCOUS) SOURCE STRENGTHS Q/(UBB)
C ---
   22 DFS=DDUMAX/DEMAX
      GEM=2.*A59.(EP/ TO 2 )
      IF(IDEBUG.EC.C) GO TO 23
      WRITE(IPR,1CC) TIT(5),BSDB,DXDB,CSUB1,DEMAX
```

126

START OF ITERATION LOOP [illegible] AND WAKE/SINK LOCATIONS.

THE SOURCES CONTRIBUTING THE ANTI-SYMM PORTION IS INITIALLY ASSUMED TO BE AT THE [illegible] (XVDB=XMOST). THE RESULTING ANTI-SYMM TAIL [illegible] IS SUBTRACTED FROM THE TEST DATA (DSUB) TO GIVE THE RESIDUE (DSUB).

THE RESIDUE IS THEN INTO A CURVE FIT ROUTINE (CFSFIT) THAT RETURNS THE COEFFICIENTS OF A [illegible] UNDER POLYNOMIAL, AND THE POSITION OF THE AXIS OF SYMMETRY (XP08). IF AN UPSTREAM MAXIMUM IS [illegible] THE PROGRAM EXITS TO THE SO-CALLED PONT.

THE RESULTING POSITION (XP08) IS CHECKED AGAINST THE ASSUMED POSITION (XVDB), USING SUCCESSIVE ITERATIONS, FOR CONVERGENCE. IF DIVERGENCE CONDITIONS ARE FOUND, THE INITIAL POSITION IS ASSUMED AND THE [illegible] REPEATED AT THIS NEW POSITION.

THE BARE BUBBLE SOURCE [illegible] THE [illegible] BUBBLE/SINK RATIO [illegible] DETERMINED FROM THE [illegible].

```
C ---
C --- COMPUTE WALL DISTRIBUTION
C ---
      DO 25 I=1,NMST
         A1=.5*CFS* [illegible]
         A2=[illegible]
         X3=XX(IE-.5*CSCEL
         XM=X(2)-.5*CSCEL
         DO 24 I=1,NMST
         T1=TANH(A2*(XB(I)-X3))
         T2=TANH(A2*(X4-XMST(I)))
   24    UCUM(I)=A1*(T1+T2)*UA3UCE(I)
   25    EFFIEM,EG,E) CO TO 7
C ---


C --- COMPUTE CONTRIBUTIONS TO TUNNEL OF LEAKAGE OF THESE SOURCES
C ---
      DO 25 I=1,NMST
      XX=XMST(I)-XVCB
      UFF=.TABLE(XX,XXOB,XUF,NX,2)
      UCUF(I)=UFF*UFF*USCAS
      XP=XX-CSCEL/2.
      ELF=.TABLE(XP,XXOB,XUF,NX,2)
      XM=XP-CSCEL
      UFF=.TABLE(XM,XXOB,XUF,NX,2)
      UCUF(I)=(ELF-UFM)*UFS
   25 SIGUCUF(I)=UCUM(I)+UOUF(I)
      CFS=CFS*BTUN [illegible]
      UFM=UFM*BTUN [illegible]
C ---


C --- INTERPOLATE FOR BLOCKAGE AT MODEL CENTER AND EXTREMES
C ---
      UFM=.STAB(XMFCB,XMST,SIGUCU,NMST,2) + 1.
      UAFT=.STAB(XMACB,XMST,SIGUCU,NMST,2) + 1.
      EPSMAX=.TAB(XMOB,XMST,SIGUCU,NMST,2)
      XCPSA=(UFM*UUFM-UAFT*UAFT)/(2.*(XMACF-XMFCF)*UFM*UM)
      IF(IUCUCU.EQ.0) GO TO 26
      WRITE(IPR,100) EPSMAX,XMFCB,XMACB,UFM,UM,UAFT,UCPEX
C ---
C --- FIN. PEAK BLOCKAGE
   26 CALL PEAK (SIGUCU,XMST,NMST,EPSMAX,XM)
C ---
C --- FIN. PEAK (SIGUCU**UOBLE) PART BLOCKAGE
      CALL PEAK (UCUF,XMST,NMST,UPMAX,XPM)
      PUMSIG=UPMAX/UUUMSX
      UC.M=UCPEAX*UCUF/SF
      PEF.M
C ---
  100 FI=MATES(,AA,BSF=.N/(FF,ISFF,AI)
  101 I MMATS(OME UEEUUSEMS SMFUPMAF=.N/)
      E C FI=MATE/SA,CFES=/,UFS,N)
      E)
```

For COMPUTES WALL VELOCITY [illegible] set I [illegible] for COMPARISON with [illegible] [illegible] These are the two SUBR [illegible] [illegible] ENTER PLOT.

For TOTAL VELOCITY DISTRIBUTION AL [illegible] CONFIGURE (SIGUCU) IS DETERMIN [illegible] THE SOURCE/SINK PANEL TOGETHER WITH THE [illegible] (OUTERFACE AND WAKE (WHICH [illegible] VELOCITY.

The CORRECTED VELOCITY IS [illegible] AND AFT EXTREMITIES OF THE [illegible] CALCULATED.

```
      SUBROUTINE EPSFIT (XIN,UIN,NIN,A,B,C,UCUMAX,XPOB,DX08)
C ---
C --- PARABOLIC CURVE FIT AND CURVE SHAPE ROUTINE
C ---   CURVE-FIT AND RETURN COEFFICIENTS A,B,C
C ---   AND UCUMAX,XPOB,DX08.
C ---
      DIMENSION XIN(21),UIN(21),XSAV(21),USAV(21)
      DIMENSION CC(3)
C ---


      DX08=-1.
      USM=AMAX1(UIN,NIN,II)
      IF(USM.LE.0.) RETURN
      DO 5 NI=1,4
      UST=USM*(7-NI)/10.
      II=NIN-1
      DO 2 I=1,II
      IL=II-I
      IR=II+I
      IF(UIN(IL).GE.UST) GO TO 1
      IF(IR.GT.NIN) GO TO 3
      IF(UIN(IR).LT.UST) GO TO 3
    1 I=IL
    2 CONTINUE
    3 IE=NIE-I
      IP=1
      DO 4 I=I,IE
      IF(UIN(I).LT.UST) GO TO 4
      IP=IP+1
      USAV(IP)=UIN(I)
      XSAV(IP)=XIN(I)
    4 CONTINUE
C ---


      IF(IP.LT.6) GO TO 5
      CALL LSQUSAV,XSAV,2,IP,CC)
      A=CC(1)
      B=CC(2)
      C=CC(3)
      IF(A.GE.0.) GO TO 5
      XPEAK=-B/(2.*A)
      IF(XPEAK.LT.XSAV(1)) GO TO 5
      IF(XPEAK.GT.XSAV(IP)) GO TO 5
      GO TO 6
    5 CONTINUE
      RETURN
C ---


    6 TEMP=C-B*B/(4.*A)
      DATA=SQRT(-TEMP/(2.*A))*1.05
      UCUMAX=TEMP*1.01
      RETURN
      END
```

SUBROUTINE FOR FITTING A 2ND ORDER POLYNOMIAL TO THE SYMMETRIC PORTION OF THE TEST DATA.

A MAXIMUM VALUE (USM) AND MINIMUM ACCEPTABLE VALUE (UST) ARE DETERMINED. A SELECTION TABLE OF ALL DATA POINTS THAT LIE BETWEEN THESE LIMITS THAT ARE CONSIDERED VALID POINTS.

A 2ND ORDER CURVE FIT IS APPLIED TO THESE DATA POINTS USING A STANDARD LIBRARY LEAST SQUARES FIT ROUTINE (LSQ). IF THE RESULTING POLYNOMIAL IS UNACCEPTABLE, THE MINIMUM ACCEPTABLE VALUE (UST) IS LOWERED, THUS GIVING ADDITIONAL DATA POINTS, AND THE PROCEDURE REPEATED.

THE LOCATION OF THE AXIS OF SYMMETRY, MAXIMUM VALUE AND WIDTH AT HALF-HEIGHT ARE DETERMINED FOR THE RESULTING INVERTED PARABOLA.

```
      SUBROUTINE RENT
      COMMON ITEST,IRUN,IPT,NNST,
     *       EPSMOD,XMOB,BSOB,OFS,EPSMAX,XP,GXOB,GFR,MENSEL,XVOB,
     *       CSLOT,AS,DCOR,UOUMAX,UFMAX,UOM(81),DATA(2L,9),CLEFF(3),
                                                                    .
      DIMENSION USAV(21)
C ---

C --- CHECK FOR MEANINGFUL SOLID BLOCKAGE SIGNATURE
C ---
      UMAX=0.
      SIGG=0.
      SIGABS=0.
      MENSEL=0.
      DO 1 I=1,NNST
      USAV(I)=DATA(I,5)
      SIGG=SIGG+USAV(I)
    1 SIGABS=SIGABS+ABS(USAV(I))
      IF(SIGG.LT.(0.50*SIGABS)) GO TO 4
      MENSEL=
C ---

C --- FIND NEXT GREATEST USOU
C ---
      UMAX=RMAX(USAV,NNST,II)
      IE=NNST-1
      IF(II.LT.II) GO TO 3
      DO 2 I=II,IE
    2 USAV(I)=USAV(I+1)
    3 UMAX=RMAX(USAV,IE,II)
C ---

C --- APPLY MENSEL CORRECTION AND ZEROES
C ---
    4 EPSMAX=MENSEL*UMAX+AS
      EPSMOD=EPSMAX
      OFS=0.
      GFR=0.
      XVOB=0.
      XP=0.
      DXOB=0.
      CSLOT=0.
      DCOR=0.
      UOUMAX=0.
      UFMAX=0.
      DO 5 I=1,3
    5 CLEFF(I)=0.
      DO 6 I=1,NNST
      DO 6 J=1,9
    6 DATA(I,J)=0.
      RETURN
      END
```

SUBROUTINE FOR ESTIMATING THE SOLID BLOCKAGE IN THE ABSENCE OF AN ACCEPTABLE ZNE [illegible] CURVE FIT.

THE VALIDITY OF THE DATA IS DETERMINED BY ENSURING THAT THE DATA IS PREDOMINANTLY POSITIVE.

THE MAXIMUM VALUE IS DISCARDED ON THE ASSUMPTION THAT IT IS IN ERROR, AND PROBABLY THE REASON FOR THE UNACCEPTABLE CURVE FIT.

THE BLOCKAGE IS CALCULATED AT THE MIDDLE STATION, AND ALL NON-RELEVANT PARAMETERS ARE ZEROED.

```
      SUBROUTINE EPSOUT(IPR,ILIST,D1,D2,ALPHA,QQ,PU,CMUU,CLL,CDU,CMU)
C ---
C --- LISTING AND PLOTTING ROUTINE
C --- IPR  =LISTING DEVICE NUMBER
C --- ILIST=0  BRIEF OUTPUT
C ---        1  FULL OUTPUT
C ---
      COMMON ITEST,IRUN,IPT,NMST,DATA2(17),B(6),DATA1(21,9),
     *       COEFF(3),TITLE(20)
      DIMENSION N(25),N1(25),NE(25),M1(2),M2(2),M3(2),M4(2),M5(10)
      DIMENSION TIT(9)
      DATA N/25*2F  /
      DATA NE/25*2H  /
      DATA NE/25*2H../
      DATA M1/2HX ,2F X/
      DATA M2/2HO ,2F O/
      DATA M3/2HI ,2F I/
      DATA M4/2H[ ,2F [/
      DATA IBL,KBL/2F  ,2H  /
      DATA M5/2,6,8,,0,12,16,18,20,22,24/
      DATA IBL,KBL/2F  ,2H  /
      DATA TIT/4HX/E ,4HCP  ,4HCD ,4HCU/U,4HUA/U,4HUS/U,4HUH/U,4HLP/U,
     *     4HUV/U,4HEPS /
      DATA IRUNC/0/
C ---

C --- CORRECTION OF COEFFICIENTS
      EPSMAX=DATA2(5)
      DCDMP=DATA2(13)
      QQ=QQ*(1.+EPSMAX)**2
      PE=PU*QQ-QQ
      CCCDD=QQ/QQ
      CLC=CLC*QQQCC
      CDC=(CDU-DCDMP)*QQQQQ
      CMC=CMC*QQQCC
      CMQC=CMQC*QQCCC
      DALP=(1.+CLC/(1.+D2*CMQC))
      ALPHAC=ALPHA*(ALP*57.3
      CLCC=CLC*COS(DALP)-CDC*SIN(DALP)
      CDCC=CLC*SIN(DALP)+CDC*COS(DALP)
      CMCC=CMC
C ---

C --- MINIMUM OUTPUT AND CP PLOT
      UMIN=RMIN(DATA1(1,3),NMST,IE)
      UMINA=RMIN(DATA1(1,6),NMST,IE)
      IF(UMINA.LT.UMIN) UMIN=UMINA
      IF(UMIN.GT.0.) UMIN=0.
      UMAX=RMAX(DATA1(1,3),NMST,IE)
      UMAXA=RMAX(DATA1(1,6),NMST,IE)
      IF(UMAXA.GT.UMAX) UMAX=UMAXA
      IF(UMAX.LT.0.) UMAX=0.
      ESCALE=UMAX-UMIN
      UMINP=-UMIN
      UA=DATA1(NMST,4)-UMIN
```

SUBROUTINE FOR TABULATING THE OUTPUT PARAMETERS AND GENERATING A LINE PRINTER PLOT OF THE SIGNATURE MATCHING.

APPLICATION OF THE BLOCKAGE PARAMETERS AND INCIDENCE CORRECTIONS TO THE SUPPLIED UNCORRECTED AERODYNAMIC COEFFICIENTS.

DETERMINATION OF THE PLOT LIMITS (UMIN AND UMAX) AND THE LOCATION OF THE ORIGIN (UMINP).
THE PLOT SCALE FACTOR (ESCALE) IS CALCULATED AND THE TITLE LINE DISPLAYED.

```
            CALL EPSPL(UMINP,FSCALE,NI,M3,JD3)
 55         CALL EPSPL(UMINP,FSCALE,NE,M4,JD4)
            CHK1=ABS(DATA2(11))
            CHK2=ABS(DATA2(2)-DATA2(10))
            IF(IRUN.NE.IRUNO) IS=0
            IRUNO=IRUN
 60         IS=1-IS
            IF(IS.EQ.0) WRITE(IPR,19)
            IF(IS.EQ.1) WRITE(IPR,20)
            WRITE(IPR,21) TIEST,IRUN,EPT,FSCALE
            ML=0
 65         M2=NWST+1
      C ---


      C --- MEASURED AND CALCULATED DATA
            DO 14 I=1,24
            LINE=MS(ML+1)
 70         IF(I.NE.LINE) GO TO 11
            ML=ML+1
            GO TO (1,2,3,4,5,6,7,8,9,10),ML
          1 WRITE(IPR,22) (TITLE(J),J=1,16),NI
            GO TO 12
 75       2 WRITE(IPR,23) NI
            GO TO 12
          3 WRITE(IPR,24) ALPHA,QO,PO,CLO,CDO,CMO,CPOO,NI
            GO TO 12
          4 WRITE(IPR,25) ALPHA,QO,PO,CLC,CDC,CMC,CPUC,NI
 80         GO TO 12
          5 WRITE(IPR,26) ALPHAC,QO,PO,CLCC,CDCC,CMCC,CMUC,NI
            GO TO 12
          6 WRITE(IPR,27) (DATA2(J),J=1,4),NI
            GO TO 12
 85       7 WRITE(IPR,28) (DATA2(J),J=5,8),NI
            GO TO 12
          8 WRITE(IPR,29) (DATA2(J),J=9,12),NI
            GO TO 12
          9 WRITE(IPR,30) (DATA2(J),J=13,16),NI
 90         GO TO 12
         10 WRITE(IPR,31) DATA2(17),NI
            GO TO 13
         11 WRITE(IPR,32) NI
         12 IF(I.GT.NWST) GO TO 13
 95         U1=DATA1(I,6)-UMIN
            U2=DATA1(I,3)-UMIN
            JD1=1
            JD2=1
            CALL EPSPL (U2,FSCALE,N,M2,JD2)
100         WRITE(IPR,33) N
            N(JD2)=KBL
            IF(CHK1.LE.C.C01) GO TO 14
            CALL EPSPL (U1,FSCALE,N,M1,JD1)
            WRITE(IPR,33) N
105         N(JD1)=KBL
            GO TO 14
      C ---
```

THE CORRECTED COEFFICIENTS AND THE BLOCK OF PARAMETERS ARE PRINTED OUT TOGETHER WITH THE LINE PRINT PLOT SHOWING THE CALCULATED HALL VELOCITY SIGNATURE (U1) AND THE MEASURED DATA (U2), DENOTED BY THE SYMBOLS O AND X RESPECTIVELY.

```
C --- ASYMPTOTE
   11 CONTINUE
      IF(I.EQ.NZ) CALL EPSPL(UA,FSCALE,N,ME,JDI)
      WRITE(IPR,33) N
   15 CONTINUE
      IF(CHK1.LT.C.CCI) GO TO 15
      IF(CHK2.LT.C.CCI) GO TO 16
      WRITE(IPR,34)
      GO TO 17
   15 WRITE(IPR,35)
      GO TO 17
   16 WRITE(IPR,36)
   17 WRITE(IPR,32) NE
      NE(JD1)=KBL
      NE(JD3)=KBL
      NE(JD4)=IBL
C ---


C --- ADDITIONAL OPTIONAL OUTPUT
      IF(ILEST.EQ.0) RETURN
      WRITE(IPR,37)
      DO 18 I=1,9
      IF(I.EC.3) WRITE(IPR,38)
      IF(I.EQ.7) WRITE(IPR,38)
   18 WRITE(IPR,39) TET(I),(DATA(J,I),J=1,NRSE)
      IS=0
      RETURN
C ---
   19 FORMAT(//)
   20 FORMAT(1HL/)
   21 FORMAT(5X,4HTEST,I4,3X,3HRUN,I4,3X,5HPOINT,I3,43X,12H(----------,
     *       22H C/C ---- FULL SCALE =,F6.4,12H ----------))
   22 FORMAT(5X,1CA4,8X,1H.,25A2,1H.)
   23 FORMAT(17X,5HALPHA,5X,2HQO,7X,2HPO,6X,2HCL,6X,2HCD,6X,2HCM,5X,
     *       3HCMC,7X,1H.,25A2,1H.)
   24 FORMAT(5X,9HMEASURED ,F8.2,F7.2,F9.2,4F8.4,7X,1H.,25A2,1H.)
   25 FORMAT(5X,9HBLOCKAGE ,F8.2,F7.2,F9.2,4F8.4,7X,1H.,25A2,1H.)
   26 FORMAT(5X,9HINCIDENCE,F8.2,F7.2,F9.2,4F8.4,7X,1H.,25A2,1H.)
   27 FORMAT(5X,1CHEPS(MOD) =,F7.4,12H  X(MCD)/B =,F6.3,8H  BS/B =,
     *       F6.3,1CH  OS/UBH =,F8.5,5X,1H.,25A2,1H.)
   28 FORMAT(5X,1CHEPS(MAX) =,F7.4,12H  X(MAX)/B =,F6.3,8H  DX/B =,
     *       F6.3,1CH  DW/UBH =,F8.5,5X,1H.,25A2,1H.)
   29 FORMAT(5X,1CHF FACTOR =,F7.4,12H  XV/B     =,F6.3,8H  CS/B =,
     *       F6.3,1CH  A5     =,F8.5,5X,1H.,25A2,1H.)
   30 FORMAT(5X,1CHCCORR    =,F7.4,12H  US(MAX)/U=,F6.3,8H  UFH  =,
     *       F6.3,1CH  A6     =,F8.5,5X,1H.,25A2,1H.)
   31 FORMAT(56X,6HA7     =,F8.5,5X,1H.,25A2,1H.)
   32 FORMAT(77X,1H.,25A2,1H.)
   33 FORMAT(1H+,77X,25A2)
   34 FORMAT(23H+    NORMAL COMPUTATION)
   35 FORMAT(23H+    HENSEL COMPUTATION)
   36 FORMAT(23H+    DIVERGENCE LIMIT  )
   37 FORMAT(//45H     WALL/CEILING PRESSURE BLOCKAGE COMPUTION//)
   38 FORMAT()
   39 FORMAT(/5X,A4,15F8.4/9X,6F8.4)
      END
```

THE PLOT IS CONCLUDED WITH AN ASYMPTOTIC LINE WHICH VARIES IN LENGTH TO ACCOMODATE THE NUMBER OF WALL PRESSURES THAT ARE USED.
THIS RESULTS IN ONE-HALF PAGE OF OUTPUT.

AN ADDITIONAL HALF-PAGE OF OUTPUT IS AVAILABLE (ILEST=1) TABULATING ALL THE WALL AND CENTER TUNNEL COMPONENTS OF THE BLOCKAGE SIGNATURE.

```
      SUBROUTINE EPSPLT(LU)                                              DUMMY ROUTINE FOR CUSTOMER INSERTION OF PLOTTER/
C ---  PLOTTING CONTROL                                                  GRAPHICS ROUTINES.
C ---
      COMMON ITEST,IRUN,IPT,NWST,DATA2(17),B(61,DATA1(21,9)
C ---
      RETURN
      END
```

APPENDIX III

PROGRAM LISTING: LIBRARY ROUTINES

```
      SUBROUTINE LSC(FX,A,N,NP,C)
      DIMENSION A(11,12),C(1),X(11),FX(1)
      N1=N+1
      N2=N+2
    5 DO 10 I=1,N1
      DO 10 J=1,N2
   10 A(I,J)=0.
      DO 30 K=1,NP
      T1=1.
   10 DO 30 J=1,N1
      T2=T1
      DO 20 I=1,N1
      A(J,I)=A(J,I)+T2
   20 T2=T2*X(K)
   15 A(J,N2)=A(J,N2)-FX(K)*T1
   30 T1=T1*X(K)
      DO 40 K=1,N
      DO 40 J=K,N
      T1=A(J+1,K)/A(K,K)
   20 DO 40 I=K,N2
   40 A(J+1,I)=A(J+1,I)-A(K,I)*T1
      C(N1)=-A(N1,N2)/A(N1,N1)
      DO 50 I=2,N1
      K=N2-I
   25 C(K)=-A(K,N2)/A(K,K)
      L=K+1
      DO 50 J=L,N1
   50 C(K)=C(K)-C(J)*A(K,J)/A(K,K)
      RETURN
   30 END
```

SUBROUTINE FOR DETERMINING THE COEFFICIENTS OF A POLYNOMIAL USING A LEAST SQUARES FITTING ROUTINE.

```
      SUBROUTINE PEAK (ARRAY,XARRAY,N,PK,X)
      DIMENSION ARRAY(20),XARRAY(20)
      ARRYPK=RMAX(ARRAY,N,J)
      IF(J.EQ.1) GO TO 3
    5 U1= ARRAY(J-1)
      U2= ARRAY(J)
      U3= ARRAY(J+1)
      X1=XARRAY(J-1)
      X2=XARRAY(J)
   10 X3=XARRAY(J+1)
      X= (U1*(X2*X2-X3*X3)+U2*(X3*X3-X1*X1)+U3*(X1*X1-X2*X2))/
     1   (2.*(U1*(X2-X3)+U2*(X3-X1)+U3*(X1-X2)))
      PK=U1*(X -X2)*(X -X3)/((X1-X2)*(X1-X3))+
     1   U2*(X -X3)*(X -X1)/((X2-X1)*(X2-X3))+
   15 2   U3*(X -X1)*(X -X2)/((X3-X1)*(X3-X2))
      GO TO 4
    3 PK=ARRAY(J)
      X=XARRAY(J)
    4 RETURN
   20 END
```

SUBROUTINE FOR INTERPOLATING AN ARRAY OF DATA POINTS FOR THE MAXIMUM VALUE AND ITS POSITION.

```
      FUNCTION CTABI(ARG,X,Y,NX,IC)
C     AITKIN INTERPOLATION
C     ARG=INDEPENDENT ARGUMENT
C     X=INDEPENDENT TABLE
C     Y=DEPENDENT TABLE
C     NX=NUMBER VALUES X TABLE
C     IC=1 FIRST ORDER INTERPOLATION
C     IC=2 SECOND ORDER INTERPOLATION
      DIMENSION X(1),Y(1),XX(4),YY(4),EE(3),FF(2)
      IEND=NX-IC+1
      IF(X(1)-X(2))10,20,20
C     ASCENDING ORDER
   10 DO 15 I=1,IEND
      IF(X(I)-ARG)15,30,30
   15 CONTINUE
   16 IB=NX-IC
      IEX=0
      GO TO 45
   20 DO 25 I=1,IEND
      IF(X(I)-ARG)25,30,30
   25 CONTINUE
      GO TO 16
   30 IF(IC-1)35,35,40
   35 IF(I-1)36,36,37
   36 IB=1
      GO TO 45
   37 IB=I-IC
      GO TO 45
   40 IF(I-2)41,41,42
   41 IEX=0
      GO TO 36
   42 IEX=1
      GO TO 37
   45 DO 50 I=1,4
      XX(I)=X(IB)-ARG
      YY(I)=Y(IB)
   50 IB=IB+1
      DO 60 I=1,3
   60 EE(I)=XX(I+1)-XX(I)
      DO 70 I=1,2
   70 FF(I)=EE(I)+EE(I+1)
      DO 80 I=1,3
      EE(I)=(YY(I)*XX(I+1)-YY(I+1)*XX(I))/EE(I)
      IF(IC-1)100,100,80
   80 CONTINUE
      DO 90 I=1,2
   90 EE(I)=(XX(I+2)*EE(I)-XX(I)*EE(I+1))/FF(I)
      IF(IEX)100,100,95
   95 EE(1)=(EE(1)+EE(2))/2.
  100 CTA=EE(1)
      RET N
      EN
```

INTERPOLATION ROUTINE FOR A SINGLE ARRAY.
INTERPOLATION MAY BE FIRST OR SECOND ORDER.

```
      FUNCTION DTAB2(XX,ZI,X,Z,NX,NZ,KX,KZ,Y,M,IERR)
C     DTAB   DOUBLE INTERPOLATION
C  XX=VALUE TO BE INTERPOLATED X DIRECTION
C  ZI=VALUE TO BE INTERPOLATED Z DIRECTION
C  X= X TABLE
C  Z= Z TABLE
C  NX=NUMBER X VALUES IN TABLE
C  NZ=NUMBER Z VALUES IN TABLE
C  KX=1 IF LINEAR INTERPOLATION X DIRECTION
C    =2 IF CURVILINEAR
C  KZ=1 IF LINEAR INTERPOLATION Z DIRECTION
C    =2 IF CURVILINEAR
C  Y =Y ARRAY
C  M =ROW DIMENSION
C  IERR=1 SUCCESSFUL RETURN
C      =2 UNSUCCESSFUL RETURN
      DIMENSION X(1),Z(1),Y(1),X2(4),Z2(4),Y2(16),INX(2),IKX(2),
     1ISV(2),IXINT(2)
      ZZ=ZI
      INX(1)=NX
      INX(2)=NZ
      IKX(1)=KX
      IKX(2)=KZ
      DO 200 I=1,2
      IF(INX(I)-2)100,140,10
   10 IF(I-1)11,11,12
   11 IF(X(1)-X(2))20,1000,30
C     ASCENDING ORDER
   20 DO 21 J=1,NX
      IF(X(J)-XX)21,40,50
   21 CONTINUE
C  VALUE BEYOND END OF TABLE
   22 ISV(I)=INX(I)-IKX(I)
   23 IXINT(I)=IKX(I)
      GO TO 150
   12 IF(Z(1)-Z(2))25,1000,35
   25 DO 26 J=1,NZ
      IF(Z(J)-ZZ)26,40,50
   26 CONTINUE
      GO TO 22
C     DESCENDING ORDER
   30 DO 31 J=1,NX
      IF(X(J)-XX)50,40,31
   31 CONTINUE
      GO TO 22
   35 DO 36 J=1,NZ
      IF(Z(J)-ZZ) 50,40,36
   36 CONTINUE
      GO TO 22
C     VALUE EQUAL VALUE IN TABLE
   40 IXINT(I)=0
      ISV(I)=J
      GO TO 150
   50 IF(J-1)60,60,70
   60 ISV(I)=1
      GO TO 23
   70 IF(J-2)60,80,80
   80 ISV(I)=J-IKX(I)
      IF(IKX(I)-2)23,90,90
   90 IF(ISV(I)+2+IKX(I)-INX(I))100,100,23
```

INTERPOLATION ROUTINE FOR A DOUBLE ARRAY.
INTERPOLATION IN EITHER DIRECTION MAY BE FIRST OR
SECOND ORDER.

```
      100  IXINT(1)=1
           GO TO 150
      140  IXINT(1)=1
           ISV(1)=1
   65 150  JI=ISV(1)
           IF(I-1)155,155,160
      155  DO 156 J=1,4
           X2(J)=X(JI)
      156  JI=JI+1
   70      GO TO 200
      160  DO 165 J=1,4
           Z2(J)=Z(JI)
      165  JI=JI+1
      200  CONTINUE
   75      IC=1
           K=(ISV(1)-1)*F+ISV(2)-M
           DO 220 I=1,4
           K=K+M
           DO 210 J=1,4
   80      KI=K+J-1
           Y2(IC)=Y(KI)
      210  IC=IC+1
      220  CONTINUE
      225  IF(IXINT(2))301,301,230
   85 230  IZO=IXINT(2)
           IZO2=IZO
           DO 280 K=1,IZO
           DO 270 I=1,IZO2
           DZ1=Z2(I)-ZZ
   90      KI=K+I
           DZ2=Z2(KI)-ZZ
           DZ=DZ2-DZ1
           IXC=IXINT(I)*4+1
           DO 260 J=1,IXC,4
   95 260  Y2(J)=(Y2(J)*DZ2-Y2(J+1)*DZ1)/DZ
      270  CONTINUE
           IZO2=IZO2-1
      280  CONTINUE
      301  IF(IXINT(1))400,400,300
  100 300  IXINT(2)=IXINT(1)
           IXINT(1)=0
      302  IC=1
           DO 310 I=1,4
           Z2(I)=X2(I)
  105      Y2(I)=Y2(IC)
      310  IC=IC+4
           ZZ=XX
           GO TO 225
      400  DIAB2=Y2(1)
  110      IERR=1
           RETURN
     1000  IERR=2
           DIAB2=0.
           RETURN
```

```
      REAL FUNCTION RMIN (X,J,II)
      DIMENSION X(99)
      I=1
      II=1
      RMIN=X(1)
    1 IF(I.EQ.J) GO TO 4
      I=I+1
      IF(X(I).LT.RMIN) GO TO 2
      GO TO 1
    2 RMIN=X(I)
      II=I
      GO TO 1
    4 CONTINUE
      RETURN
      END
```

FUNCTION FOR DETERMINING THE MINIMUM VALUE IN AN ARRAY OF NUMBERS AND ITS SUBSCRIPT.

```
      REAL FUNCTION RMAX (X,J,II)
      DIMENSION X(99)
      I=1
      II=1
      RMAX=X(1)
    1 IF(I.EQ.J) GO TO 4
      I=I+1
      IF(X(I).GT.RMAX) GO TO 2
      GO TO 1
    2 RMAX=X(I)
      II=I
      GO TO 1
    4 CONTINUE
      RETURN
      END
```

FUNCTION FOR DETERMINING THE MAXIMUM VALUE IN AN ARRAY OF NUMBERS AND ITS SUBSCRIPT.

```
      SUBROUTINE EPSPL (U,FSCALE,N,P,JD)
      DIMENSION N(25),M(2)
      ID=(U/FSCALE)+49.5
      LL=107+1
      KD=ID-20*JD+3
      N(JD)=M(KE)
      JD=JD
      RETURN
      END
```

SUBROUTINE FOR CALCULATING THE LINE OUTPUT OF THE LINE PRINTER PLOT.

APPENDIX IV

WORKING CHARTS FOR RECTANGULAR WIND TUNNELS

APPENDIX IV

WORKING CHARTS FOR RECTANGULAR WIND TUNNELS

The later stages of wall pressure signature analysis require references to data charts or carpets which are used to determine blockage line source and line sink details from measured signature characteristics (see Figure 2.3). For rectangular tunnels, the influence coefficients needed to define these carpets can be written in closed form as given below. Less regularly shaped tunnels, such as the 40' x 80', may require a numerical approach (see Appendix V).

Equations for a Source-Sink Flow Model (Rectangular Tunnel)

For a flow model involving three horizontal line sources on the center plane of a rectangular tunnel, the axial velocity increment induced at a point x, y, z is given by

$$\Delta u = \sum_{L=2}^{4} \frac{Q_L}{8\pi s_L} \sum_{m=-M}^{M} \sum_{n=-N}^{N} R + \sum_{L=2}^{4} \frac{Q_L}{2BH} \frac{(x - x_L)}{ABS(x - x_L)} - \sum_{L=2}^{4} \frac{Q_L}{4\pi BH} T$$

$$+ \sum_{L=2}^{4} \frac{Q_L}{2\,BH} . \qquad (A1)$$

In equation (A1), R is an axial velocity function, for axial velocity at a receiving point x, y, z, given by

$$R = \frac{X}{\{X^2 + Z^2\}} \left[\frac{(Y + s_L)}{\{X^2 + (Y-s_L)^2 + Z^2\}^{\frac{1}{2}}} - \frac{(Y - s_L)}{\{X^2 + (Y-s_L)^2 + Z^2\}^{\frac{1}{2}}} \right]$$

where $X \equiv x - x_L$

$Y \equiv mB - y$

$Z \equiv nH - z.$

L is the index for the source system and m, n represent the image cell location in the cross flow plane (m = n = 0, representing the central source, is included in the summations when wall velocities are calculated but excluded when interference velocities are required.) L = 1 is reserved for the model location.

Γ, in equation (A1) is obtained from

$$\Gamma = \tan^{-1} \frac{Y_1 Z_1}{X\{X^2 + Y_1^2 + Z_1^2\}^{\frac{1}{2}}} - \tan^{-1} \frac{Y_1 Z_2}{X\{X^2 + Y_1^2 + Z_2^2\}^{\frac{1}{2}}}$$

$$- \tan^{-1} \frac{Y_2 Z_1}{X\{X^2 + Y_2^2 + Z_1^2\}^{\frac{1}{2}}} + \tan^{-1} \frac{Y_2 Z_2}{X\{X^2 + Y_2^2 + Z_2^2\}^{\frac{1}{2}}}$$

where

$$X \equiv (x - x_L)$$

$$Y_1 \equiv \left(y + (2M+1)\frac{B}{2}\right) \qquad Y_2 \equiv \left(y - (2M+1)\frac{B}{2}\right)$$

$$Z_1 \equiv \left(z + (2N+1)\frac{H}{2}\right) \qquad Z_2 \equiv \left(z - (2N+1)\frac{H}{2}\right) .$$

The tangent function, Γ, concerns the velocity induced at the "receiving" point x, y, z by a transverse rectangular source plate situated at $x = x_L$ and covering an area (2M+1)B by (2N+1)H.

For each source system, L in equation (A1), the line source function R, is summed over a finite number of tunnel images in the first term. The middle two terms approximate the region outside of this by considering it as a doubly-infinite source sheet (second term) minus the "hole" (third term) which is already represented. The final term represents downstream sink sheets needed for continuity and ensures zero disturbance far upstream of the model.

As written, there are nine unknowns in equation (A1); three source strengths, Q_L, three line source positions, x_L, and three source semi-spans, s_L. The problem is converted to more convenient notation and reduced to seven unknowns by putting

$$Q_3 = +Q_s \qquad s_3 = \frac{1}{2} b_s$$

$$Q_4 = -Q_s \qquad s_4 = \frac{1}{2} b_s \qquad \text{(A2)}$$

and

$$Q_2 = Q_w \qquad s_2 = \frac{1}{2} b_w \qquad \text{(A3)}$$

The subscript s refers to solid or separation-bubble blockage and w refers to wake blockage.

Preparation of Working Charts (a) Signature Analysis (Charts I and II)

Charts I and II are used when matching the measured signature to the idealized mathematical model of the flow. Prior to using these charts, the measured signature is resolved into symmetric and antisymmetric parts. Charts I and II are then used to analyze the symmetric, bell-shaped part. Preparation of these charts is described briefly below: a more detailed description is given in Reference 1.

Chart I (Figure A3) determines source-sink spacing, c_s/B, from the assumed source and sink spans b_s/B and the width of the symmetric part of the signature at half-height, $\Delta x/B$. To prepare the chart the symmetric terms, L = 3, 4 in Equation (A1) are evaluated at the wall location over a range in x/B between ±1.0 for the c_s/B, b_s/B combinations of interest. The central source and sink, for which m = n = 0, are included in the summations. For each c_s/B, b_s/B combination, the peak width at half-height, $\Delta x/B$, is determined. The results are then assembled suitably for chart or table look-up with $\Delta x/B$ and b_s/B as independent variables and c_s/B as the dependent variable. Cross-plotting is used to obtain "whole" values of $\Delta x/B$ for this purpose.

Chart II (Figure A4) is used in the determination of source and sink strengths $\pm Q_S/B^2$ from the same combinations of input variables, b_S/B and $\Delta x/B$. This is a departure from the Reference 1 procedure which employed c_S/B and $\Delta x/B$. To prepare Chart II, the symmetric terms in Equation (A1) are evaluated midway between the source and sink, i.e. at the velocity maximum. The quantity $(u_{max}B/Q_S)$ is determined for each c_S/B, b_S/B combination. For convenience and accuracy, c_S/B is replaced by $\Delta x/B$ for chart or table look-up purposes.

Preparation of Working Charts (b) Tunnel Centerline Interference (Chart III)

"Chart III" (Figure A5) gives the normalized tunnel centerline interference velocity, due to a single line source, as a function of x/B. Interference velocity is calculated using L = 1 and omitting m = n = 0 from the summation in Equation (A1). Figure A3 is drawn for a b_S/B value of 0.30. Strictly, a carpet should be drawn to include other b_S/B values. However, it is found in practice that dependence on b_S/B is very weak and the curve shown is adequate throughout the b_S/B range of interest.

The total source-source-sink interference signature is built up from Figure A5 using suitable scaling and superposition procedures.

Floor-Mounted Half-Models

For a rectangular tunnel of approximately $\sqrt{2}$ aspect ratio, the geometry is the same for a floor-mounted half model as it is for a centrally-mounted model. The same charts and procedures may therefore be used provided that tunnel height and width are increased so as to represent the "double tunnel" properly.

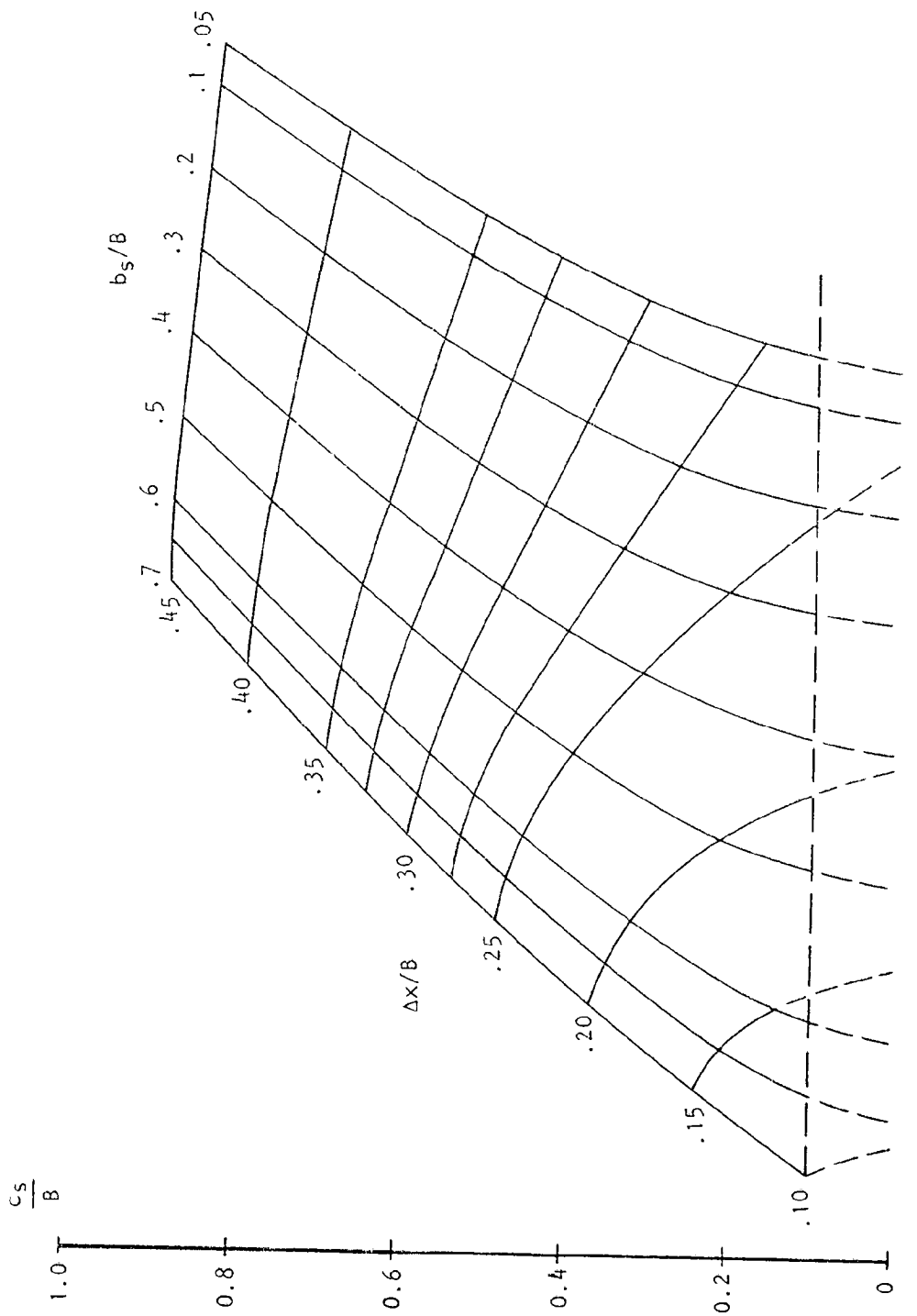

Figure A3 "Chart I": Determination of source-sink spacing (Rectangular tunnel, H/B = 0.699).

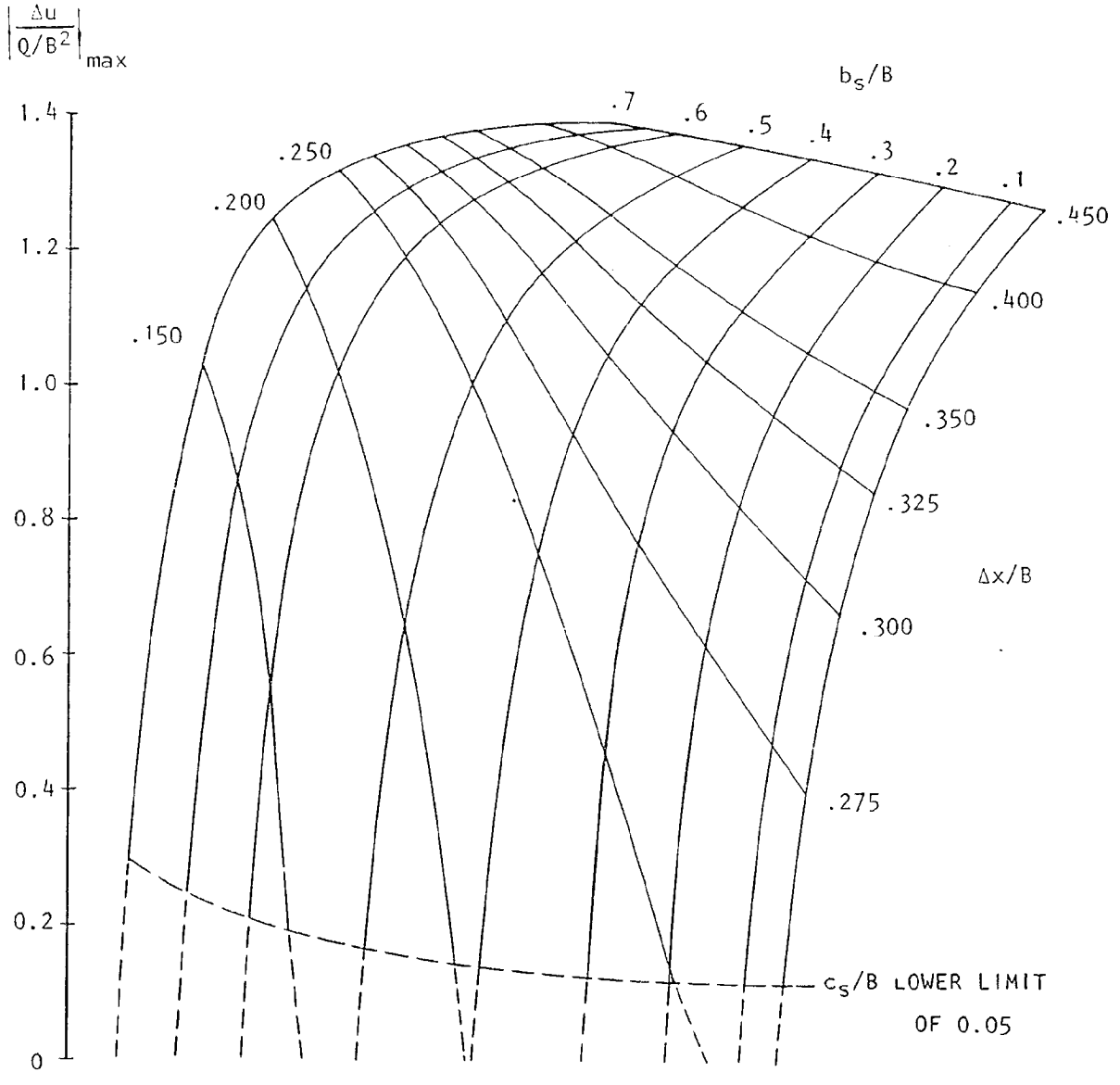

Figure A4 "Chart II": Determination of source-sink strengths (Rectangular tunnel, H/B = 0.699).

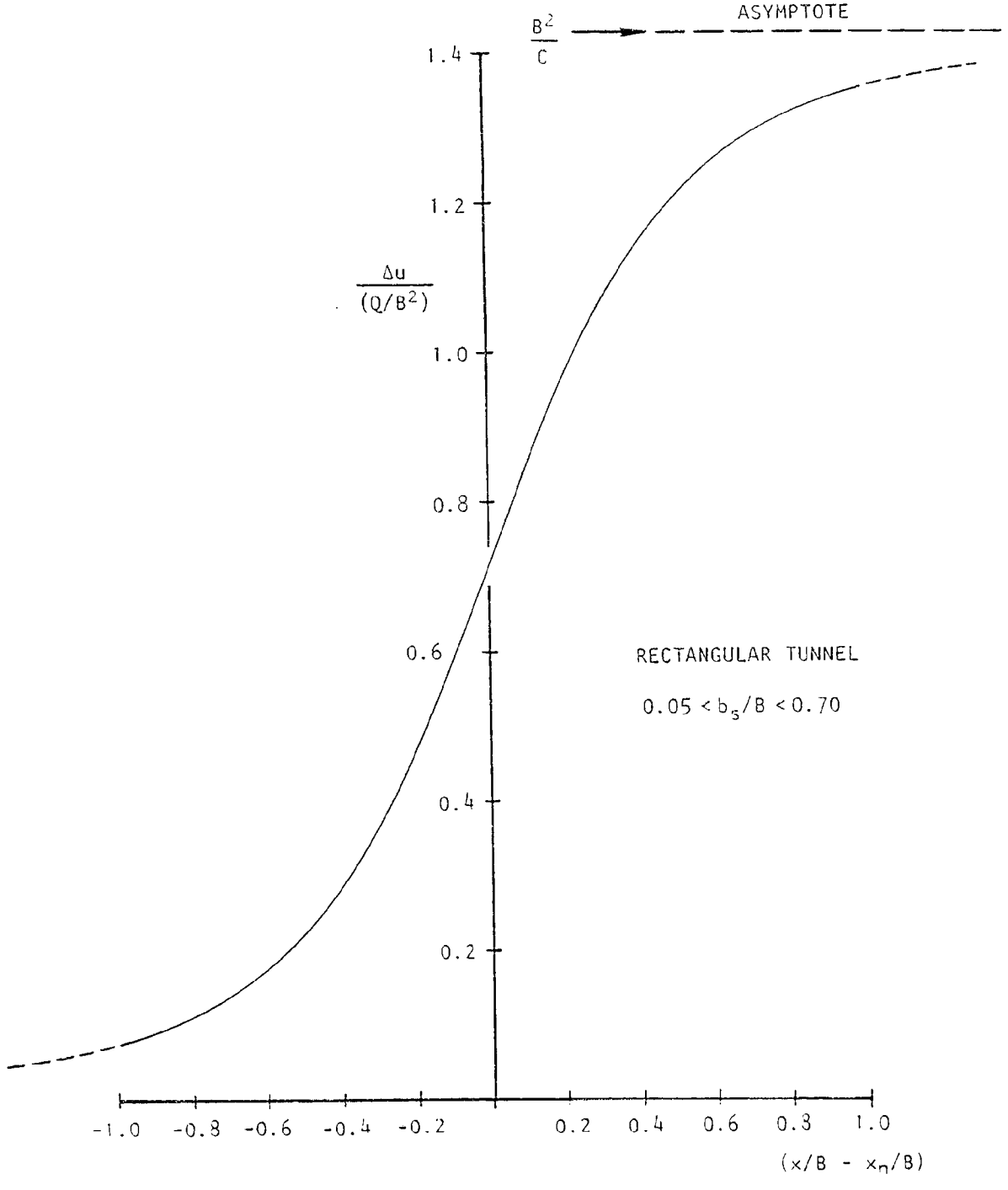

Figure A5 (Chart III) Interference velocities at tunnel centerline for a single line source (rectangular tunnel, H/B = 0.699)

APPENDIX V

WORKING CHARTS FOR THE 40' x 80' WIND TUNNEL

APPENDIX V

WORKING CHARTS FOR THE 40' x 80' WIND TUNNEL

The image methods described in Appendix IV cannot be applied to the 40' x 80' tunnel cross section because of its unusual shape. Errors for approximations to the shape (e.g. ellipses) were difficult to quantify and a detailed, surface panel technique was therefore employed.

Preparation of Charts I and II

Figure A6 shows the theoretical flow model used to generate data charts for the 40' x 80' tunnel. A section of tunnel about 3.5 diameters long is panelled with doublet sheets. Velocities due to a centrally located line source [Figure A7(a)] are calculated at each panel center. Various line source spans are used in successive calculations. In order to assure correct asymptotic behavior far upstream and far downstream, velocities due to ring vortex tube extensions are also calculated and added to the source-induced velocities. The test section boundary conditions are now defined completely. In the next stage of the calculation, an influence matrix is computed for the doublet panels and doublet strengths are found by inverting this matrix and applying the boundary conditions. Tunnel wall supervelocities are then computed and the resulting curves are developed to give "Chart I" (Figure A8) and "Chart II" (Figure A9) in the manner described in Appendix IV.

Preparation of "Chart III"

"Chart III" (Figure A10) gives the axial velocity along the model centerline with the central source removed. For this, velocities due to the ring vortex tubes are added to velocities induced by the doublet panels representing the test section.

In all of the above calculations the bilateral symmetry of the test section is exploited in order to reduce matrix size. Although there are 504 panels on the test section, only a 126 x 126 matrix is inverted.

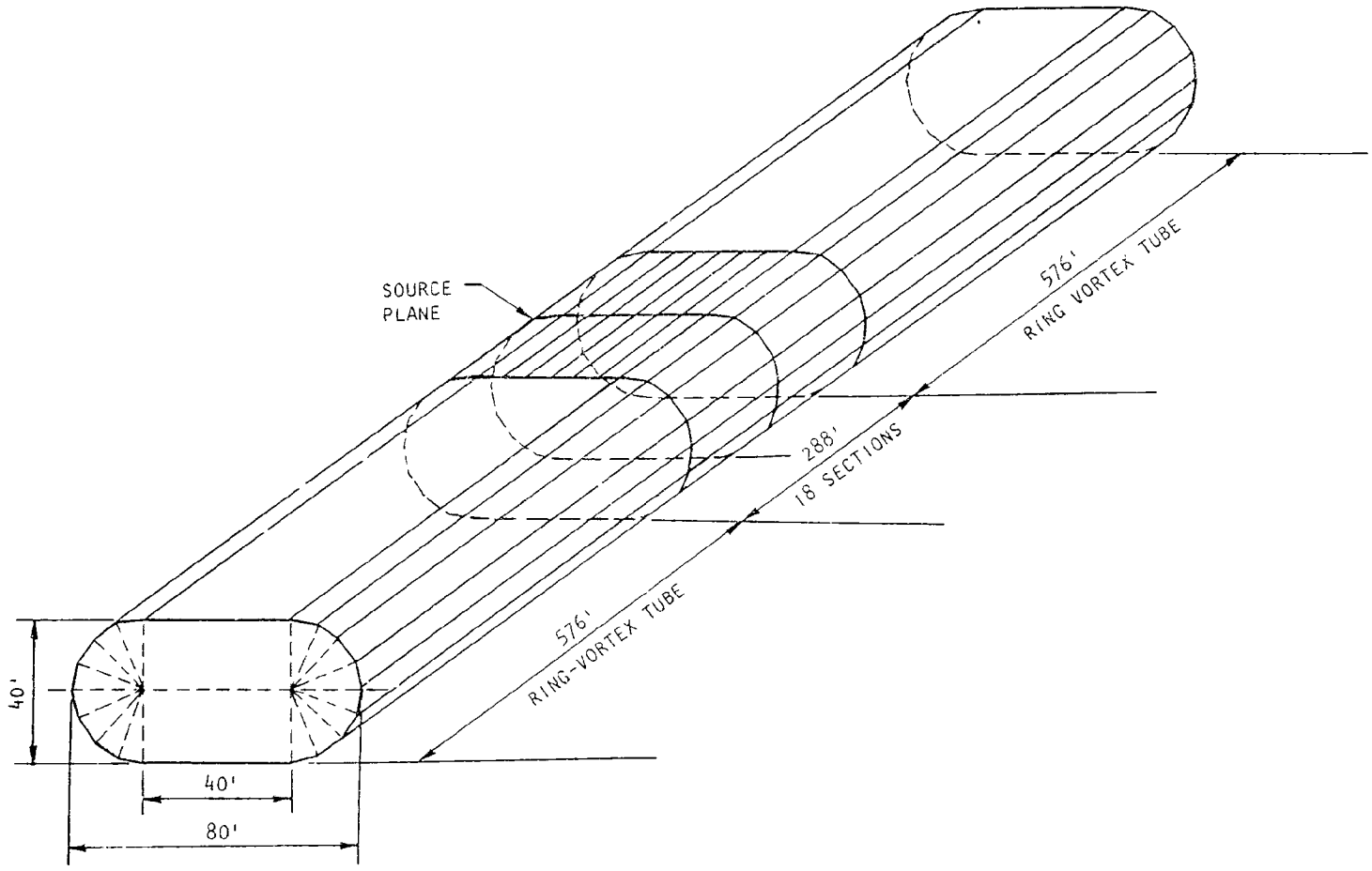

Figure A6 Flow model for representing the 40 × 80-foot wind tunnel.

Floor-Mounted Half Models

Because of the irregular cross-sectional shape, special calculations are needed for floor-mounted half models in the 40' x 80' wind tunnel. A complete image of the Figure A6 flow model, in the floor plane, must be created. The only exception is on the flat part of the floor, when imaging assures tangency [see Figure A7(b)]. The remaining calculation details were the same as for the center-tunnel case, except that a fore-aft imaging system was added, employing reflections in the source plane. This reduced the influence matrix from 198 x 198 to 99 x 99. The total system, including all the images, involves 792 panels.

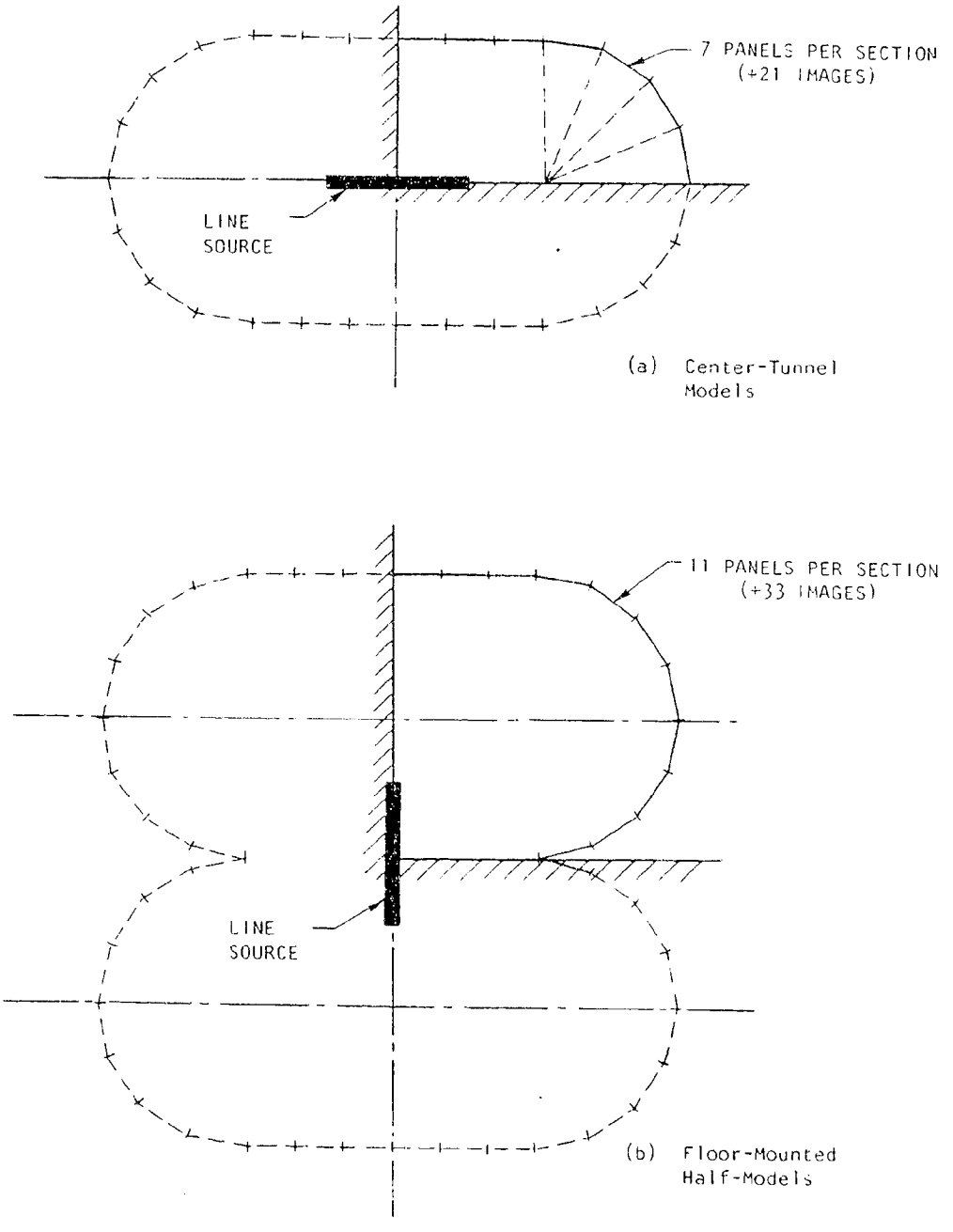

Figure A7 Cross-sectional detail of the flow model at the source plane.

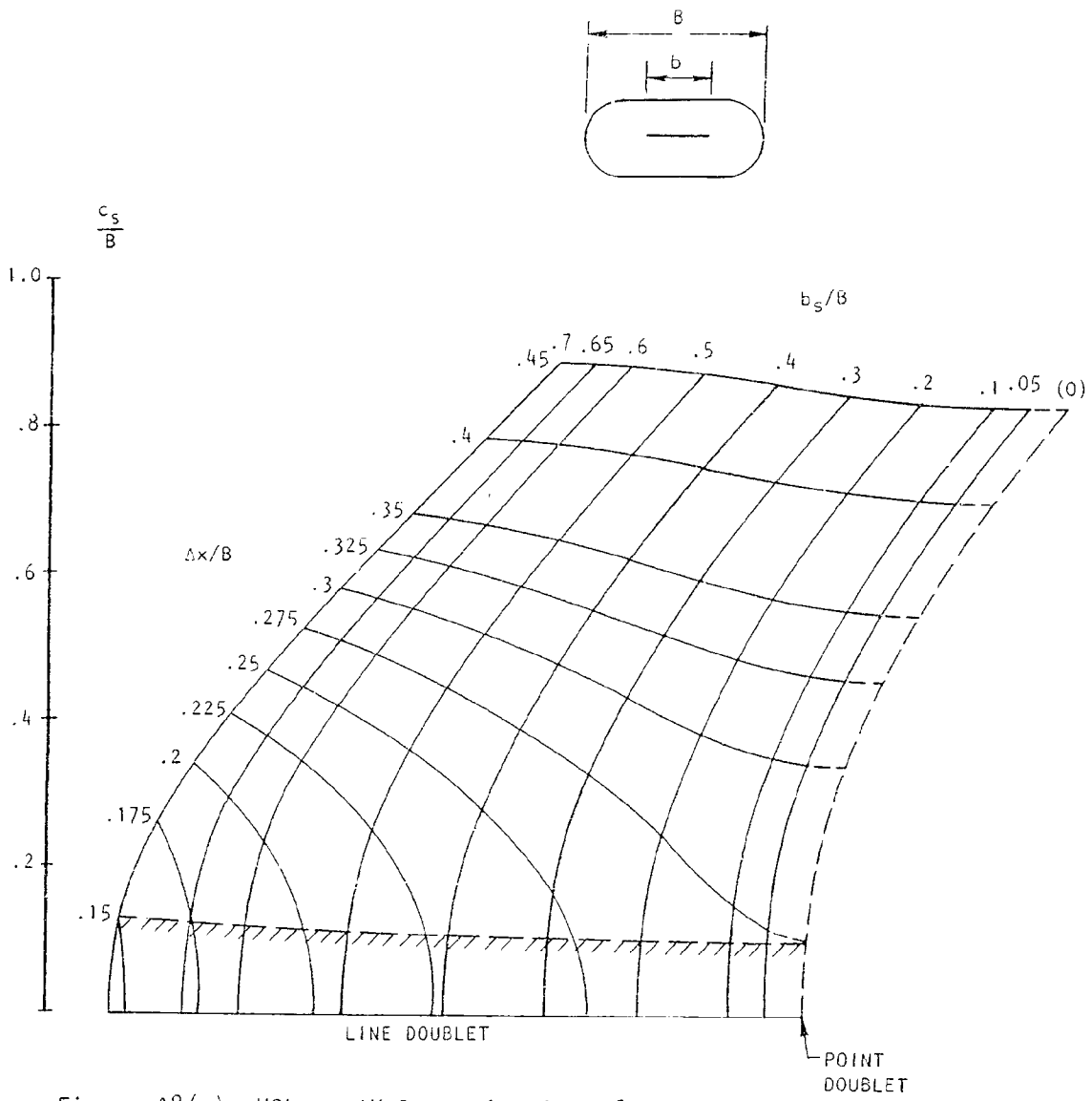

Figure A8(a) "Chart I" Determination of source-sink spacing for center-tunnel models (40' × 80' wind tunnel)

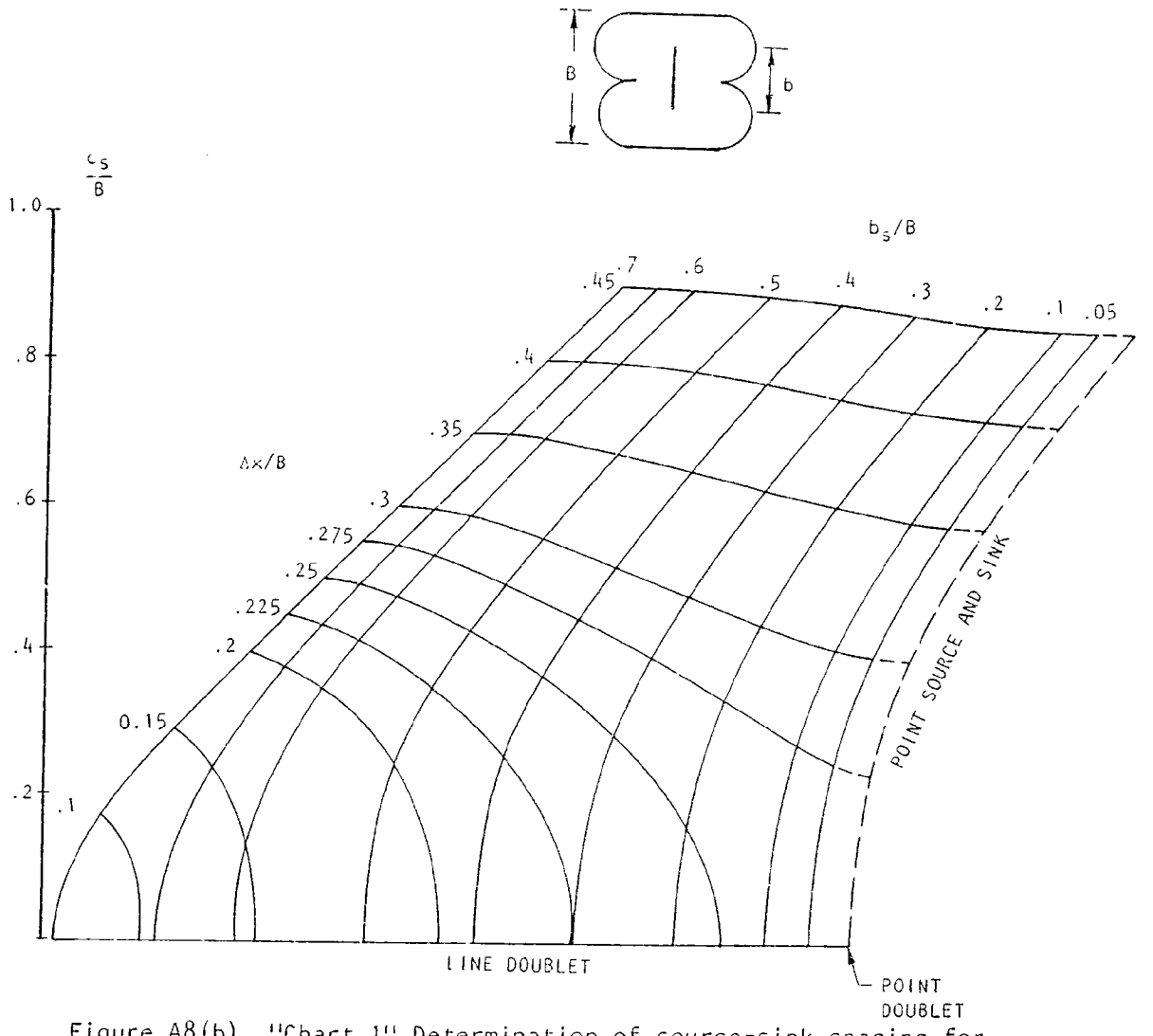

Figure A8(b) "Chart 1" Determination of source-sink spacing for floor-mounted half-models (40' × 80' wind tunnel)

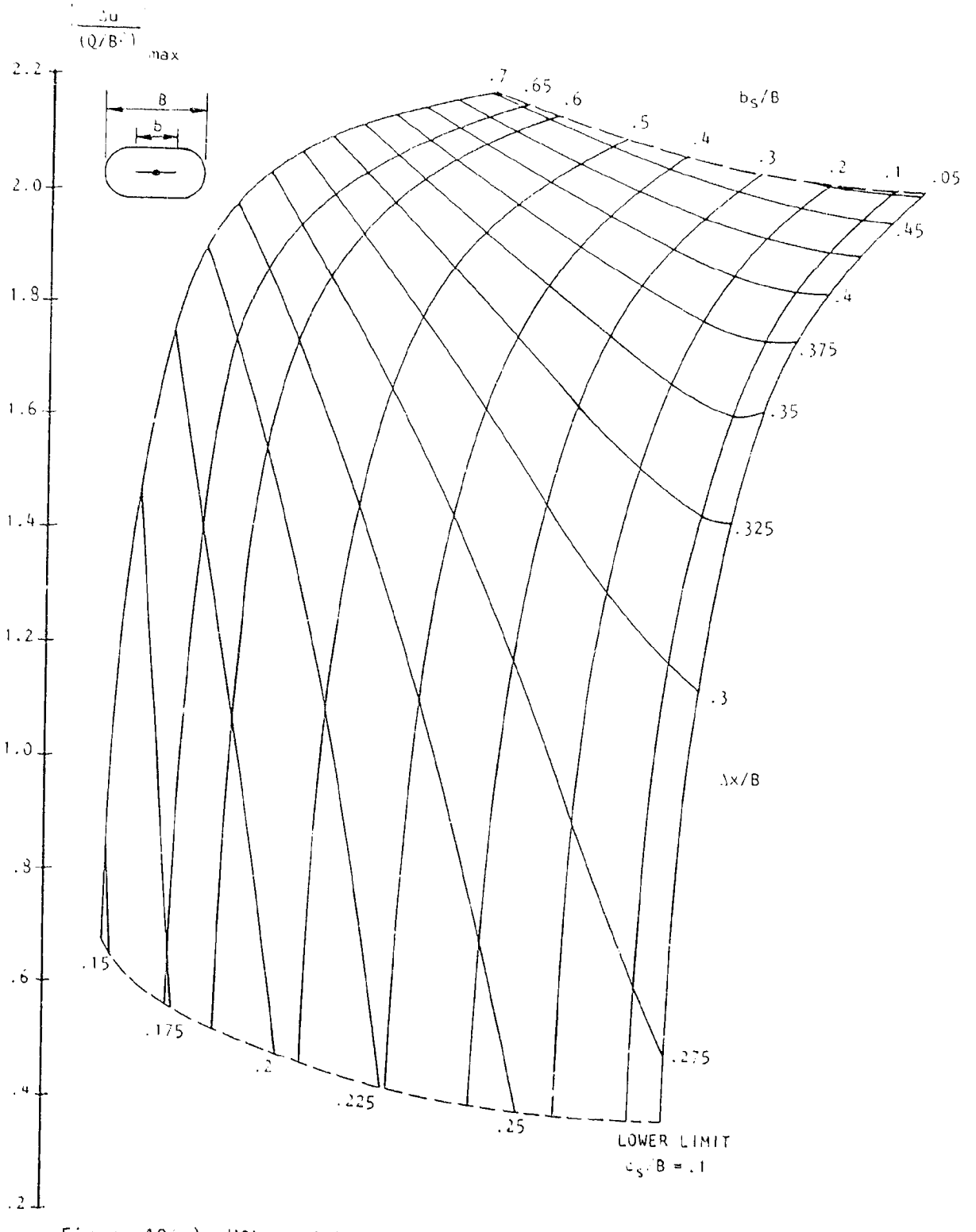

Figure A9(a) "Chart II" Determination of source-sink strength for center-tunnel models (40' × 80' wind tunnel)

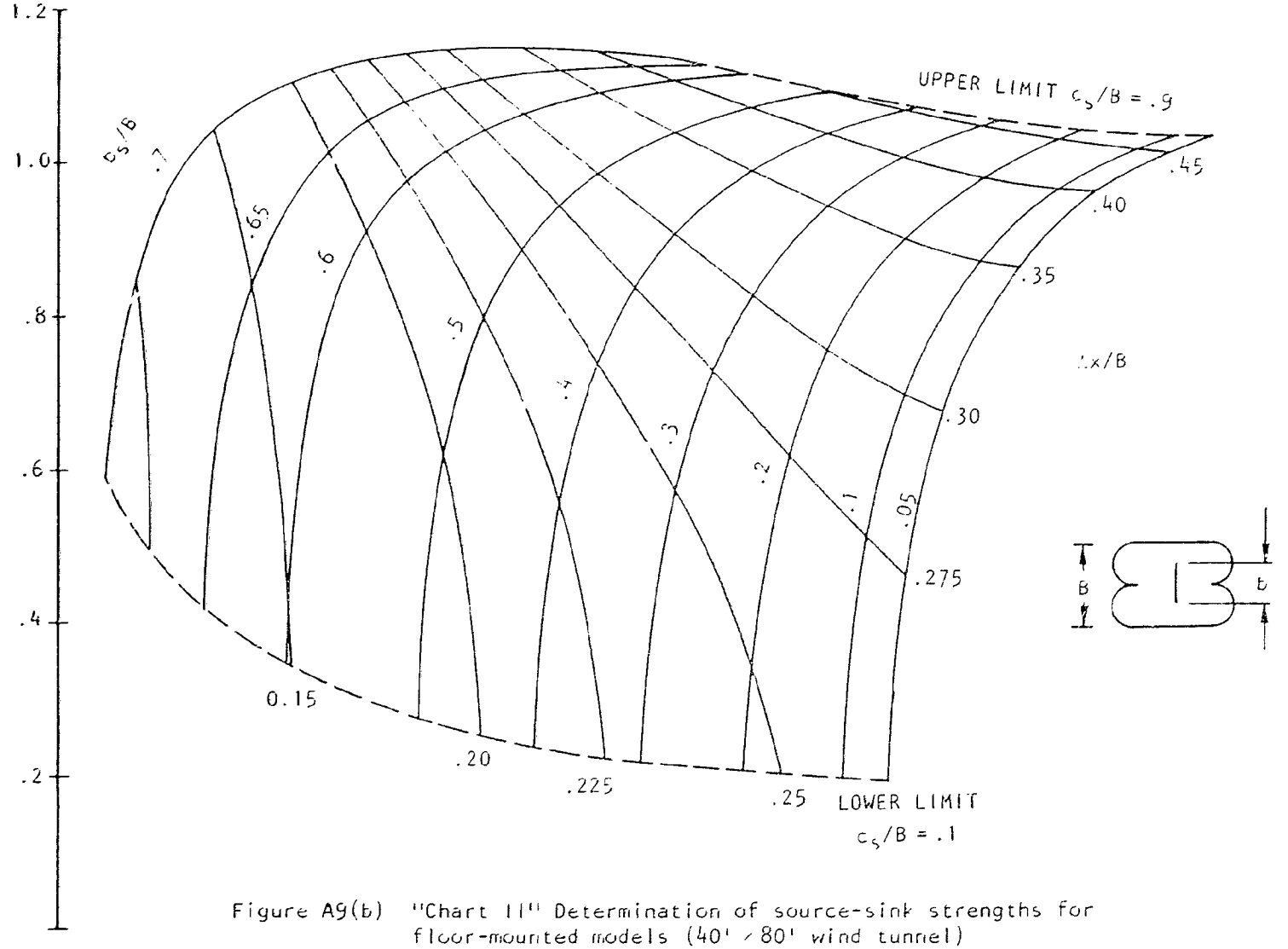

Figure A9(b) "Chart II" Determination of source-sink strengths for floor-mounted models (40' × 80' wind tunnel)

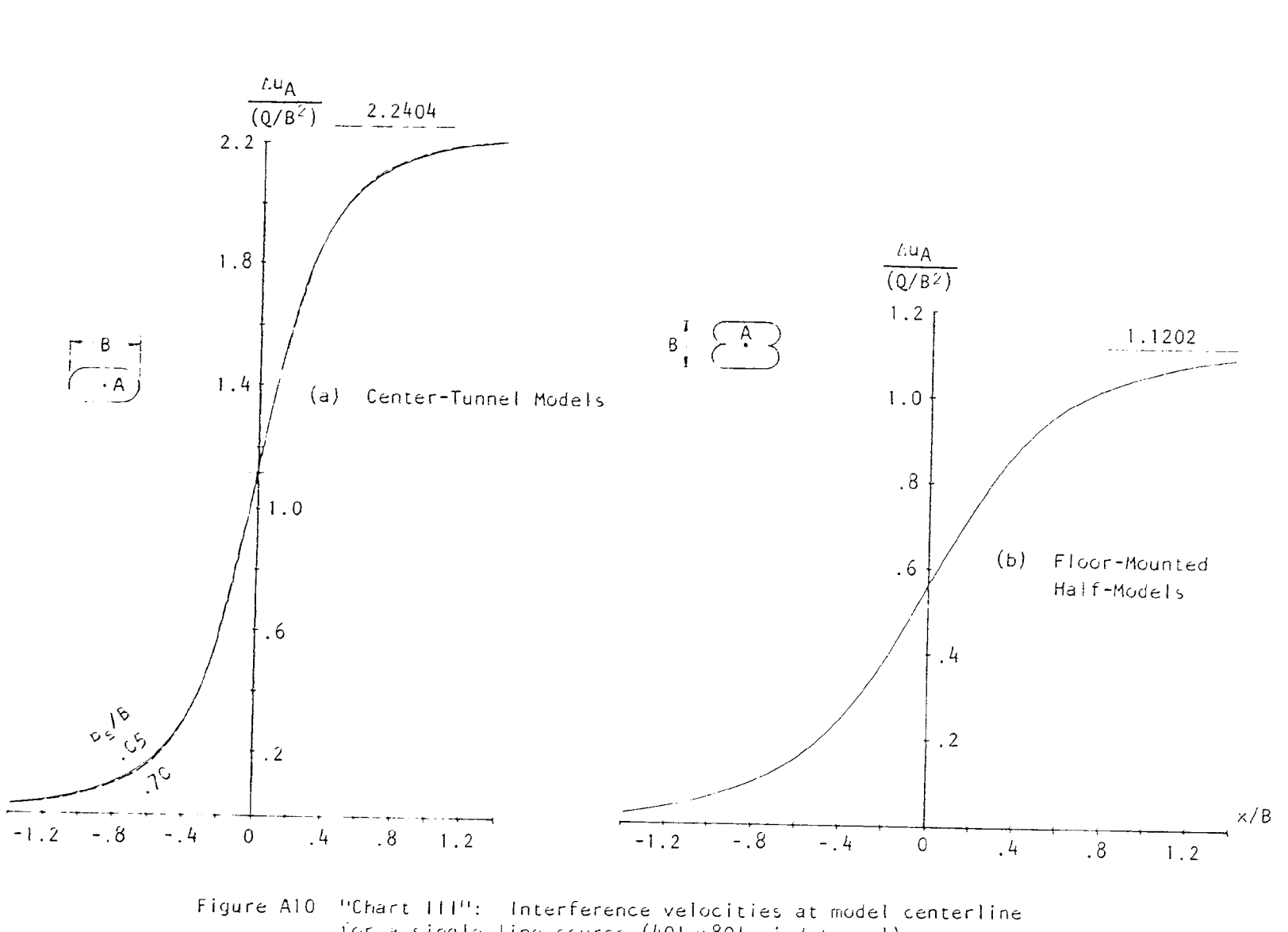

Figure A10 "Chart III": Interference velocities at model centerline for a single line source (40' x 80' wind tunnel).